TARGET DETECTION IN BUBBLE-POPULATED WATER USING BIO-MIMETIC SONAR

Yeo Kian Peen

BEng(Hons), NUS

A THESIS SUBMITTED
FOR THE DEGREE OF MASTER OF ENGINEERING
DEPARTMENT OF ELECTRICAL AND COMPUTER ENGINEERING
NATIONAL UNIVERSITY OF SINGAPORE
2010

Acknowledgements

I would like to thank Associate Prof. S.H. Ong, for his supervision and support during this research. I am also grateful to Dr. Elizabeth Taylor for having been constantly supportive and encouraging, and for her helpful suggestions and critical comments.

I would to express my gratitude to colleagues from the Marine Mammal Research Laboratory, Tropical Marine Science Institute (TMSI). To Suranga, thank you for your advice in formatting this thesis and your guidance in using LaTeX. Jolyn, thank you for your excellent support in setting up the equipment for experiments. Thanks, Petrina for also lending your support during the experiments. I appreciate their encouragement and moral support during the most difficult times.

I would also like to thank fellow colleagues from the other research laboratories in TMSI. The advice from Dr Mandar Chitre (Head, Acoustic Research Laboratory) in the early stages of the project has been invaluable on an academic level, for which I am extremely grateful. I show appreciation to Mr Roopsekhar (Physical Oceanography Research Laboratory) for allowing us to use PORL's water tank.

The echosounder unit used in the experiments was provided by Hydronav Services (Singapore) Pte Ltd. I appreciate their generous support in lending us the equipment unconditionally.

To my friends, especially Keddy, George, Carol, Lena, Edmund, Raymond, Pauline, Angela and Adrian. Thank you for your encouragement and the concern you have shown throughout this period. Thank you all for always believing in me.

Finally, I am truly grateful to my family for their encouragement and motivation. Their support and love brought me through many tough times.

Contents

Acknowledgements **i**

Summary **v**

List of Figures **viii**

List of Tables **xiv**

Abbreviations **xv**

Physical Constants **xvi**

Symbols **xvii**

1 Introduction **1**
1.1 Motivation for research 1
1.2 Thesis goals 4
1.3 Thesis organisation 6

2 Background and Related Work **8**
2.1 Marine mammal echolocation 8
2.1.1 Echolocation in marine mammals that also produce whistles 10
2.1.2 Echolocation in marine mammals that do not whistle 12
2.2 Bubbles in water and their dynamics 14
2.2.1 Properties of bubbles in the sea surface layer 14
2.2.2 Bubble dynamics 15
2.2.3 Equation of motion for different bubble models 18
2.3 Twin Inverted Pulse Sonar (TWIPS) technique 20

3 Simulation **26**
3.1 Simulation formulation 26
3.2 Scaling of equations in dimensionless variables 29
3.3 Signal processing 32
3.4 Verification of model by comparing with examples by Leighton *et al.* (2006) 35

3.4.1 Single bubble response 41
3.4.2 Bubble cloud response 45
3.5 Response from porpoise echolocation chirp 59
3.5.1 Single bubble response 62
3.5.2 Cloud response 70
3.6 Response from a typical dolphin echolocation click 87
3.6.1 Single bubble response 89
3.6.2 Cloud response 93
3.7 Simulation summary 99

4 Experiment **102**
4.1 Experimental setup 102
4.2 Experiment results - Bubble cloud response 107

5 Conclusion and Future Work **114**

A Formulating the modified Herring-Keller equation **117**

B Receiver Operating Characteristic (ROC) Curves **122**

Bibliography **126**

Summary

Marine mammals have been observed to hunt effectively in littoral environments where man-made sonar systems have always performed poorly. Surf zones and adjacent areas which form part of the littoral environment are particularly problematic because transmitted signals are affected by microbubble populated waters. Wave breaking is the dominant cause of bubble entrainment in the surf zone. The wave breaking process generates a large distribution of bubbles where larger bubbles tend to rise quickly to the surface while smaller 'microbubbles' persist for long periods of time. The difference in density and compressibility between air bubbles and seawater causes changes in velocity, scattering and absorption of sound waves which therefore complicates the use of sound underwater when compared to ideal 'bubble-free' environments.

Leighton first proposed the twin inverted pulse sonar (TWIPS) technique in 2004 [1], where he suggested exploiting the nonlinear nature of bubbles for contrast enhancement of a linear target buried in a cloud of bubbles. This technique involves the transmission of a pair of high amplitude pulses, one having reverse polarity with respect to the other. If the amplitude of this ensonification field is high enough, bubbles will generate nonlinear radial excursions while a linear target will scatter linearly. When the time histories are split in the middle and combined to make a time history half as long, enhancement and suppression occurs. Depending on the arithmetic operator used to combine the time histories, target backscatter is enhanced while bubble backscatter is suppressed or vice versa.

Leighton together with co-workers, subsequently published numerous papers on the TWIPS technique [2–13] and also filed for an international patent application in 2006 [14]. More details on the TWIPS technique was first described in [4] where the authors showed simulation results claiming that their technique outperformed the standard sonar processing technique. The patent application report [14] provided implementation details together with simulation and experimental results on TWIPS, but there was no thorough and quantitative measure of the performance of TWIPS compared with the standard sonar processing technique. In addition, the authors only discussed examples using windowed sine wave pulses at 6 and 300 kHz, although they also claimed that their method would work for any other type of pulses (chirps, pseudo-random noise sequences or M-sequences) with different time durations and operating at other frequencies.

This research thesis aims to provide a quantitative measure of the performance of TWIPS against other (simpler) signal processing techniques through the use of signal to noise (SNR) measurements and receiver operating characteristic (ROC) curves. This will be explored both by simulation and experiments in water populated by clouds of microbubbles. The model described by Leighton *et al.* in [14] will be used and one of the simulation examples will be reproduced in this project. Apart from the standard sonar processing technique and TWIPS discussed by the authors, several other processing techniques including: averaging and smoothing, bandpass filtering and standard cross correlation, have been introduced in this project for performance comparison. In addition, a new variant of TWIPS will be included for discussion.

To extend the scope of the techniques discussed, simulations will include applications using bio-mimetic sonar signals from two cetacean species: echolocation chirps from porpoises and echolocation clicks from dolphins. In general most species of porpoises produce echolocation chirps that have low sound pressure levels, narrower bandwidth and longer time duration compared to echolocation clicks produced by some species of dolphins. The use of these two types of bio-mimetic signals will provide insights on how bubble cloud backscatter will appear to these animals and whether the TWIPS technique would actually work if the animals do adopt TWIPS processing.

Experiments were conducted on a modified setup different from the model, but it was sufficient to illustrate the performance among the different signal processing techniques, which was found to agree with simulation results.

This study showed that TWIPS does outperform the 'standard sonar processing technique' defined in Leighton *et al.* (2005). However, it also showed that bandpass filtering or cross correlation methods performed better or equally well against TWIPS under conditions considered in the simulations and experiments. It is hoped that the studies here will offer alternative methods of processing sonar signals and statistical methods for the analysis of their performances. This would then help in the development of man-made sonar systems employing bio-mimetic signals that perform effectively in the littoral zone.

List of Figures

2.1 Waveform of a bottlenose dolphin (*Tursiops truncatus*) echolocation pulse. 11

2.2 Spectrum of a bottlenose dolphin (*Tursiops truncatus*) echolocation pulse. 11

2.3 Waveform of a finless porpoise (*Neophocaena phocaenoides*) echolocation pulse. 13

2.4 Spectrum of a finless porpoise (*Neophocaena phocaenoides*) echolocation pulse. 13

2.5 An illustration of the application of pulse inversion technique on linear and nonlinear scatterers. 22

3.1 Geometry of the model used in the simulations. 27

3.2 Waveforms illustrating the backscatter from bubbles with radii 10, 50, 100, 500, 1000 and 5000 μm, when driven by a positive and negative 6 kHz, 60 kPa windowed pulse. 42

3.3 Frequency response plots illustrating the backscatter from bubbles with radii 10, 50, 100, 500, 1000 and 5000 μm, when driven by a positive and negative 6 kHz, 60 kPa windowed pulse. 44

3.4 Frequency response plots illustrating the summation/subtraction of backscatter from bubbles with radii 10, 50, 100, 500, 1000 and 5000 μm, when driven by a positive and negative 6 kHz, 60 kPa windowed pulse. 46

3.5 An example plot showing the envelope of bubble cloud backscatter when a target is absent/present. 47

3.6 Corresponding waterfall plot of the example in Figure 3.5 when a target is (a) absent; (b)present. 48

3.7 Waterfall plot of bubble cloud backscatter from a 6 kHz, 60 kPa pulse using standard sonar processing when a target is (a) absent; (b) present (TS = -20 dB). 49

3.8 Magnitude response of a 6 kHz bandpass filter used in the simulations. 50

3.9 Waterfall plot of bubble cloud backscatter from a 6 kHz, 60 kPa pulse using TWIPS1a when a target is (a) absent; (b) present (TS = -20 dB). 50

3.10 Waterfall plot of bubble cloud backscatter from a 6 kHz, 60 kPa pulse using averaging and smoothing when a target is (a) absent; (b) present (TS = -20 dB). 51

3.11 Waterfall plot of bubble cloud backscatter from a 6 kHz, 60 kPa pulse using bandpass filtering when a target is (a) absent; (b) present (TS = -20 dB). 52

3.12 Waterfall plot of bubble cloud backscatter from a 6 kHz, 60 kPa pulse using cross correlation when a target is (a) absent; (b) present (TS = -20 dB). 53

3.13 6 kHz at 60 kPa pulse - Mean ROC curve with 95% CI (n = 50) at 0.1 FPR. 55

3.14 Waterfall plot of bubble cloud backscatter from a 6 kHz, 60 kPa pulse using TWIPS1b when a target is (a) absent; (b) present (TS = -20 dB). 58

3.15 6 kHz, 60 kPa pulse - Mean ROC curve with 95% CI (n = 50) at 0.1 FPR. 58

3.16 Comparison between the (a) waveform; (b) spectrum of a real and simulated porpoise chirp. 60

3.17 Waveforms illustrating the backscatter from bubbles with radii 10, 50, 100, 500, 1000 and 5000 μm, when driven by a positive and negative simulated porpoise chirp at 316 Pa. 63

3.18 Frequency response plots illustrating the backscatter from bubbles with radii 10, 50, 100, 500, 1000 and 5000 μm, when driven by a positive and negative simulated porpoise chirp at 316 Pa. 64

3.19 Frequency response plots illustrating the summation/subtraction of backscatter from bubbles with radii 10, 50, 100, 500, 1000 and 5000 μm, when driven by a positive and negative simulated porpoise chirp at 316 Pa. 65

3.20 Waveforms illustrating the backscatter from bubbles with radii 10, 50, 100, 500, 1000 and 5000 μm, when driven by a positive and negative simulated porpoise chirp at 10 kPa. 67

3.21 Frequency response plots illustrating the backscatter from bubbles with radii 10, 50, 100, 500, 1000 and 5000 μm, when driven by a positive and negative simulated porpoise chirp at 10 kPa. 68

3.22 Frequency response plots illustrating the summation/subtraction of backscatter from bubbles with radii 10, 50, 100, 500, 1000 and 5000 μm, when driven by a positive and negative simulated porpoise chirp at 10 kPa. 69

3.23 Magnitude response of a 125 kHz bandpass filter used in the simulations. 71

3.24 Waterfall plot of bubble cloud backscatter from a simulated porpoise chirp at 316 Pa using averaging and smoothing when a target is (a) absent; (b) present (TS = -20 dB). 72

3.25 Waterfall plot of bubble cloud backscatter from a simulated porpoise chirp at 316 Pa using bandpass filtering when a target is (a) absent; (b) present (TS = -20 dB). 72

3.26 Waterfall plot of bubble cloud backscatter from a simulated porpoise chirp at 316 Pa using cross correlation when a target is (a) absent; (b) present (TS = -20 dB). 73

3.27 Waterfall plot of bubble cloud backscatter from a simulated porpoise chirp at 316 Pa using standard sonar processing when a target is (a) absent; (b) present (TS = -20 dB). 73

3.28 Waterfall plot of bubble cloud backscatter from a simulated porpoise chirp at 316 Pa using TWIPS1a when a target is (a) absent; (b) present (TS = -20 dB). 74

3.29 Waterfall plot of bubble cloud backscatter from a simulated porpoise chirp at 316 Pa using TWIPS1b when a target is (a) absent; (b) present (TS = -20 dB). 74

3.30 Waterfall plot of bubble cloud backscatter from a simulated porpoise chirp at 316 Pa using averaging and smoothing when a target is (a) absent; (b) present (TS = -10 dB). 76

3.31 Waterfall plot of bubble cloud backscatter from a simulated porpoise chirp at 316 Pa using bandpass filtering when a target is (a) absent; (b) present (TS = -10 dB). 76

3.32 Waterfall plot of bubble cloud backscatter from a simulated porpoise chirp at 316 Pa using cross correlation when a target is (a) absent; (b) present (TS = -10 dB). 77

3.33 Waterfall plot of bubble cloud backscatter from a simulated porpoise chirp at 316 Pa using standard sonar processing when a target is (a) absent; (b) present (TS = -10 dB). 77

3.34 Waterfall plot of bubble cloud backscatter from a simulated porpoise chirp at 316 Pa using TWIPS1a when a target is (a) absent; (b) present (TS = -10 dB). 78

3.35 Waterfall plot of bubble cloud backscatter from a simulated porpoise chirp at 316 Pa using TWIPS1b when a target is (a) absent; (b) present (TS = -10 dB). 78

3.36 Simulated porpoise chirp at 316 Pa - Mean ROC curve with 95% CI (n = 50) at 0.1 FPR. 80

3.37 Waterfall plot of bubble cloud backscatter from a simulated porpoise chirp at 10 kPa using averaging and smoothing when a target is (a) absent; (b) present (TS = -10 dB). 82

3.38 Waterfall plot of bubble cloud backscatter from a simulated porpoise chirp at 10 kPa using bandpass filtering when a target is (a) absent; (b) present (TS = -10 dB). 82

3.39 Waterfall plot of bubble cloud backscatter from a simulated porpoise chirp at 10 kPa using cross correlation when a target is (a) absent; (b) present (TS = -10 dB). 83

3.40 Waterfall plot of bubble cloud backscatter from a simulated porpoise chirp at 10 kPa using standard sonar processing when a target is (a) absent; (b) present (TS = -10 dB). 83

3.41 Waterfall plot of bubble cloud backscatter from a simulated porpoise chirp at 10 kPa using TWIPS1a when a target is (a) absent; (b) present (TS = -10 dB). 84

3.42 Waterfall plot of bubble cloud backscatter from a simulated porpoise chirp at 10 kPa using TWIPS1b when a target is (a) absent; (b) present (TS = -10 dB). 84

3.43 Simulated porpoise chirp at 10 kPa - Mean ROC curve with 95% CI (n = 50) at 0.1 FPR. 86

3.44 Simulated dolphin click (a) waveform; (b) spectrum 88

3.45 Waveforms illustrating the backscatter from bubbles with radii 10, 50, 100, 500, 1000 and 5000 μm, when driven by a positive and negative simulated dolphin click at 100 kPa. 90

3.46 Frequency response plots illustrating the backscatter from bubbles with radii 10, 50, 100, 500, 1000 and 5000 μm, when driven by a positive and negative simulated dolphin click at 100 kPa. 91

3.47 Frequency response plots illustrating the summation and subtraction of backscatter from bubbles with radii 10, 50, 100, 500, 1000 and 5000 μm, when driven by a positive and negative simulated dolphin click at 100 kPa. 92

3.48 Waterfall plot of bubble cloud backscatter from a simulated dolphin click at 10 kPa using averaging and smoothing when a target is (a) absent; (b) present (TS = -15 dB). 95

3.49 Waterfall plot of bubble cloud backscatter from a simulated dolphin click at 10 kPa using bandpass filtering when a target is (a) absent; (b) present (TS = -15 dB). 95

3.50 Waterfall plot of bubble cloud backscatter from a simulated dolphin click at 10 kPa using cross correlation when a target is (a) absent; (b) present (TS = -15 dB). 96

3.51 Waterfall plot of bubble cloud backscatter from a simulated dolphin click at 10 kPa using standard sonar processing when a target is (a) absent; (b) present (TS = -15 dB). 96

3.52 Waterfall plot of bubble cloud backscatter from a simulated dolphin click at 10 kPa using TWIPS1a when a target is (a) absent; (b) present (TS = -15 dB). 97

3.53 Waterfall plot of bubble cloud backscatter from a simulated dolphin click at 10 kPa using TWIPS1b when a target is (a) absent; (b) present (TS = -15 dB). 97

3.54 Simulated dolphin click at 100 kPa - Mean ROC curve with 95% CI (n = 50) at 0.1 FPR. 99

4.1 Block diagram showing the experiment setup. 104

4.2 Source level measured at position occupied by target. 105

4.3 Waveform of the driving pulse used in the experiment. 106

4.4 Waveform of the backscatter from the bubble cloud used in the experiment. 106

4.5 Frequency response of the bubble cloud used in the experiment. . . 107

4.6 Waterfall plot of bubble cloud backscatter from experiment driving pulse using averaging and smoothing when a target is (a) absent; (b) present. 109

4.7 Waterfall plot of bubble cloud backscatter from experiment driving pulse using bandpass filtering when a target is (a) absent; (b) present. 109

4.8 Waterfall plot of bubble cloud backscatter from experiment driving pulse using cross correlation when a target is (a) absent; (b) present. 110

4.9 Waterfall plot of bubble cloud backscatter from experiment driving pulse using standard sonar processing when a target is (a) absent; (b) present. 110

4.10 Waterfall plot of bubble cloud backscatter from experiment driving pulse using TWIPS1a when a target is (a) absent; (b) present. . . . 111

4.11 Waterfall plot of bubble cloud backscatter from experiment driving pulse using TWIPS1b when a target is (a) absent; (b) present. . . . 111

4.12 Experiment data - ROC curve. 113

B.1 Confusion Matrix 123

List of Tables

2.1 Properties of bubble plumes 14

3.1 Bubble population distribution described by Leighton *et al.* (2006) 38

3.2 Bubble population distribution calculated using Equation 3.1 39

3.3 Comparison of SNR for different processing methods - 6 kHz at 60 kPa driving pulse. 54

3.4 Comparison of SNR for different processing methods - simulated porpoise chirp at 316 Pa. 79

3.5 Comparison of SNR for different processing methods - simulated porpoise chirp at 10 kPa. 85

3.6 Comparison of SNR for different processing methods - simulated dolphin click at 100 kPa. 98

3.7 Summary of SNR comparison on different processing methods using different driving pulse. 100

4.1 Comparison of SNR for different processing methods applied on experiment data. 112

Abbreviations

AUC	**A**rea **U**nder **C**urve
CI	**C**onfidence **I**nterval
FIR	**F**inite **I**mpulse (R)esponse
FP	**F**alse **P**ositive
FPR	**F**alse **P**ositive **R**ate
FN	**F**alse **N**egative
M-sequence	**M**aximum length sequence
ROC curves	**R**eceiver **O**perating **C**haracteristic curves
SNR	**S**ignal to **N**oise **R**atio
SONAR	**SO**und **N**avigation **A**nd **R**anging
TP	**T**rue **P**ositive
TPR	**T**rue **P**ositive **R**ate
TN	**T**rue **N**egative
TS	**T**arget **S**trength
TWIPS	**TW**in **I**nverted **P**ulse **S**onar

Physical Constants

Speed of Sound in Seawater	c	=	1540 m s^{-1}
Hydrostatic Pressure	p_0	=	101 300 Pa
Polytropic Exponent of Gas	κ	=	1.0
Density of Seawater	ρ	=	1 025 kg m^{-3}
Viscosity	η	=	0.0 010 Ns m^{-2}
Surface Tension	σ	=	0.075 N m^{-1}

Symbols

a_0	Resonance bubble radius
a	Bubble radius
a_e	Bubble radius at equilibrium
$\dot{a}$	First order derivative of bubble radius (bubble wall velocity)
$\ddot{a}$	Second order derivative of bubble radius (bubble wall acceleration)
C	Time dependant speed of sound
c	Speed of sound in liquid
η	Shear viscosity
γ	Normalised speed of sound
h	Liquid enthalpy
κ	Polytropic exponent of gas
ω_0	Resonance frequency
Φ	Velocity potential
p_0	Atmospheric pressure
p_A	Driving pressure including ambient pressure
p_g	Instantaneous gas pressure within a pulsating bubble
p_i	Driving pressure
$p_{i,e}$	Equilibrium pressure inside bubble
p_∞	Far field pressure
p_L	Liquid pressure at the bubble wall
q	Normalised pressure
q_L	Normalised pressure at bubble surface
ρ	Density of water

r	range distance from bubble center
σ	Surface tension
S	Normalised surface tension
t	Time
τ	Dimensionless time
u	Particle velocity
v_L	Normalised shear viscosity of liquid
x'	Time differentiation

Chapter 1

Introduction

1.1 Motivation for research

Acoustics play an important and necessary part in our daily lives. Mankind has evolved to use speech as the main communication channel for social interaction among individuals. This ability is not limited to the human species as animals, too, have evolved a complex set of vocal tools to assist in their social interactions. In addition, some species of animals have evolved a highly complex neural-audio system to replace vision. Most bats and some species of marine mammals are able to use sound to aid in their navigation, and to detect objects in extreme harsh environments where vision is obscure, such as at night. For marine mammals in particular, the use of vision is extremely limited in the underwater environment, especially in deep waters where there is little illumination, or in waters with high turbidity due to sediments and phytoplankton. To overcome this problem, some

species of marine mammals use sound in the form of echolocation signals to replace or supplement their sense of sight underwater.

Humans also possess the innate ability to use echolocation signals for navigation and detection in their surroundings. However, they have evolved to primarily use their sense of sight for this purpose because of the abundance of light and clarity in the environment they live in. Nevertheless, there have been numerous reports of vision-impaired humans employing echolocation to replace their sense of sight. One of the earliest documented cases of a blind person using echolocation was James Holman (1786-1857), who used the sound of a tapping cane to sense his environment [16].

Advancements in technology have allowed humans to re-create the underwater echolocation ability of marine mammals to some extent. These man-made (SONAR) systems can outperform marine mammal echolocation in some aspects but they also have limitations which make them inferior under some circumstances. One of the major problems faced by man-made sonar is the effect of noise caused by scattering. This problem has the greatest impact in shallow waters (surf zone) where there can be a large number of bubbles in the water.

Bubbles are efficient scatterers of sound in water because of the impedance mismatch at the liquid/gas interface. Bubbles are formed by natural processes that include rainfall, gas emission from the sea bed, boat wakes, living or decomposing organisms, and wave breaking; the latter being the dominant cause of bubble entrainment in the surf zone. Despite the complications of sound propagation in bubble populated water, some species of cetaceans are still observed to hunt

efficiently in shallow coastal waters and in biologically active rivers where bubbles persist. In contrast, the performance of man-made sonar systems has always been greatly handicapped by this phenomenon. How cetaceans manage to overcome the problem is still largely unknown but scientists have proposed techniques that might give a possible explanation.

Leighton first suggested the use of pulse inversion techniques for contrast enhancement in the surf zone in 2004 [1]. The basic concept of pulse inversion is not novel and was in fact first proposed and applied in biomedical applications for the detection of contrast agents in blood. He proposed the twin inverted pulse sonar (TWIPS) technique, which is a set signal processing algorithms applied to the backscatter from a pair of closely-spaced, high amplitude transmit pulse of opposite polarity. It was suggested that the algorithm could help to either enhance linear scattering from targets while suppressing non-linear scattering from bubbles, or vice versa. In subsequent publications on TWIPS [3–13], Leighton and co-workers showed that TWIPS performed better than their definition of 'standard sonar processing technique' both in simulations and experiments on target contrast enhancement in microbubble populated water. They also suggested the possibility of marine mammals adopting pulse inversion techniques for detecting prey, which they hoped to further explore.

1.2 Thesis goals

The work by Leighton and co-workers used non-biomimetic signals. In their simulations and experiments, they tested the proposed TWIPS technique using windowed sine wave pulses with centre frequencies of 6 kHz and 300 kHz for probing a linear target hidden in a non-homogeneous spherical bubble cloud. The authors suggested that their technique would work for pulses with centre frequencies within the 6 - 300 kHz range, but they did not describe an assessment of how the technique would perform using marine mammal bio-mimetic echolocation pulses. A quantitative analysis of the performance of TWIPS compared to other existing methods was also unavailable. In [4], the authors mentions the possibility that odontocetes (a sub-order of marine mammals under the Cetacea order) producing multiple pulses, but no further work on this has been discussed in their subsequent publications.

A literature search showed that six species of dolphins and porpoises have been reported to use multiple echolocation pulses [17–19]. Echolocation signals in marine mammals differ among different species but they can be classified into two general categories. The first category refers to signals of dolphins that are capable of whistling and the second category refers to signals of dolphins that do not whistle [20]. Echolocation signals belonging to marine mammals from the first category are characterised by high amplitude, broad bandwidth and short duration. On the other hand, echolocation signals produced by marine mammals in the second category have a much lower amplitude, narrower bandwidth and longer duration.

This thesis builds upon the concept of TWIPS by providing a method of evaluating TWIPS compared to the standard sonar processing technique and also other signal processing techniques not compared previously, such as standard averaging and smoothing, bandpass filtering and standard cross correlation. In addition, a discussion of these processing techniques applied to bubble clouds in response to echolocation signals from two species of marine mammals will be given. In order to achieve this, a simulation of the model described by Leighton *et al.*(2006) [14] was developed. One of the examples given in [14] was tested to verify the model, after which it was used to evaluate bubble cloud response from bio-mimetic echolocation pulses. Experiments were also conducted to compare results from simulations.

The list below summarises the objectives of this research thesis:

- Reproduce and clarify the model described by Leighton *et al.* [14] using MATLAB. Verify the model by comparing simulation results with those obtained in [14].
- Simulate and compute the backscatter pressure amplitude of single bubbles in a range of defined radii, and a target hidden in the centre of a spherical bubble cloud with an internally consistent dispersion of bubbles consisting of the same range of defined radii, when driven by a simulated porpoise echolocation chirp.
- Simulate and compute the backscatter pressure amplitude of single bubbles in a range of defined radii, and a target hidden in the centre of a spherical bubble cloud with an internally consistent dispersion of bubbles consisting

of the same range of defined radii, when driven by a simulated dolphin echolocation click.

- Conduct experiments to measure the backscatter pressure amplitude from a target hidden inside/behind a machine-generated bubble cloud when driven by a signal from an echosounder unit.

- For all simulations and experiments, apply standard sonar processing and TWIPS1 for evaluating target/bubble contrast enhancement. In addition, introduce other signal processing methods to compare against standard sonar processing and TWIPS1. Evaluate and compare the performance of these various methods by measuring the signal to noise ratio (SNR) between backscatter from target and bubbles. Plot the receiver operating characteristics (ROC) curves to further assess the detection performance.

1.3 Thesis organisation

The thesis is organised as follows:

- Chapter 1 - Introduction

  The motivation for this research project is discussed and objectives of the thesis defined.

- Chapter 2 - Background and Related Work

  Background information related to the research topic is presented in detail.

Topics include echolocation signals in marine mammal, bubble properties and its dynamics, and TWIPS.

- Chapter 3 - Simulation

  A model of the problem is implemented and simulations are performed to verify the model. Apply the model in simulations using bio-mimetic sonar pulses. Report on target detection performance between various signal processing techniques for target contrast enhancement.

- Chapter 4 -Experiment

  Conduct an experiment based on a modified model used in the simulations. Report on target detection performance between various signal processing techniques for target contrast enhancement.

- Chapter 5 - Conclusion

  A conclusion of current research outcomes and a discussion of future work will be provided.

Chapter 2

Background and Related Work

2.1 Marine mammal echolocation

Marine mammals include a diverse assemblage of species that have representatives in three mammalian orders. The order Carnivora is made up of three subgroups consisting of the superfamily Pinnipedia (seals, sea lions and walruses), family Mustelidae (sea otter and marine otter) and family Ursidae (polar bear). The order Cetacea comprises of two suborders, Mysticeti (Baleen whales) and Odontoceti (Tooth whales). Whales, dolphins and porpoises fall into the Cetacea order. Finally, the order Sirenia is composed of sea cows (manatees and dugongs).

Dolphins produce sound that can be classified into two broad categories. The first type is frequency-modulated signals of moderately long duration lasting between one-tenth of a second to several seconds, which are referred to as whistles. They are suggested to be used for intraspecific communications [21]. The second

type is characterised by broadband impulses in the ultrasonic frequency range with very short durations (in the order of microseconds) and high sound intensity which are referred to as echolocation clicks. They are used mainly for navigation and detection.

Echolocation is the process of projecting acoustic signals and sensing the surrounding environment from the echoes. Acoustic energy propagates most efficiently in water compared to other forms of energy. As such, it is no surprise that many marine mammals have evolved to use sound to replace their sense of sight for navigation and detection underwater when conditions are unfavorable for vision. Most species of river dolphin in particular have very poorly developed vision. The Ganges river dolphin (*Platanista gangetica*), for example, is reported to not possess a pair of crystalline eye lenses [22].

Echolocation signals can be further classified into two general categories. The first category is signals of dolphins that are capable of whistling and the second category is signals of dolphins that do not whistle. Some species that fall into the first category where echolocation signals have been measured include the bottlenose dolphin, beluga whale, killer whale, false killer whale, Pacific whitesided dolphin, Amazon River dolphin, Risso's dolphin, tucuxi, Atlantic spotted dolphin, Pacific spotted dolphin, spinner dolphin, pilot whale, rough tooth dolphin and Chinese river dolphin. Species that fall under the second category include the harbor porpoise, finless porpoise, Dall's porpoise, Commerson's dolphin and pygmy sperm whale. The echolocation signals from the second category compared to

those from the first category are of a longer duration, narrower bandwidth and lower intensity [20].

2.1.1 Echolocation in marine mammals that also produce whistles

Echolocation signals from this category of marine mammals vary slightly among species but generally have some common features that distinguish them from the other category. In general, the waveform of echolocation clicks from this group of marine mammals typically have less than 3 to 5 cycles, with the first cycle reaching its maximum amplitude (oligocyclic waveform). They have broad bandwidth and high sound intensity.

Echolocation signals emitted by two Atlantic bottlenose dolphins (*Tursiops truncatus*) were made by Au *et al.* (1974) during a target detection experiment in open waters of Kaneohe Bay, Oahu, Hawaii [23]. The signals were observed to have peak frequencies ranging from 120 to 130 kHz and an average peak-to-peak click level in the order of 220 dB re 1 μPa @ 1 m. Another set of signals recorded from the same species was describe by Au (1980), where signals were observed to have peak frequencies ranging from 110 to 130 kHz and an average peak-to-peak click level of 228 dB re 1 μPa @ 1 m. These clicks have a 3 dB bandwidth from 30 to 60 kHz and have durations approximately between 50 to 80 μs [24].

The waveform and spectrum of a representative echolocation click from a bottlenose dolphin (*Tursiops truncatus*) recorded in the open sea are shown in Figures 2.1 and 2.2, respectively.

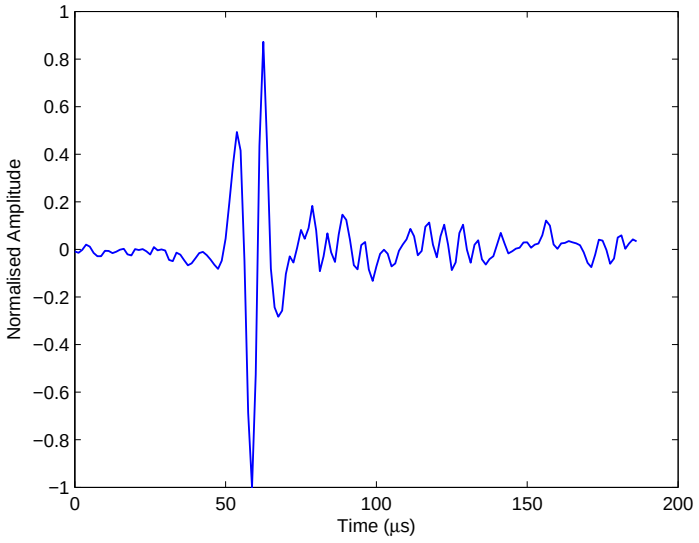

FIGURE 2.1: Waveform of a bottlenose dolphin (*Tursiops truncatus*) echolocation pulse. *(Provided by Ms Simone Baumann, Eberhard-Karls-Universitt Tbingen, Germany in cooperation with Scripps Institution of Oceanography)*

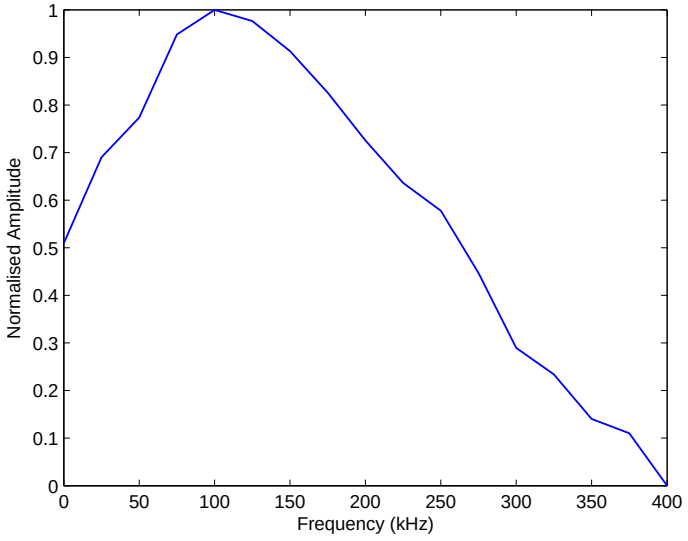

FIGURE 2.2: Spectrum of a bottlenose dolphin (*Tursiops truncatus*) echolocation pulse.

2.1.2 Echolocation in marine mammals that do not whistle

Most species of porpoises fall into this category. The echolocation waveform envelope increases in amplitude from the first few cycles and decays exponentially (polycyclic waveform). This type of echolocation signal is referred to as an 'echolocation chirp' and it generally has a narrow frequency range and long duration. The reason for porpoises using long duration, narrow bandwidth signal may be related to their relatively small body size. This is because for a given amplitude, the energy in a signal is directly proportional to its duration [20].

Echolocation signals of finless porpoise (*Neophocaena phocaenoides*) measured in open waters were reported by Li *et al.* (2005).The peak frequency typically ranges from 87 to 145 kHz with an average of 125 $\pm$ 6.92 kHz and the 3dB bandwidth ranged from 15 to 25 kHz with an average of 20 $\pm$ 4.24 kHz. The duration of these signals was 30 to 122 μs with an average of 68 $\pm$ 14.12 μs [25]. Peak to peak sound pressure levels measured by Li *et al.* (2006) were estimated to range from 163.7 to 185.6 dB re 1 μPa @ 1 m [26]. The waveform and spectrum of a representative echolocation pulse recorded from *Neophocaena phocaenoides* in open waters are given in Figures 2.3 and 2.4 respectively.

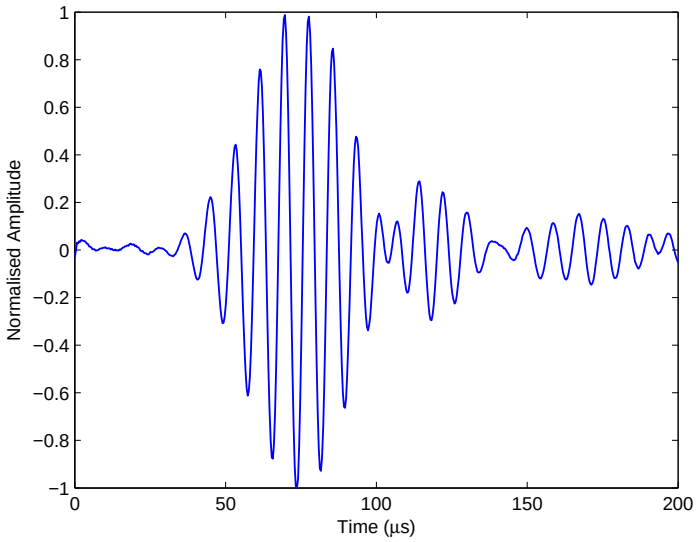

FIGURE 2.3: Waveform of a finless porpoise (*Neophocaena phocaenoides*) echolocation pulse. *(Provided by Dr Tomonari Akamatsu, National Research Institute of Fisheries Engineering, Fisheries Research Agency, Japan).*

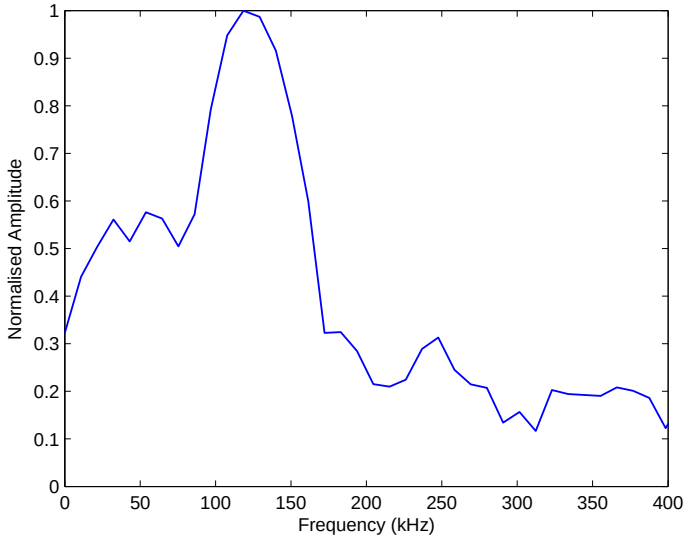

FIGURE 2.4: Spectrum of a finless porpoise (*Neophocaena phocaenoides*) echolocation pulse.

2.2 Bubbles in water and their dynamics

2.2.1 Properties of bubbles in the sea surface layer

Wave breaking is the dominant cause of bubble entrainment in the surf zone. These assemblages of bubbles are often referred to as clouds or plumes. Monahan [15] proposed the existence of three types of bubble plumes (α, β and γ). He went on to associate two of these bubble plumes with stages of whitecaps. A stage A whitecap occurs with the crest of a spilling breaker producing α-plumes at the subsurface extension. These α-plumes have the highest void fraction $O(10^{-1} - 10^{-2})$ and have a lifetime of less than 1 s. A stage A whitecap then evolves into a foam patch to become a stage B whitecap where the *alpha*-plumes decay into β-plumes which are attached to the foam patch. β-plumes have a much smaller void fraction $O(10^{-3} - 10^{-4})$ and have a lifetime of approximately 4 s. In addition, they are spatially larger than α-plumes. γ-plumes evolve from β-plumes and form when the latter detach from the whitecap. γ-plumes have the lowest void fraction $O(10^{-7} - 10^{-7})$, lifetimes 10 - 100 times longer than a β-plume and the largest spatial dimensions. γ-plumes eventually decay into a weak background layer. A summary of the properties of bubble plumes is given in Table 2.1.

TABLE 2.1: Properties of bubble plumes (*reproduced from Monahan [15]*).

	α-plume	β-plume	γ-plume	background
Horizontal area (m^2)	$0.2 - 1$	$8 - 50$	$100 - 500$	-
Vertical scale (m)	-	0.8	$0.42 - 0.75$	-
Time scale (s)	1.0	$3.5 - 4.3$	$100 - 1000$	-
Void fraction	$4^{-2} - 4^{-2}$	$10^{-3} - 10^{-4}$	$10^{-7} - 10^{-6}$	$10^{-9} - 10^{-8}$
n(a=100μm) ($m^{-3}\mu m^{-1}$)	$10^{7} - 10^{-8}$	$10^{5} - 10^{6}$	$10^{2} - 10^{4}$	10

γ-plumes dominate in the subsurface (surf zone) because of their spatial dimension and lifetime. As such, measurements of bubble population distribution often give results that coincide with descriptions of γ-plumes. The simulations discussed in the later chapters uses bubble population distributions that are similar to γ-plumes.

2.2.2 Bubble dynamics

In the study of bubble dynamics, one observes the behaviour of gaseous cavities within a body of liquid when subjected to an acoustic disturbance. A time-varying, generally directional sinusoidal pressure source is superimposed onto the ambient pressure causing any cavities present (bubbles of gas in the liquid medium) of an appropriate size to be in set into a state of motion in which both expansion and contraction phases are present. This behavior is defined as bubble oscillation.

One of the important factors that determine the response of a bubble is the relationship between the frequency of the external oscillating pressure field and the natural resonance frequency of the bubble. A bubble will oscillate most when driven by a signal whose frequency matches its natural resonance frequency. The other factor is the amplitude of the signal which, together with the driving frequency, determines whether a bubble will undergo linear or non-linear oscillations.

A gas bubble in a liquid acts like an oscillator. Minnaert (1993) was the first to calculate the natural frequency of a spherical gas bubble in a liquid [27]. The

Minnaert resonance frequency is defined as

$$w_0 = \frac{1}{a_0}\sqrt{\frac{3\kappa p_{i,e}}{\rho}} \tag{2.1}$$

where w_0 is the resonance frequency, a_0 is the resonance bubble radius, κ is the polytropic exponent of gas, $p_{i,e}$ is the equilibrium pressure inside bubble and ρ is the density of water.

Another form of the equation taking surface tension into consideration is

$$w_0 = \frac{1}{a_0}\sqrt{\frac{3\kappa p_{i,e}}{\rho} - \frac{2\sigma}{p_0 a_0}} \tag{2.2}$$

where σ is the surface tension and p_0 is the atmospheric pressure.

A bubble's natural frequency is a function of its radius as shown in Eq. 2.1 and 2.2. Knowledge of the range of bubble radii in a bubble cluster will help determine the range of frequencies favourable for generating non-linear responses. Bubbles found commonly in the ocean are dominated by those with radii ranging from 10 to 100 μm. This was found from experimental measurements of bubble populations in the field made separately by several investigators including Phelps and Leighton 1998 [28], Farmer and Vagle 1989 [29], Leighton *et al.* 1996 [30, 31] and Meers *et al.* 2001 [32]. A figure comparing the bubble population density made by these investigators can be found in [32].

Resonance oscillation can occur when the frequency of the driving pulse matches the natural (resonance) frequency of the bubble. A bubble driven at or close to its resonance frequency will have a response which is primarily a function of damping

by the medium in which it is suspended. Given that viscous damping is small in most practical circumstances, the bubble will undergo large oscillations exceeding its critical size. This results in a highly nonlinear scattering response.

The review by Plesset and Prosperetti (1977) [33] discussed several interesting and important nonlinear phenomena in single bubbles. They found that with increase in amplitude of the driving pressure, single bubbles can be driven into nonlinear oscillations resulting in harmonic dispersions. These harmonic dispersions occur at frequencies in integer multiples of the driving frequency (super-harmonics) and more unusually, at frequencies less than the driving frequency (sub-harmonics). Both the super-harmonics and sub-harmonics become more prominent as the driving amplitude is increased.

In the dynamic problem of acoustic cavitation and bubble oscillation, one is interested to find the pressure and velocity field together with the radical motion of the bubble wall when excited by a time-dependent acoustic pressure field. For simplification, bubbles are often assumed to be spherical and always remain spherical. The equations of motion for the liquid are derived from conservation equations for mass and momentum, and from equations of state for the liquid. These equations give the relationship between changes in enthalpy, density and pressure in the liquid. By combining these basic equations and making some simplification assumptions, the partial differential equations describing the motion of the liquid are reduced to an ordinary differential equation describing the bubble radius as a function of time. The equation of motion for an ideal bubble will be discussed in the following section.

2.2.3 Equation of motion for different bubble models

A number of bubble models have been developed over time. They differ in complexity and make different assumptions. Lord Rayleigh was the first to mathematically describe bubble oscillations [34]. Rayleigh's model assumed that the liquid medium is incompressible, which infers an infinite velocity of sound. This assumption only gives satisfactory results for small amplitudes of oscillations. The motion of a bubble wall described by Rayleigh is given as

$$\ddot{a}a + \frac{3}{2}\dot{a}^2 = \frac{1}{\rho}(p_L - p_\infty) \tag{2.3}$$

where a is the bubble radius, $\dot{a}$ is the first order derivative of bubble radius, $\ddot{a}$ is the second order derivative of bubble radius, p_L is the liquid pressure at the bubble wall and p_∞ is the far field pressure.

Thirty years after Rayleigh published this concept, significant improvements were made to his equation. Plesset (1949) [35] modified the equation by adding a variable pressure term and surface tension term. This, together with a viscous damping term added by Poritsky (1952) [36] is known as the Rayleigh-Plesset equation. It is given as

$$\ddot{a}a + \frac{3}{2}\dot{a}^2 = \frac{1}{\rho}\left(p_g(t) - p_A(t) - \frac{2\sigma}{a} - \frac{4\eta\dot{a}}{a}\right) \tag{2.4}$$

where p_g is the instantaneous gas pressure inside the bubble, p_A is the driving pressure including ambient pressure and η is the shear viscosity.

Another common bubble model is that of Gilmore (1952) [37]. In this model, the velocity of sound in the liquid varies with pressure. Gilmore also considered the enthalpy difference H, between liquid at pressures under isentropic conditions. The equation of motion in Gilmore's model is given as

$$a\ddot{a}\left(1-\frac{\dot{a}}{C}\right)+\frac{3}{2}\dot{a^2}\left(1-\frac{1}{3}\frac{\dot{a}}{C}\right)=h\left(1+\frac{\dot{a}}{C}\right)+\frac{a}{C}\dot{h}\left(1-\frac{\dot{a}}{C}\right) \tag{2.5}$$

where C is the time dependant speed of sound and h is the liquid enthalpy.

Keller and Miksis (1980) [38] produced a radial equation based on the assumption of a constant speed of sound in the liquid. This equation is suitable for large amplitude forced oscillations and incorporates the effects of acoustic radiation by the bubble. It also uses the approximation of a linear polytropic index. Prosperetti (1984) [39] modified this equation which was based on the original formulations by Herring (1941) [40], to incorporate a more exact formulation for the internal pressure. This modified Herring-Keller equation is given as

$$a\ddot{a}\left(1-\frac{\dot{a}}{c}\right)+\frac{3}{2}\dot{a^2}\left(1-\frac{1}{3}\frac{\dot{a}}{c}\right)=\left(1+\frac{\dot{a}}{c}\right)\frac{1}{\rho}\left(p_L-p_0-p_i\left(t+\frac{a}{c}\right)\right)+\frac{a}{\rho c}\frac{\partial p_L(t)}{\partial t} \tag{2.6}$$

where c is the speed of sound in liquid and t is the time.

The modified Herring-Keller equation was chosen for describing the bubble motion in this research project since it is suitable for large amplitude forced oscillations caused by echolocation signals at close range. In addition, this equation is easier to implement compared to the Gilmore model. The derivation of the modified Herring-Keller equation from fundamental equations is given in Appendix

A.

2.3 Twin Inverted Pulse Sonar (TWIPS) technique

The twin inverted pulse sonar (TWIPS) technique in summary, involves the transmission of a pair of closely-spaced pulses of opposite polarity and then applying signal processing techniques to the backscatter signal to either enhance linear scattering from targets while suppressing non-linear scattering from bubbles or vice versa. This technique operates on the basic concept of pulse inversion imaging used in the detection of microbubble contrast agents in medical ultrasound.

In pulse inversion imaging for medical ultrasound, a pair of consecutive ultrasound pulse of opposite polarity is transmitted and their echoes added together. In the case of linear scattering, the echoes will be of opposite polarity and the addition of these echoes will cause them to cancel each other almost completely. On the other hand, for non-linear scattering, the echoes will not cancel each other to the same extent because the responses from the positive and negative pulse differ in phase and amplitude.

Following the same basic principle of pulse inversion imaging in medical ultrasound diagnosis, it might be possible to enhance linear scattering and suppress nonlinear scattering by applying the subtraction operator to echoes from successive inverted driving pulses. The key to enhancing the ability to detect linear targets

in bubbly water is to ensure that bubbles scatter energy nonlinearly and the target in question scatters energy linearly with respect to the source of ensonification. One point of interest is to observe that nonlinearity in the bubble response is asymmetrical about the zero-pressure axis compared to linear scattering which is symmetrical about the zero-pressure axis. Applying the subtraction operator to linear scatter from pulses of opposite polarity doubles its original amplitude. On the other hand, with the nonlinear scatter being asymmetrical, the subtraction operator would result in the suppression of even harmonics components.

The pulse inversion technique is illustrated in Figure 2.5.

TWIPS has been proposed as a method that outperforms the use of a standard correlator [14]. There are two basic subdivisions, TWIPS1 and TWIPS2. Their mathematical formulations are described as follows.

The transmitted pulse, $P(t)$, consist of two pressure components of opposite polarity and after a time delay of t_1 after each other

$$P(t) = \Gamma(t) - \Gamma(t - t_1) \tag{2.7}$$

The received signal is denoted as $P_{RX}(t)$, consisting of a linear (target) and non-linear (bubbles) component

$$P_{RX}(t) = P_l(t) + P_{nl}(t) \tag{2.8}$$

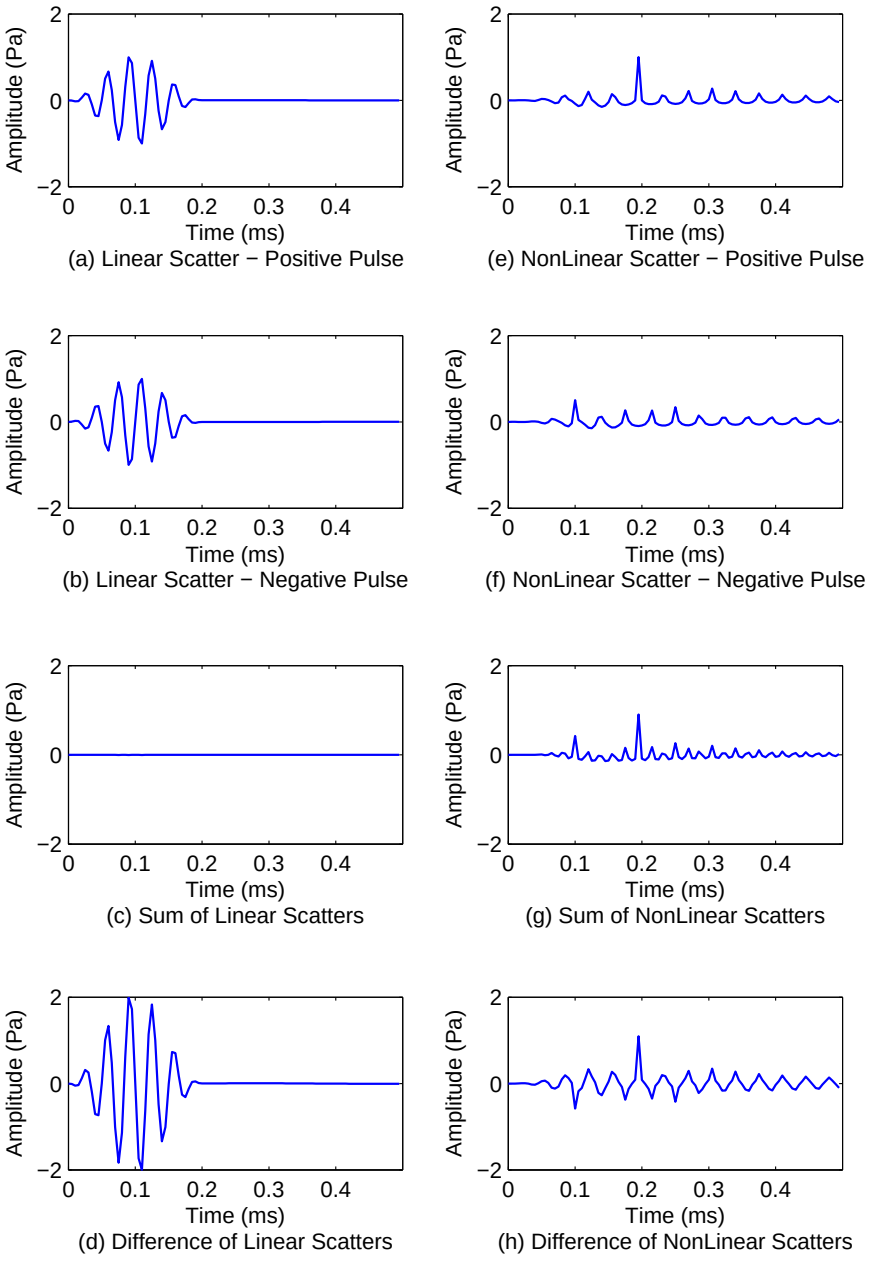

FIGURE 2.5: An illustration of the application of pulse inversion technique on linear and nonlinear scatterers.

The linear component $P_l(t)$ is a scaled version of the transmitted signal arriving after a time delay τ

$$P_l(t) = s_T P(t-\tau) = s_T(\Gamma(t-\tau) - \Gamma(t-t_1-\tau)) \tag{2.9}$$

where s is a constant scaling factor and τ is the two way travel time between source/receiver and the scatterer.

The nonlinear component is assumed to be nonlinearly related to the incident pulse such that the pressure contribution from it at the receiver can be expressed as a power series

$$\begin{aligned} P_{nl}(t) =& s_1 P(t) + s_2 P^2(t) + s_3 P^3(t) + s_4 P^4(t)... \\ =& s_1[\Gamma(t) - \Gamma(t-t_1)] + s_2[\Gamma(t) - \Gamma(t-t_1)]^2 \\ &+ s_3[\Gamma(t) - \Gamma(t-t_1)]^3 + s_4[\Gamma(t) - \Gamma(t-t_1)]^4 + ... \end{aligned} \tag{2.10}$$

τ is assumed to be zero for notational simplicity

The delay t_1 is assumed to be sufficiently large so that Γ_t and Γ_{t-t_1} are never simultaneously non zero

$$\begin{aligned} P_{nl}(t) =& s_1\Gamma(t) - s_1\Gamma(t-t_1) + s_2\Gamma^2(t) + s_2\Gamma^2(t-t_1) \\ &+ s_3\Gamma^3(t) - s_3\Gamma^3(t-t_1) + s_4\Gamma^4(t) + s_4\Gamma^4(t-t_1) + ... \\ =& s_1\Gamma(t) + s_2\Gamma^2(t) + s_3\Gamma^3(t) + s_4\Gamma^4(t) + \\ &... - s_1\Gamma(t-t_1) + s_2\Gamma^2(t-t_1) - s_3\Gamma^3(t-t_1) + s_4\Gamma^4(t-t_1) + ... \end{aligned} \tag{2.11}$$

The most basic subdivision of TWIPS, referred to as TWIPS1, involves a simple addition or subtraction operation between the first and second pulse in the received signal. In the case of the subtraction operator applied on the backscatter from a linearly scattering target, the following is obtained

$$P_{l-}(t) = P_{RX}(t) - P_{RX}(t+t_1) = s_T[\Gamma(t) - (-\Gamma(t))] = 2s_T\Gamma(t),\ 0 \leq t \leq t_1 \quad (2.12)$$

It can be observed that subtracting the received pulses enhances the signal from the linear scatterer. Applying the same subtraction operation on the nonlinear scattering component enhances contributions from the linear and odd-powered nonlinearities. The even-powered nonlinearities are suppressed.

The converse is true if the addition operation is applied to the received pulses. In this case, the even powered nonlinearities from the bubbles are enhanced and the linear scatter is suppressed.

There is the other subdivision of TWIPS, referred to TWIPS2, which is formed by the ratio of P_+, and P_- . The ratio P_-/P_+, for example, further enhances the detection of linear targets while the ratio P_+/P_- further enhances the detection of bubbles. Other combinations are possible such as P_+^2/P_-^2 and P_-^2/P_+^2, and powers of these ratios. The formation of this ratio has to be applied carefully because this method can lead to a magnification of noise in the signal. This is because the statistical distribution of noise at the output can be highly non-Gaussian. Impulsive noise may result, leading to an increase in the false alarm rate. TWIPS2

gives a much greater contrast in detection but at the expense of an increase in false detection rate.

TWIPS has been implemented on simulated data and verified experimentally by Leighton and co-workers. A description of the implementation of TWIPS together with simulation and experiment results are available in their patent application [14]. In this research thesis, only TWIPS1 will be discussed because TWIPS2 gives a high false detection rate at the expense of greater target contrast. Comparisons of performance among the different signal processing methods discussed in the subsequent chapters will be based on detection rates, hence TWIPS2 will not implemented for discussion.

Chapter 3

Simulation

3.1 Simulation formulation

The geometry of the problem is shown in Figure 3.1. A sound source is located at a predefined distance away from a linear target located at the centre of a spherical bubble cloud with a radius of 1 metre. The sound source is assumed to be an echolocating dolphin or porpoise. The linear target is assumed to be a fish (which is appropriate to the context of an echolocating dolphin) with a target strength of -20 dB. As a rough comparison, an Atlantic cod (*Gadus morhua*) with length 125 mm has a target strength of approximately -25 dB when presented broadside to an acoustic beam at a frequency of 6 kHz [14].

While the returns from a fish are primarily from its swim bladder (which is gas filled), one might question the similarity in the acoustic response between a bubble and the swim bladder of a fish, and whether they exhibit the same type of

response under the same conditions. The relationship between bubble radius and resonance frequency was discussed in the previous chapter in section 2.2.1. If one was to compare the radius between a microbubble with that of a fish swim bladder which is in the order of centimetres, their resonance frequencies are separated by several orders of magnitude. Thus, at the frequencies of interest discussed in this research, a fish can be safely assumed to be a linear target.

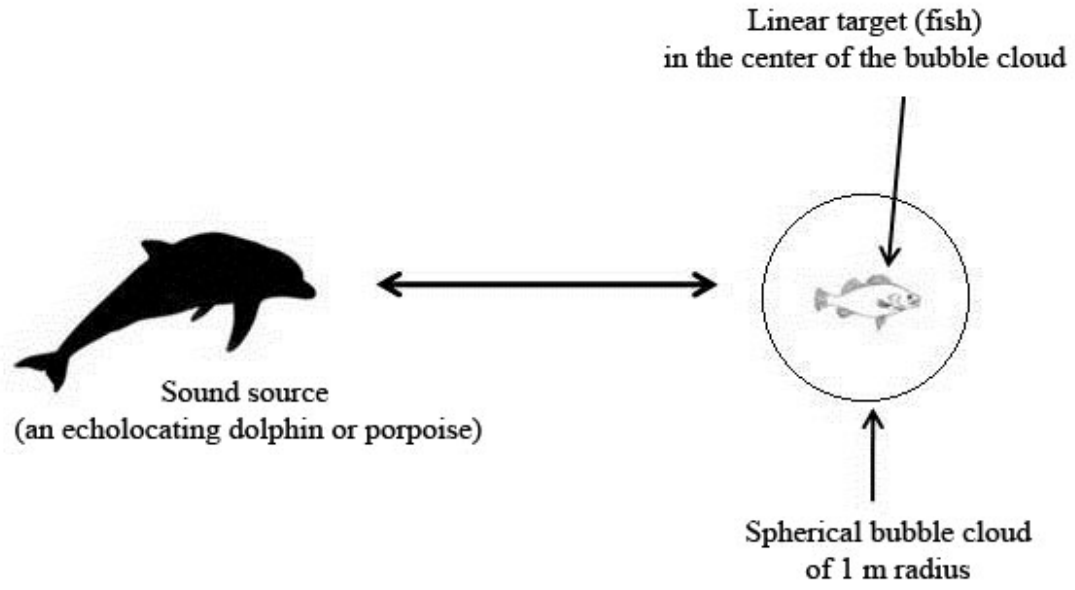

FIGURE 3.1: Geometry of the model used in the simulations.

The bubble population distribution used here is modelled after the work by Meers *et al.* (2001) [32] in which he described the population distribution beneath a breaking wave as a function of bubble radius:

$$n_b = 6 \times 10^6 e^{-0.002(R_0)} \tag{3.1}$$

where n_b is the number of bubbles in 1 cubic metres of water per micrometre increment and R_0 is the bubble radius, expressed in microns.

A comparison of this distribution (denoted by 'Extrapolation 2') against other experimentally measured distributions is given in Figure 7 of [32]. The distribution proposed by Meers *et al.* appears to be overestimated compared to the rest of the distributions described by other investigators. However, one possible explanation could be because Meers's measurements were based at the surf zone whereas the other measurements were taken at deeper waters, hence the differences.

In formulating the model, it was not computationally feasible to consider a continuous range of bubble size. As such, the bubble population was discretised into size bins calculated using Eq. 3.1.

Bubble positions from the center of the cloud were generated by first creating 3 sets of random uniformly distributed variables in the range of ± 1 (metre), with each set representing a component of the Cartesian coordinate (x,y,z) and the centre of the cloud defined by (0,0,0). These sets of coordinates were then converted to the spherical coordinate system to obtain (r, ϕ, θ). Cartesian coordinate combinations that had the corresponding radius (r) value exceeding the bubble cloud radius limit were discarded. The process was repeated until the desired population of sizes was obtained.

The backscatter pressure amplitude response from a single bubble was obtained by solving for the bubble radius and velocity using Eq. A.21 and substituting the results into Eq. A.26. The result was then compensated for the propagation delay and spreading loss measured by the receiver.

Calculating the total back-scatter pressure response from a bubble cluster is no

trivial task especially if multiple scattering between bubbles is considered. However the computational process can be simplified by assuming a low bubble void fraction. This allows bubble responses to be uncoupled. The bubble population distribution described earlier gives a relatively low void fraction which fulfils this criterion. The return signal from the whole bubble cloud can be formed as a summation of convolutions, with one convolution representing the return from the bubbles in the cloud within a size bin, where the delay is proportional to each bubble position in the cloud with respect to the driving sound source, and the weight proportional to spreading loss. While the bubble responses can be nonlinear, superposition still holds for the scattered signals. This significantly helps to reduce the computational load.

In the simulation, a linear target with a predefined target strength was located at the centre of the bubble cloud. The total scatter from the bubble cloud and linear target was obtained from linear superposition by simply adding the two responses together.

3.2 Scaling of equations in dimensionless variables

A MATLAB simulation for calculating the pressure response from a single bubble and a spherical bubble cloud, when excited by a driving signal, was developed based on the modified nonlinear Herring-Keller equation derived in Appendix A. The equations however had to be re-scaled to dimensionless variables in order to

reduce the number of simulation parameters and also to give more control over the precision of results.

The following dimensionless variables were introduced in formulating the equations for implementing on MATLAB:

Radial strain,

$$x = \frac{a - a_e}{a_e} \tag{3.2}$$

Characteristic frequency,

$$w_0 = \sqrt{\frac{p_0}{\rho a_e^2}} \tag{3.3}$$

Dimensionless time,

$$\tau = \omega_0 t \tag{3.4}$$

Time differentiation,

$$x' = \frac{dx}{d\tau} = \frac{1}{\omega_0}\frac{dx}{dt} = \frac{\dot{x}}{\omega_0} \tag{3.5}$$

Normalised pressure,

$$q = \frac{p}{p_0} \tag{3.6}$$

Normalised speed of sound,

$$\gamma = \frac{c}{a_e \omega_0} \tag{3.7}$$

Normalised shear viscosity of liquid,

$$v_L = \eta_L \frac{\omega_0}{p_0} \tag{3.8}$$

Normalised surface tension,

$$S = \frac{\sigma}{p_0} \tag{3.9}$$

The pressure at the bubble surface p_L is reformulated by expressing it in terms of the new dimensionless variables:

$$q_L = \left(1 + \frac{2S}{a_e}\right)(x+1)^{-3\kappa} - \frac{2Sp_0}{a_e(x+1)} - 4v_L \frac{x'}{x+1} \tag{3.10}$$

The derivatives of q_L are:

$$q_1(x,x') = \frac{\partial q_L}{\partial x} = -3\kappa(x+1)^{-3\kappa-1}\left(1 + \frac{2S}{a_e}\right) + \frac{2S}{a_e(x+1)^2} - 4v_L \frac{x'}{(x+1)^2} \tag{3.11}$$

$$q_2(x,x') = \frac{\partial q_L}{\partial x'} = -4v_L \frac{1}{x+1} \tag{3.12}$$

The modified nonlinear Herring-Keller equation expressed in dimensionless variables is obtained as:

$$x''(1+x)(1-M) + \frac{3}{2}x'^2\left(1 - \frac{M}{3}\right) - (1+M)(q_L - 1 - q_i) - \frac{1}{\gamma}(1+x)q_L' = 0 \tag{3.13}$$

$$x'' = -\frac{1}{q_3}\left[\frac{3}{2}x'^2\left(1 - \frac{M}{3}\right) - (1+M)(q_L - 1 - q_i) - \frac{1}{\gamma}(1+x)q_1 x'\right] = 0 \tag{3.14}$$

where

$$q_3 = (1+x)(1-M) - \frac{1}{\gamma}(1+x)q_2 \tag{3.15}$$

$$M = \frac{x'}{\gamma} \tag{3.16}$$

Eq. 3.14 is a second order ordinary differential equation which can be solved numerically with a explicit Runge-Kutta (4,5) formula, the Dormand-Prince pair. This formula is available as a standard function (*ODE45*) in MATLAB.

3.3 Signal processing

In the numerous literature studies on target contrast enhancement by Leighton *et al.*, they compared the performance between standard sonar processing and TWIPS for detecting a linear target in the centre of a bubble cloud. Other standard signal processing techniques have also been introduced in the simulations here to give a thorough comparison involving more techniques. These techniques include: averaging and smoothing, bandpass filtering and standard cross correlation. In addition, a new variant of TWIPS will be introduced and its performance will be evaluated. To avoid confusion, the TWIPS1 method adopted by Leighton *et al.* will thereafter be referred to as TWIPS1a, whereas the new variant of TWIPS will be referred to as TWIPS1b. A more complete description of each of these methods is as follows:

1. Standard sonar processing

   Leighton *et al.* have described what they call 'standard sonar processing' as

the result obtained by averaging and normalising the returns from a spatially evolving bubble cloud (in which the bubbles positions in the cloud have changed) when ensonified by two positive (identical) driving pulses, and cross-correlating this averaged and normalised output with the envelope of the input signal. The reason for using an averaged pair of pulses for standard sonar processing is because TWIPS1 has the advantage of using return echoes from a single pair of pulses. Hence it seems fair for standard sonar processing to average the return from two pulses.

2. TWIPS1a

   TWIPS1a has been previously described in detail in Section 2.3 of this thesis. In summary, TWIPS1a is performed by first finding the difference between the normalised backscatter responses from a pair of inverted pulses ensonifying a bubble cloud. The normalised difference between the two backscatter responses is then filtered by a narrowband bandpass filter with a centre frequency similar to the driving pulse. In real life situations, the bubble cloud has to be spatially evolving. However in TWIPS1a, pairs of inverted pulses are assumed to be transmitted with a very short delay, such that the positions of bubbles in the cloud have not changed. The bubble cloud is however allowed to evolve between pairs of inverted pulses.

3. Averaging and smoothing

   The averaging and smoothing method was introduced to observe the direct effects of constructive and/or non-constructive addition by backscatters from

a spatially evolving bubble cloud. This method is identical to standard sonar processing except that the cross-correlation operation is omitted.

4. Bandpass filtering

   The bandpass filtering method was introduced for comparison with the other methods for its simplicity. In addition, the bandpass filtering method serves as a good comparison with TWIPS1a since TWIPS1a consist of a bandpass filter stage. This way, one can compare and observe the effects with and without the effects of linear enhancement and nonlinear suppression from the subtraction operator in TWIPS1a. Bandpass filtering is identical to standard sonar processing except that the cross-correlation operator has been replaced with a bandpass filter (similar to the one used in TWIPS1a).

5. Standard cross correlation

   Leighton *et al.* in their description of standard sonar processing, used the envelope of the driving pulse for cross-correlation. An alternative to this would be to perform coherent processing, whereby cross-correlation is performed with the original driving pulse. This method theoretically gives a much higher processing gain and should therefore be included for comparison. The standard cross correlation is introduced here and defined as a method similar to Leighton's definition of standard sonar processing except that the cross-correlation operator is performed with the original driving pulse.

6. TWIPS1b

   One might have noticed that all the signal processing methods mentioned

above, except for TWIPS1a, use the backscatter from two pulses whereby bubble positions in the cloud have changed. It would be interesting to observe any effects on detection performance if the bubble cloud is allowed to evolve spatially between a positive and negative driving pulse. The TWIPS1b method is introduced here and defined to be similar to TWIPS1a except that the bubble positions in the bubble cloud are allowed to change during the time between a positive and negative driving pulse.

3.4 Verification of model by comparing with examples by Leighton *et al.* (2006)

In [14], the authors described the performance of TWIPS1a compared to conventional (standard) sonar processing with two specific simulation examples. The simulations were carried out using windowed pulses with centre frequencies of 6 and 300 kHz. The former example was reproduced and will be discussed in this section.

Assumptions following those given in [14] were made in all the simulations presented in this work unless otherwise specified:

1. Bubble responses are uncoupled;
2. All bubbles in the entire cloud are driven by the same input sound pressure;
3. All bubbles in the cloud do not move during the time between each twin pair of pulses;

4. The time between twin pulses allows bubbles to move;

5. The target does not displace any bubble. It has no acoustic shadow and does not diffract any acoustic energy;

The bubble population distribution model described in [14] gives a low void fraction which helps to support the first assumption. In real life situations, such distributions exist in the form of γ-plumes which can have a void fraction in the range between 10^{-7} to 10^{-6} and persist for durations between 100 to 1000 s [15]. Assumption 2 might have been poorly made because one cannot neglect the effects of attenuation as the acoustic plane wave passes through the bubble cloud. The attenuation of a plane wave through a γ-plume was modelled by Novarini *et al.* (1998) and a figure showing the attenuation coefficient against transmission frequency is given in Figure 2.5 of [41]. Consider a 6 kHz plane wave passing through a spherical γ-plume 2 m in diameter, with a target in the centre of the plume. From Figure 2.5, the attenuation is approximately 0.04 dB/cm at 6 kHz; therefore the driving pulse would be attenuated by 4 dB when it strikes the target located at a depth of 1 m inside the bubble cloud. Similarly, for a 125 kHz plane wave, the attenuation is approximately 0.22 dB/cm, which is equivalent to 22 dB at 1 m range. The attenuation is noticeably significant at this frequency. However, this observation should only serve as a rough guide because there are many other factors that can affect the attenuation of an acoustic plane wave through any given bubble cloud.

Owing to the complexity of the problem, assumptions 1 and 2 were made to greatly simplify computation of the problem. A single simulation trial in which

we compute/calculate the responses of groups of neighboring bubbles with similar sizes and then sum their results, takes more than 10 hours to complete with this simplification. If the effects of bubble coupling and attenuation in the bubble cloud were taken into consideration, one would need to compute the response for each and every bubble in the cloud. This would clearly increase the computational time by several orders of magnitude. It should be emphasised that the assumptions were used in the simulations here for an unbiased comparison of results with those shown in [14]. Despite some of these poor assumptions, the authors of [14] did obtain similar results in their simulations and experiments.

The bubble cloud population distribution used in the simulations here follow the one used in [14] where the entire bubble cloud was discretised to consist of bubbles within 5 logarithmically spaced size bins with centre radii 10, 50, 100, 500, 1000 and 5000 μm. The authors stated that the void fraction they found from these centre radii and limits using Eq. 3.1 gave a value in the order of 10^{-6}. The bubble population distribution they used is given in page 35, Table 1 of [14] and reproduced in Table 3.1 in this report.

TABLE 3.1: Bubble population distribution described by Leighton *et al.* (2006)

Bubble radius (μm)	Size bin radius limits (μm)	Number of bubbles in size bin per cubic meter of seawater
10	$10^{0.75} \leq R_0 < 10^{1.25}$	3.500×10^7
50	$10^{1.25} \leq R_0 < 10^{1.75}$	3.300×10^6
100	$10^{1.75} \leq R_0 < 10^{2.25}$	3.000×10^4
500	$10^{2.25} \leq R_0 < 10^{2.75}$	3.100×10^2
1000	$10^{2.75} \leq R_0 < 10^{3.25}$	3.000×10^0
5000	$10^{3.25} \leq R_0 < 10^{3.75}$	0.000

Quoting from the first paragraph of Section VII in [4],

> *The bubble cloud is assumed to be a sphere of radius 1 m, containing around 35 million bubbles following the population size distribution as measured by Meers* et al. *[16] such that the void fractions (the ratio of the volume of gas within a cloud to the total volume occupied by the cloud) on the order of* 10^{-7} *(i.e* $10^{-5}\%$*).*"

Using the bubble population distribution described in Table 3.1, the total number of bubbles in a spherical bubble cloud of 1 m radius is calculated to be 1.606×10^8 and the void fraction evaluated to 2.175×10^{-6}. It appears that the void fraction value calculated here contradicts with what was stated in [4].

Verification of the third column in Table 3.1 using Eq. 3.1 revealed that the number of bubbles in each size bin was much greater than those reported by Leighton *et al.*. The actual values evaluated using Eq. 3.1 are presented in Table 3.2.

TABLE 3.2: Bubble population distribution calculated using Equation 3.1

Bubble radius (μm)	Size bin radius limits (μm)	Number of bubbles in size bin per cubic metre of seawater
10	$10^{0.75} \leq R_0 < 10^{1.25}$	5.734×10^7
50	$10^{1.25} \leq R_0 < 10^{1.75}$	1.144×10^8
100	$10^{1.75} \leq R_0 < 10^{2.25}$	8.829×10^7
500	$10^{2.25} \leq R_0 < 10^{2.75}$	8.613×10^6
1000	$10^{2.75} \leq R_0 < 10^{3.25}$	3.887×10^3
5000	$10^{3.25} \leq R_0 < 10^{3.75}$	0.000

The calculated bubble population size in a spherical cloud of 1 m radius was found to consist of approximately 1.100×10^9 bubbles occupying a gas volume of 0.004 m^3. The void fraction in the bubble cloud evaluated to be approximately 9.400×10^{-4}, which was about 2 to 3 orders of magnitude greater than what Leighton *et al.* claimed in [3] and [14]. This large void fraction would have violated the first assumption of uncoupling between bubbles. Through correspondence with one of the authors of the paper, it seems like it is most likely that they made a mistake in some of their statements.

Nevertheless, the main objective in this research is to compare the target detection performance of TWIPS1a with other methods. As such, for an unbiased comparison at this stage, the simulations presented for this purpose (in this section) were performed using the bubble population presented in Table 3.1. It is reasonable to use the values in this table since they fall within acceptable limits in terms of the void fraction and population size of the γ-plumes discussed earlier. The new bubble population distribution found in Table 3.2 does not seem physically realistic given the natural occurrences of γ-plumes.

The driving pulse used in the simulation was a 6 kHz sine wave pulse consisting

of 6 cycles with an applied Hanning window. The zero to peak pressure of the driving pulse was 60 kPa (referenced at 1 metre away from the bubble cloud) and a sampling resolution of 2×10^6 samples/second was used.

In [14], there was no quantitative measure of the performance between the TWIPS1a and standard sonar processing. The assessment of performance was purely visual and based on time-amplitude (waterfall) plots comparing the output of the two different signal processing methods (i.e., standard sonar processing and TWIPS1a) for target present and absent conditions.

To further substantiate/investigate the results and claims in [14], a measure of signal to noise ratio (SNR) and receiver operating characteristics (ROC) curves will be introduced in this project to provide a better evaluation in comparing the performance among the different signal processing methods. A brief introduction to ROC curves is provided in Appendix B.

The results presented in the next two sub-sections were obtained from a simulation program written using MATLAB R2009. The simulation was performed using a desktop computer (Dell Optiplex 780, 3.16 GHz. Intel Core 2 Duo processor, 8 GB 1066 MHz DDR3 SDRAM). All simulation parameters were kept identical to those provided in Leighton *et al.* (2006) [14] and any modifications to the simulation parameters will be highlighted.

3.4.1 Single bubble response

The simulated backscatter waveform from a bubble in the different radius size bins (provided in Table 3.1) in response to a positive and negative driving pulse of 6 kHz is given in Figure 3.2. A comparison of this result obtained in the simulation here with the result shown in Figure 9 of [14] shows that individual bubble backscatter in the corresponding radius size bin matches reasonably well in magnitude and their state of motion (linear or nonlinear). It can be observed that bubbles with radii 500 μm and below scatter nonlinearly, with the 500 μm bubble having the greatest backscatter pressure amplitude among all the size bins since it corresponds most closely to the resonance bubble radius for a 6 kHz signal. It can also be observed that the backscatter from bubbles with radii 10, 50, 100 and 500 μm, when ensonified with the negative pulse, is not an inverted version of the backscatter from the positive pulse. This is due to the nonlinear pulsation of the bubbles. It is interesting to note that for the 500 μm bubble, both the positive and negative response exhibit non-symmetrical amplitude peaks which are dominant in the positive cycle. In addition, they appear to be shifted copies of each other rather than being inverted copies of each other as observed in the linear case.

Frequency response plots (Figure 3.3) of the scattered pressure from a bubble in the respective radius size bin reveals further information on harmonic dispersion. These harmonic dispersions occur at frequency multiples of the driving pulse frequency, and can be seen clearly in the response from the 10, 50 and 500 μm bubbles. Harmonic dispersion from the 100 μm bubble is less prominent and a

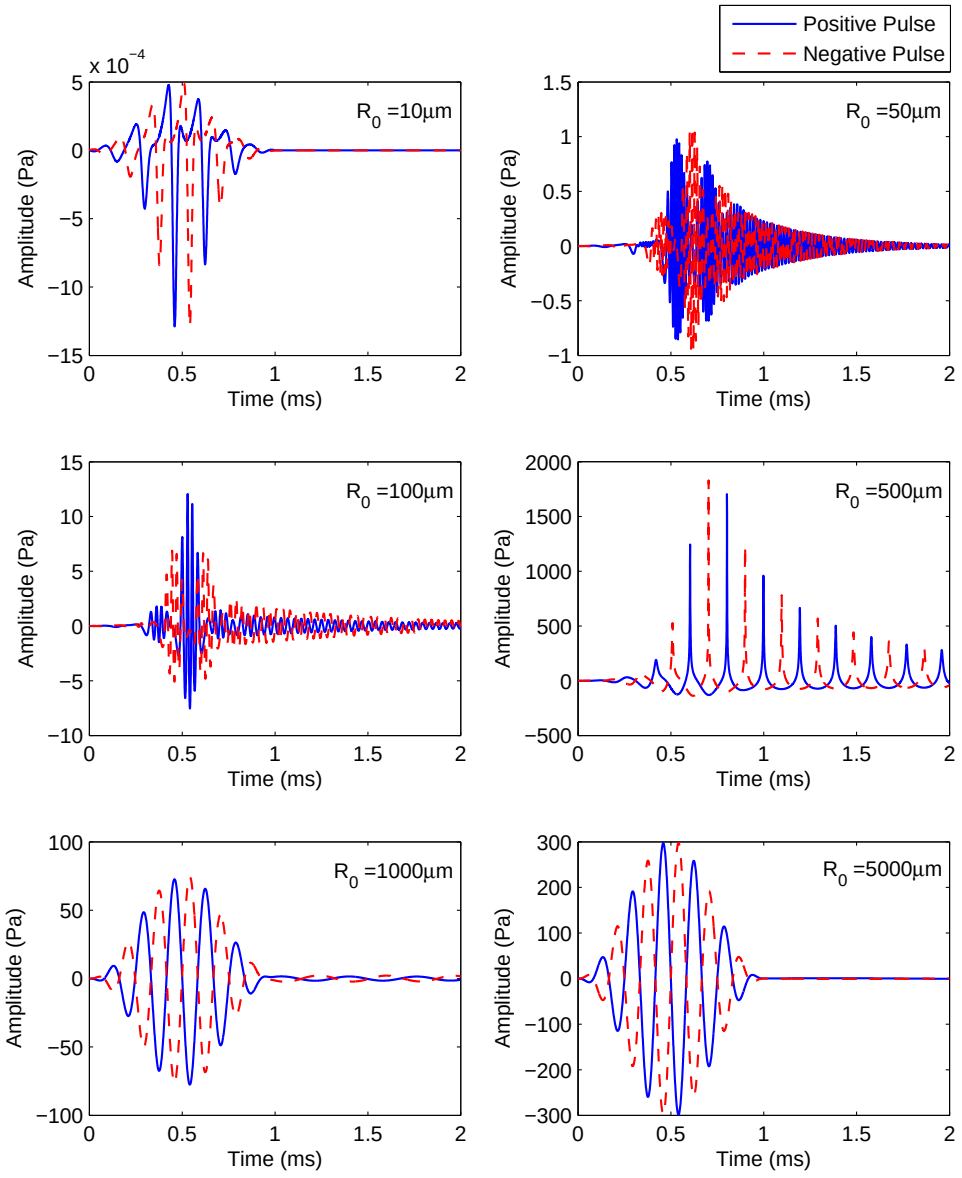

FIGURE 3.2: Waveforms illustrating the backscatter from bubbles with radii 10, 50, 100, 500, 1000 and 5000 μm, when driven by a positive and negative 6 kHz, 60 kPa windowed pulse.

Note: The scaling on the y-axis are different for each plot here and in subsequent figures in this report. This is to better illustrate the backscatter waveform shape.

sharp peak is observed at 28 kHz. The resonance bubble size of 500 μm scatters the most energy. Harmonic dispersion can be observed for this bubble size but there is a slight shift in the scattering frequencies. The harmonics occur at multiples of 5.4 kHz even though the driving frequency is at 6 kHz.

The frequency response of bubble backscatter due to a negative driving pulse exhibit the same resonance peaks as that observed from the frequency response due to the positive driving pulse. There are however slight differences in the higher frequency harmonics for nonlinear responses in the 10, 50, 100 and 500 μm bubbles.

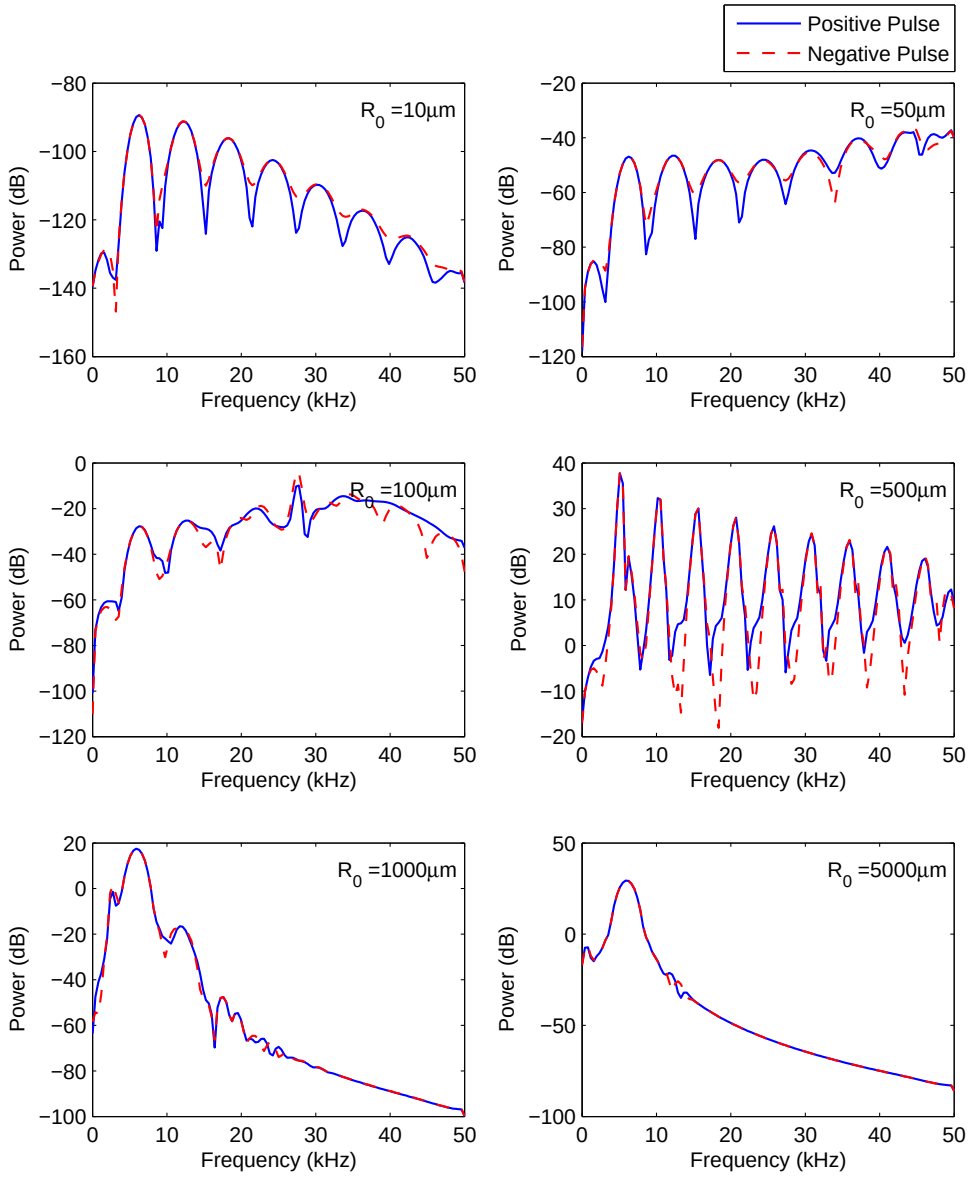

FIGURE 3.3: Frequency response plots illustrating the backscatter from bubbles with radii 10, 50, 100, 500, 1000 and 5000 μm, when driven by a positive and negative 6 kHz, 60 kPa windowed pulse.

By applying standard pulse inversion technique, the frequency responses from bubbles driven by a 6 kHz windowed pulse illustrate the enhancement and suppression of harmonics in the nonlinear case. In Figure 3.4, the harmonic peaks occur at odd and even multiples of the transmit frequency (e.g. 6 kHz, 12 kHz, 18 kHz, 30 kHz ...). When inverted pulses are summed, the fundamental component and odd harmonics are suppressed while the even harmonics are enhanced. On the other hand, the difference of inverted pulses enhances the fundamental component and even harmonics while odd harmonics are suppressed.

The results shown so far all agree with what has been discussed in [14]. Simulated bubble responses look similar to those given in the examples in the quoted reference. In addition, the enhancement and suppression of harmonics using pulse inversion is successful demonstrated. The next section will discuss the response from a bubble cloud.

3.4.2 Bubble cloud response

The simulation of a bubble cloud response was performed following the model described in Figure 3.1. The transmitting source and receiver was located 10 m from the bubble cloud and the linear target present in the middle of the bubble cloud had a target strength of -20 dB.

In [14] the bubble cloud response was presented in the form of two- dimensional waterfall plots. These waterfall plots were obtained by plotting the processed

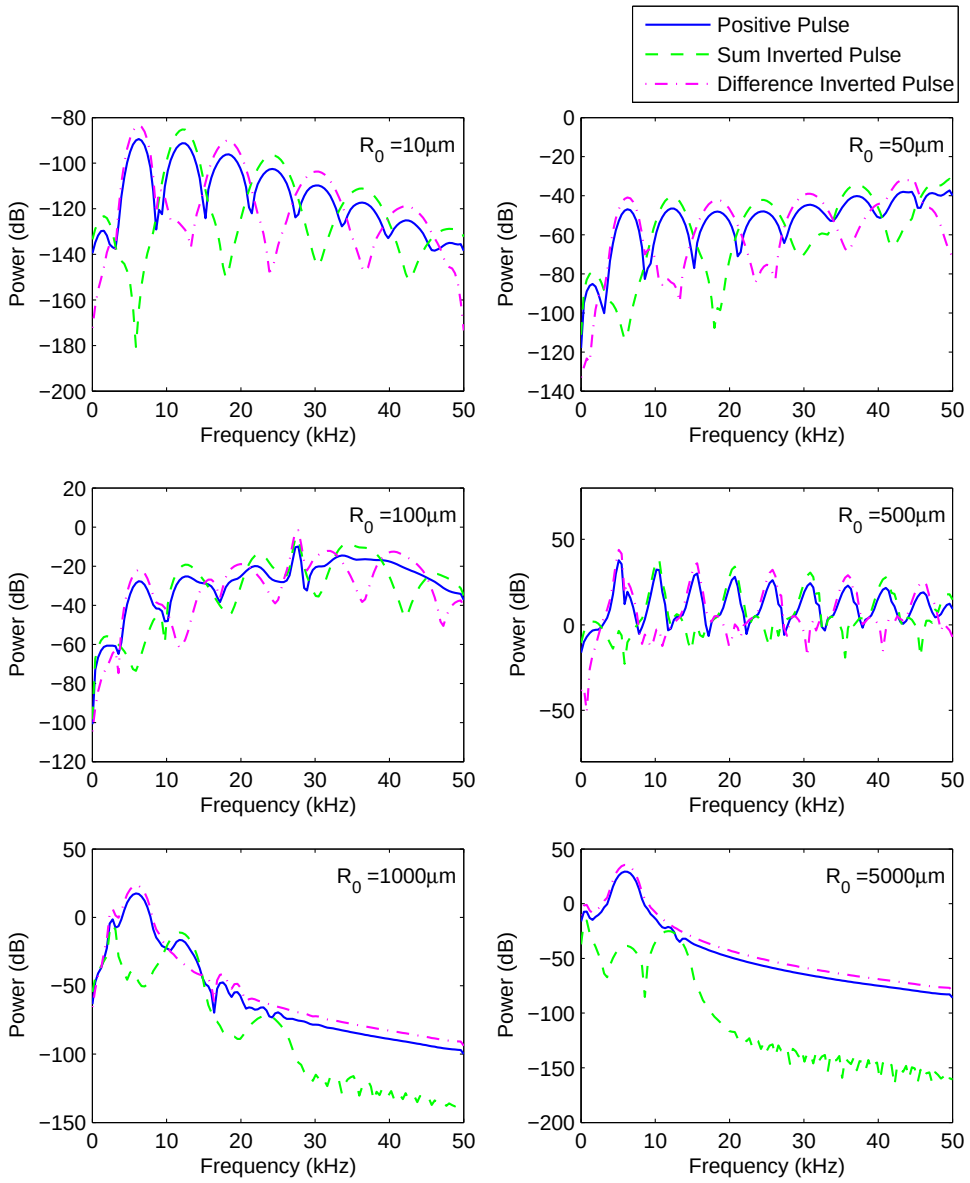

FIGURE 3.4: Frequency response plots illustrating the summation/subtraction of backscatter from bubbles with radii 10, 50, 100, 500, 1000 and 5000 μm, when driven by a positive and negative 6 kHz, 60 kPa windowed pulse.

backscatter output from each driving pulse (ping) as a time history on a one-dimensional line, with a colour map corresponding to the amplitude of the envelope of the signal at a particular instance of time. The envelope was obtained by using the Hilbert transform. A low pass filter was applied to further smooth the envelope before plotting. Fifty such pings were stacked one on top of another to form the waterfall plot. The x-axis shows the time delay and the y-axis the ping number. The colour map is the normalised amplitude of the envelope of the backscatter signal. Figure 3.5 shows an example of the envelope of bubble cloud backscatter when a target is absent or present, and Figure 3.6 shows the corresponding waterfall plots. The waterfall plot basically serves as a visual aid in representing the energy difference between target absent and present conditions.

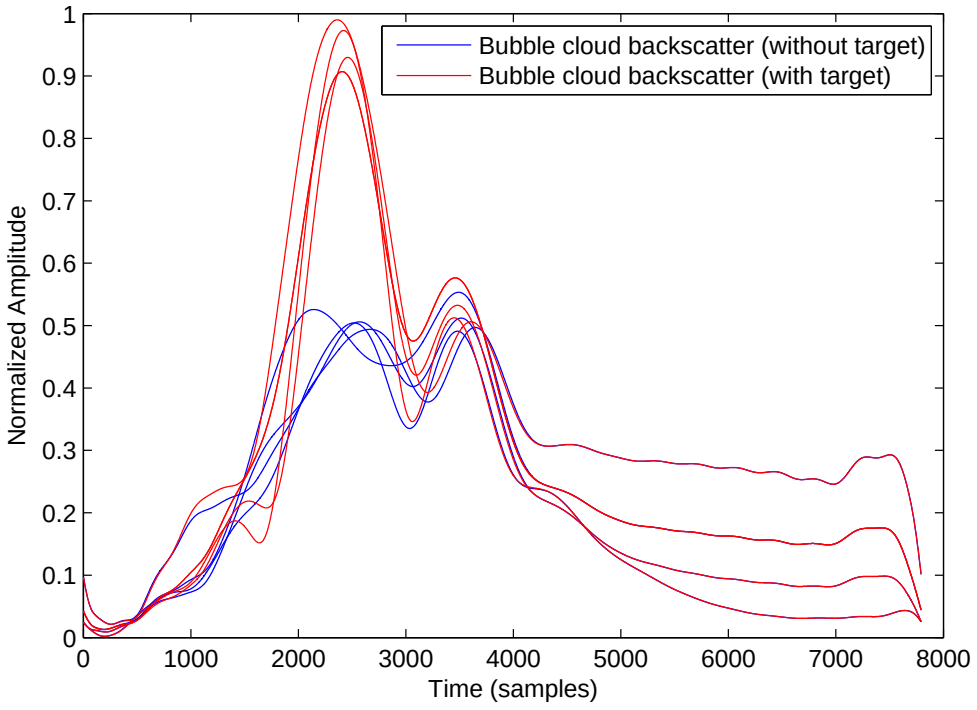

FIGURE 3.5: An example plot showing the envelope of bubble cloud backscatter when a target is absent/present.

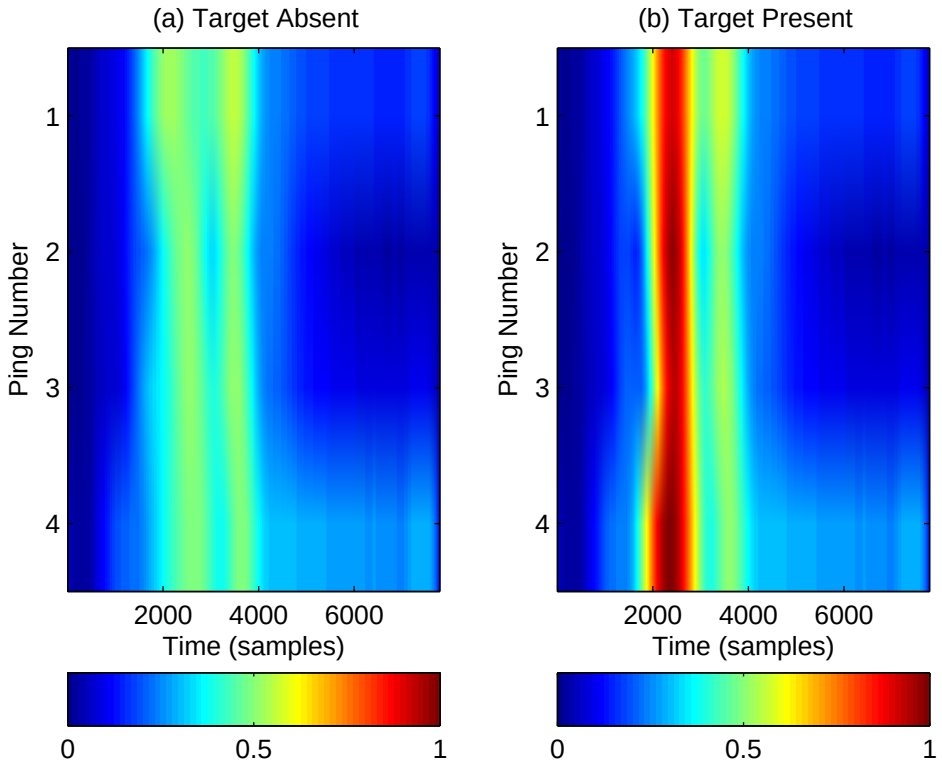

FIGURE 3.6: Corresponding waterfall plot of the example in Figure 3.5 when a target is (a) absent; (b)present.

The backscatter from a bubble cloud consisting of a bubble distribution given in Table 3.1 was processed using standard sonar processing and TWIPS1a, and their waterfall plots compared.

Comparing the results shown in Figure 3.7 here with the findings shown in Figure 12 of [14], it does seem that standard sonar processing does not perform well in detecting the target as described in the model. The waterfall plot between the target present and target absent case appears almost similar, except for a few small highlights of high amplitude scattering in the target present case which does not amount to any significant conclusion.

The narrowband bandpass filter used in the simulation for TWIPS1a is a

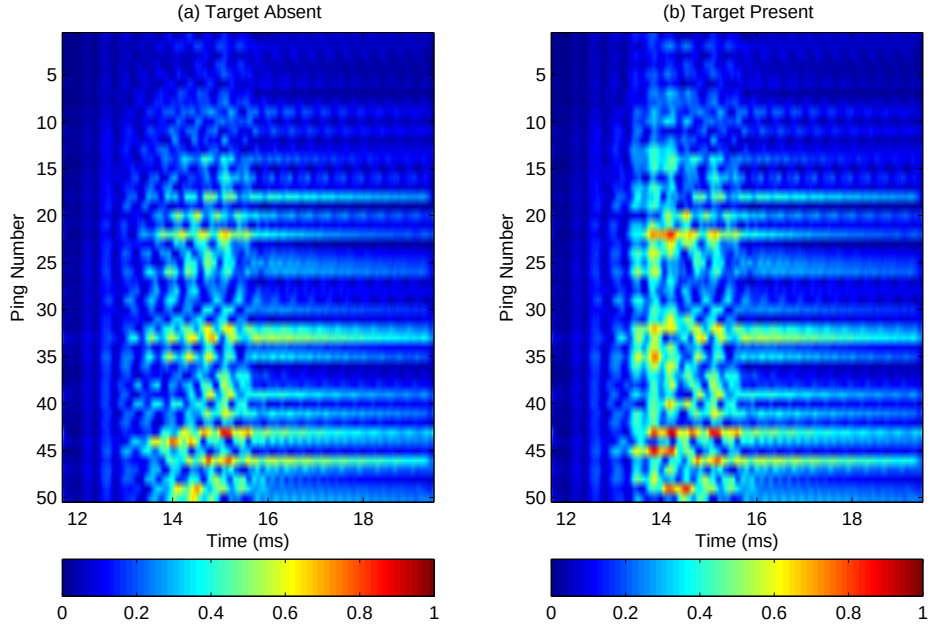

FIGURE 3.7: Waterfall plot of bubble cloud backscatter from a 6 kHz, 60 kPa pulse using standard sonar processing when a target is (a) absent; (b) present (TS = -20 dB).

Note: The colour scale is the normalised backscatter amplitude from the bubble cloud. The value of 1 represents the maximum amplitude.

digital finite impulse response (FIR) equiripple filter. The filter has a passband gain of 1 dB from 4 to 8 kHz and a stopband gain of -80 dB at the 2 and 10 kHz cutoff frequencies. The frequency response of the filter is shown in Figure 3.8.

The waterfall plot for TWIPS1a is given in Figure 3.9 where it shows better contrast between the target 'absent' and 'present' cases. This result somewhat coincides with the results given in Figure 13 of [14], which suggested a clear indication of high amplitude scattering at the position occupied by the linear target compare to elsewhere in the bubble cloud.

Based on the waterfall plots from these two different signal processing methods, Leighton and co-workers reported that their simulations of TWIPS1a outperformed standard sonar processing. There is however a problem with standard

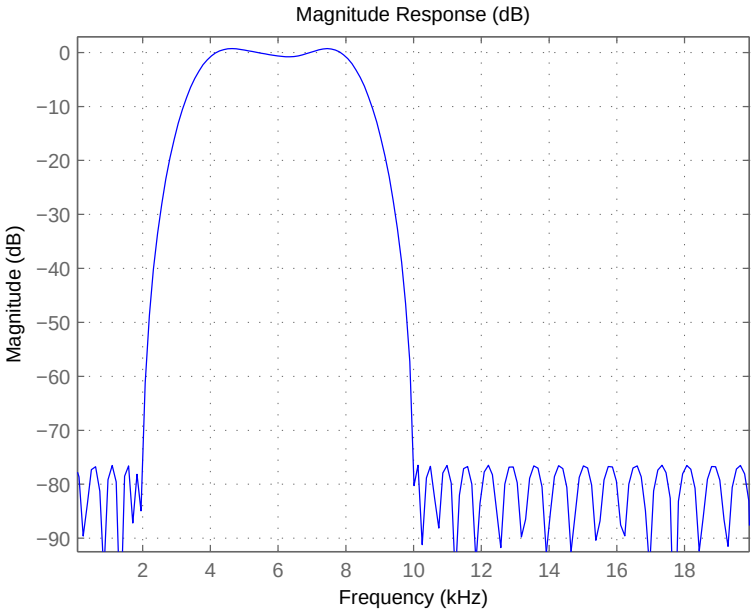

FIGURE 3.8: magnitude response of a 6 kHz bandpass filter used in the simulations.

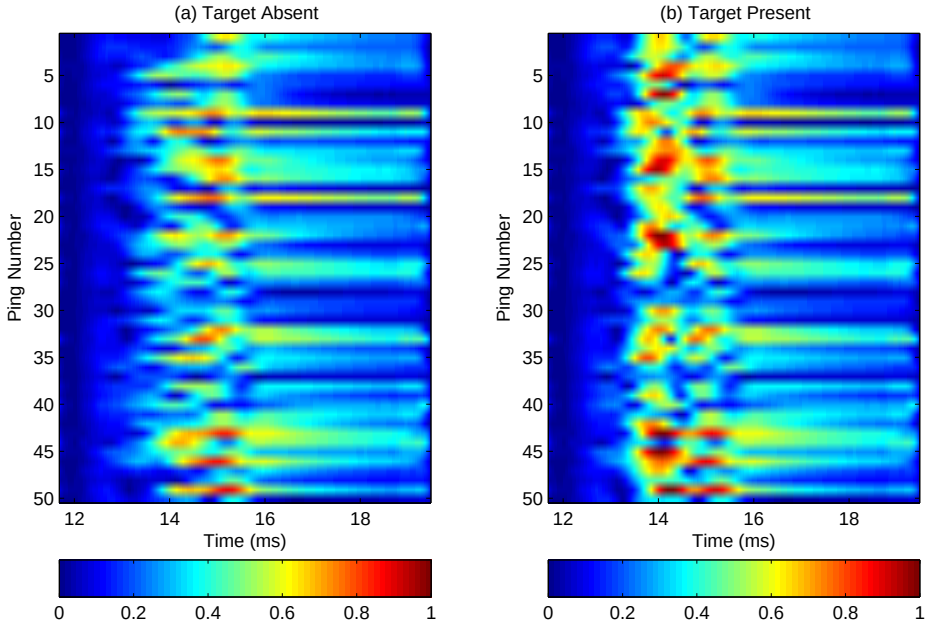

FIGURE 3.9: Waterfall plot of bubble cloud backscatter from a 6 kHz, 60 kPa pulse using TWIPS1a when a target is (a) absent; (b) present (TS = -20 dB).

sonar processing that might have been overlooked for the 6 kHz driving pulse example. If one was to compare the pulse width of the envelope of the driving pulse with the width of the bubble cloud, it appears that the pulse width of the driving pulse spans almost the entire diameter of the bubble cloud. As a result, this might have affected the cross correlation performance when the target was present in the middle of the bubble cloud. More significantly, when a simple averaging and smoothing method was performed on two backscatter responses, its waterfall plot showed some improvement compared to the standard sonar processing method.

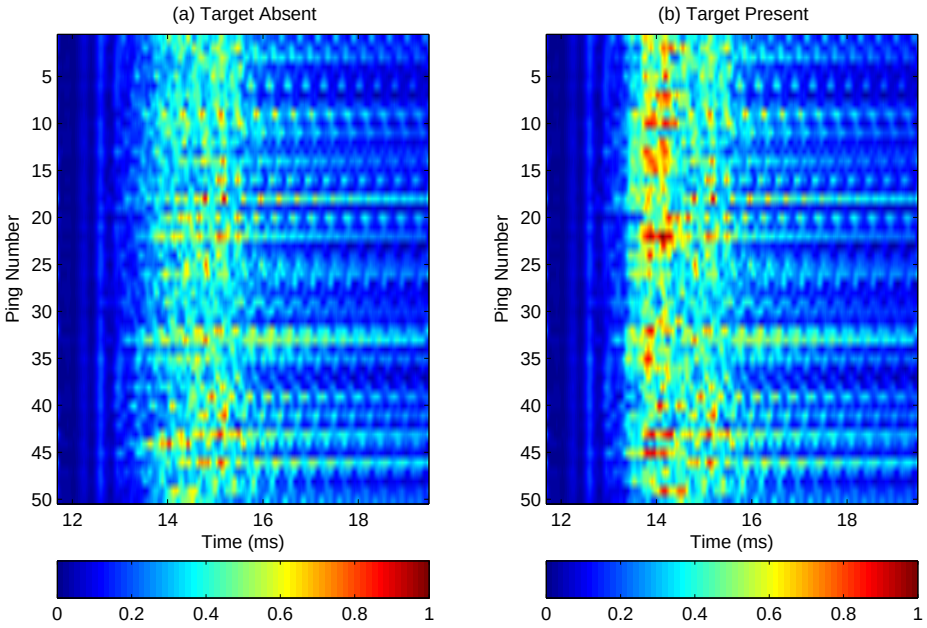

FIGURE 3.10: Waterfall plot of bubble cloud backscatter from a 6 kHz, 60 kPa pulse using averaging and smoothing when a target is (a) absent; (b) present (TS = -20 dB).

Comparing the waterfall plots in Figures 3.7 and 3.10, it does seem that the performance of standard sonar processing method is inferior even against the very simple averaging and smoothing method. As such, the standard sonar processing method would not have served as a good comparison against TWIPS1a in the 6 kHz

driving pulse example. The results from bandpass filtering and cross correlation methods will be presented in Figures 3.11 and 3.12 respectively. It can be observed that both methods show relatively good contrast between the target absent and present case.

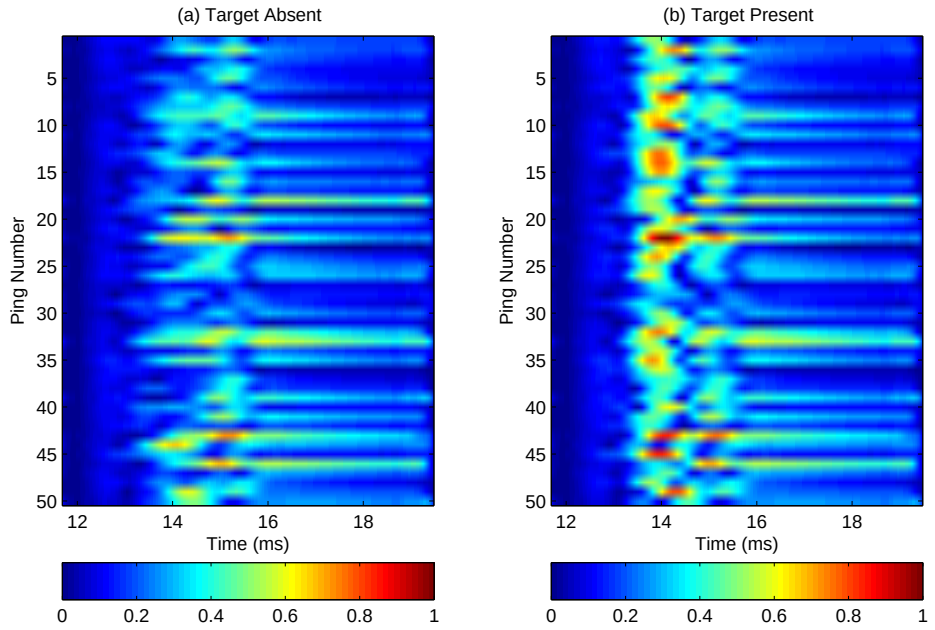

FIGURE 3.11: Waterfall plot of bubble cloud backscatter from a 6 kHz, 60 kPa pulse using bandpass filtering when a a target is (a) absent; (b) present (TS = -20 dB).

The waterfall plots produce features for the human brain to differentiate between target present or absent conditions. These features may be in the form of colours, positions of high intensity areas, and/or texture. However, it is visually not easy to quantify and compare each of the processing methods shown. The easiest method would perhaps be to compare the signal to noise ratio (SNR) between the energy scattered from the target alone (signal) and the energy scattered from the bubble cloud alone (noise). In our work, the signal energy was found by subtracting the energy of the envelope of the bubble cloud backscatter (with target

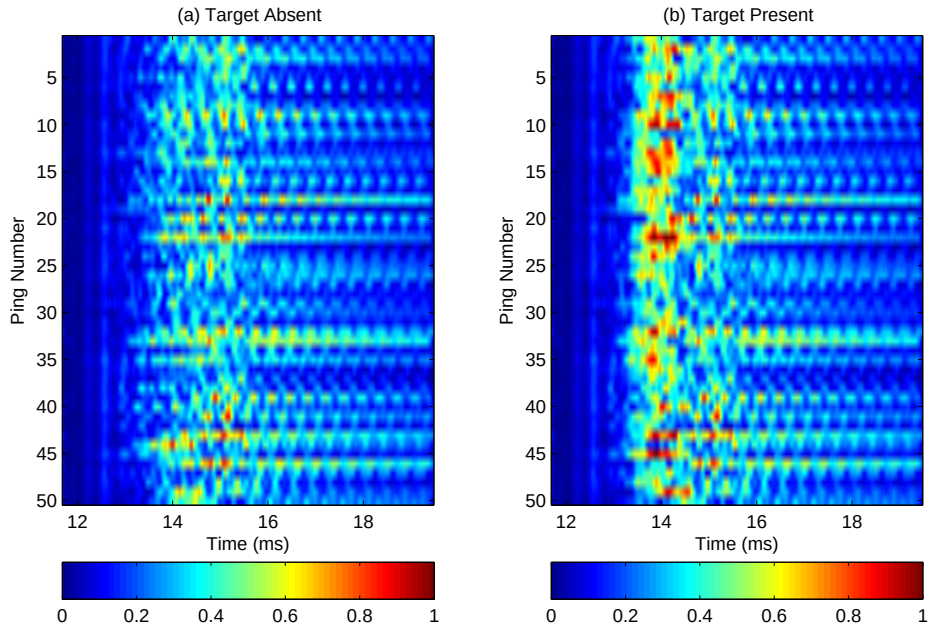

FIGURE 3.12: Waterfall plot of bubble cloud backscatter from a 6 kHz, 60 kPa pulse using cross correlation when a target is (a) absent; (b) present (TS = -20 dB).

present) from the energy of the envelope of the bubble cloud backscatter alone, whereas the noise energy is simply the energy of the envelope of the backscatter from the bubble cloud only. While this method might not provide the best numerical measure of discrimination, it gives a good approximation of the performance of the various signal processing methods when compared to visual analysis of the waterfall plots.

The SNR for the simulation discussed here using different processing methods is averaged over 50 pings and presented in Table 3.3.

Comparing the SNR among the different signal processing methods, bandpass filtering appears to give the best target/bubble contrast. This is followed closely by cross correlation. It is interesting to note that TWIPS1a method gives the worst SNR among all the methods, although the waterfall plot for TWIPS1a gives

Table 3.3: Comparison of SNR for different processing methods - 6 kHz at 60 kPa driving pulse.

Signal processing method	SNR
Averaging and smoothing	0.250
Bandpass filtering	0.396
Cross correlation	0.357
Standard sonar processing	0.252
TWIPS1a	0.222

a better contrast in the area occupied by the target. However, from the waterfall plot for TWIPS1a, there is some evidence of high amplitude scattering from other parts of the cloud, which could have contributed to more noise, thus its low SNR.

The comparison of SNR among the different signal processing methods is not a strict measure of performance since it does not offer statistical measures of detection rates and confidence intervals. As such, receiver operating characteristics (ROC) curves will be introduced to provide a better evaluation in comparing the performance among different signal processing methods. The method of plotting ROC curves is discussed in Appendix B.

For each simulation in this project, 50 sets (n = 50) of 100 bubble cloud backscatter responses were generated to obtain 50 waterfall plots and 50 ROC curves for each of the processing method discussed. Each point on the ROC curve is plotted by varying the detection threshold and finding the percentage of correct detections and false alarms. Correct detection is measured from the waterfall plot (target present) by finding the number of pings in the time samples occupied by the target that have an amplitude higher than the specified detection threshold. A false alarm is measured from the waterfall plot (target absent) by finding the number of pings in the entire time duration that have an amplitude higher than the

detection threshold. The false positive rate (FPR) and true positive rate (TPR) are then calculated using Eq. B.2 and B.1 respectively.

Each of the ROC curves presented in this report was found by averaging over 50 ROC curves. The 95 % confidence interval for a FPR of 0.1 and its corresponding 95 % confidence interval for TPR was plotted. Any overlap in the confidence interval between two or more signal processing techniques would indicate that these methods are not significant from each others.

The ROC curves comparing the different signal processing methods for a false detection rate of 10% (FPR = 0.1) is shown in Figure 3.13. The 95% confidence interval is also shown in the figure.

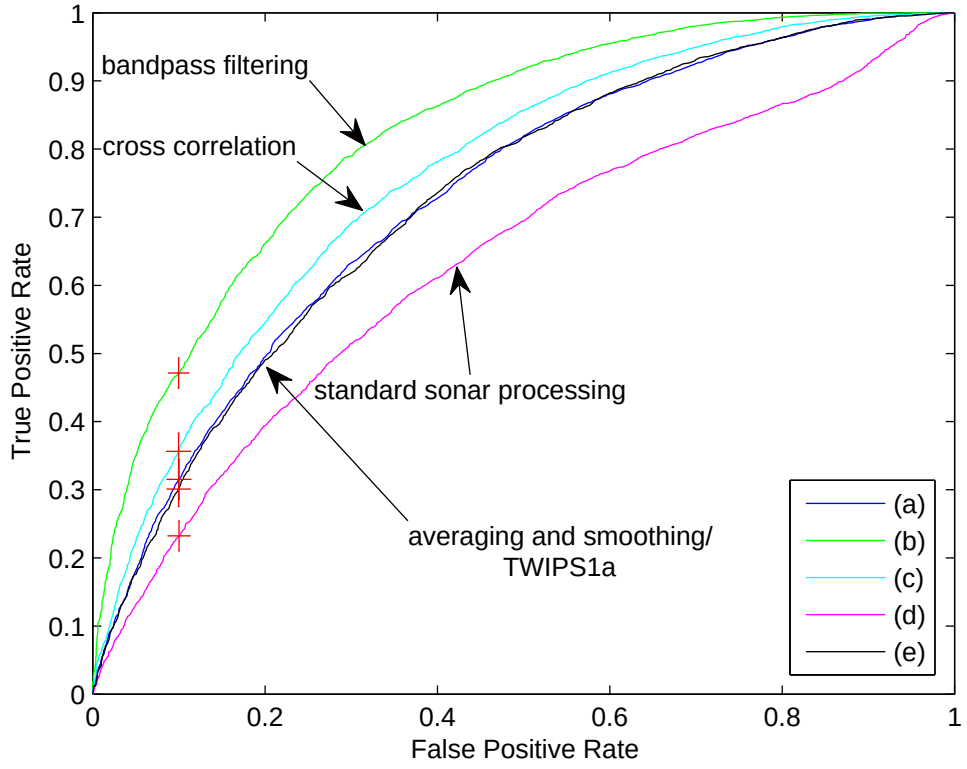

FIGURE 3.13: 6 kHz at 60 kPa pulse - Mean ROC curve with 95% CI (n = 50) at 0.1 FPR for (a) averaging and smoothing; (b) bandpass filtering; (c) cross correlation; (d) standard sonar processing; (e) TWIPS1a.

The results presented in the ROC curves show that bandpass filtering method significantly outperforms the other methods for a FPR of 0.1. On average, the averaging and smoothing method performed slightly better than cross correlation and TWIPS1a, but their confidence interval overlaps, indicating that their performance indicator is not significant. Standard sonar processing performs most poorly among all the different signal processing methods.

To further address the problem of why TWIPS1a has an inferior performance compared to some of the newly proposed methods, one of the assumptions made earlier was re-looked into. It was assumed that bubbles in the cloud did not move between pairs of inverted pulses for TWIPS1a. However, all of the other methods used an average between two (positive) pulses from a non-stationary bubble cloud, which meant that bubbles were in different positions for each pulse. The averaging effect caused by the scattering from bubbles (noise) in different random positions and scattering from a target (signal) in a fixed position effectively increased the SNR. Since the linear target remains stationary, when the backscatter from two positive pulses is added and averaged, its amplitude is the same as the backscatter from one single pulse. However for the backscatter from the bubbles, since they are in random positions for each positive pulse, summing the backscatter from two positive pulses does not give a two-fold increase in amplitude. Averaging the sum effectively reduces the magnitude of the backscatter to a value less than that compared with the backscatter of a single pulse.

The assumption of stationary bubbles between inverted pulses in TWIPS1a provided a disadvantage compared to the other methods. When the returns from

a positive and negative pulse are subtracted, backscatter from the linear target (signal) adds up, while the backscatter from the bubbles (noise) only effectively cancels out the higher order odd harmonics which would have been removed by a bandpass filter at the output stage. Hence it might make some sense to increase the delay between inverted pulses to allow bubbles to move substantially within a bubble cloud. This would not be practical in situations where the linear target is moving rapidly. Nevertheless it would be interesting to observe any improvement in TWIPS1a by assuming a non-stationary bubble population between pairs of inverted pulses, hence the introduction of TWIPS1b in the simulations

The waterfall plot for TWIPS1b is given in Figure 3.14, where it shows some improvement in suppressing scatter from bubbles in the cloud. The new calculated SNR is approximately 0.394 (an improvement from the previous value of 0.252), which makes it comparable in performance to bandpass filtering.

The ROC curves are plotted again to include TWIPS1b. This is shown in Figure 3.15.

The new ROC curve shows the improvement in switching from TWIPS1a to TWIPS1b. It can be observed that the performance of TWIPS1b is on par with bandpass filtering. Noting that TWIPS1b uses the same bandpass filter in the bandpass filtering method at its output stage, this could have explained why it performs equally well as the bandpass filtering method.

The simulation results from a single bubble using the proposed model produced results similar to those observed in the examples in [14]. Moreover, the backscatter

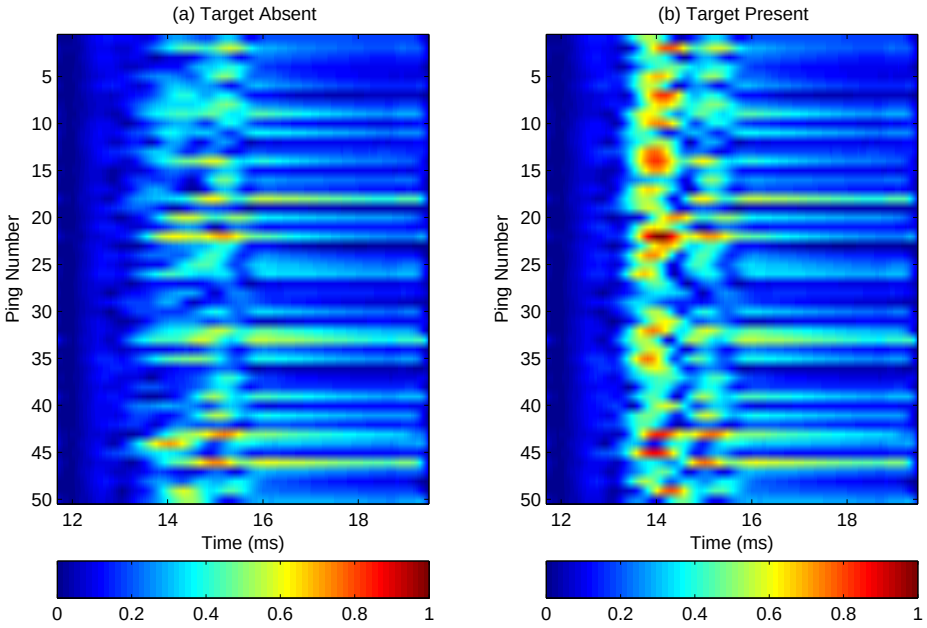

FIGURE 3.14: Waterfall plot of bubble cloud backscatter from a 6 kHz, 60 kPa pulse using TWIPS1b when a target is (a) absent; (b) present (TS = -20 dB).

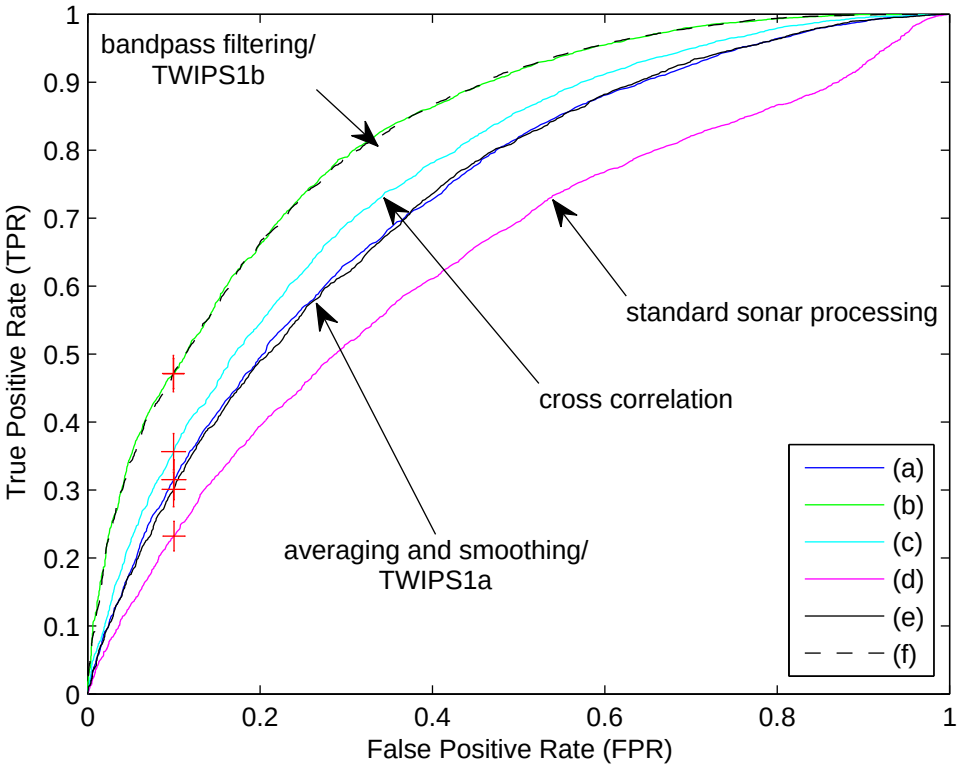

FIGURE 3.15: 6 kHz, 60 kPa pulse - Mean ROC curve with 95% CI (n = 50) at 0.1 FPR for (a) Averaging and smoothing; (b) Bandpass filtering; (c) Cross correlation; (d) Standard sonar processing; (e) TWIPS1a; (f) TWIPS1b.

amplitude response from the bubble cloud as observed from the waterfall plots in Figures 3.7 to 3.14 shows that both TWIPS1a and TWIPS1b perform better than standard sonar processing. The model will be used for simulating bubble/bubble cloud response from marine mammal bio-mimetic sonar in the following sections.

3.5 Response from porpoise echolocation chirp

The characteristics of an echolocation chirp from a finless porpoise were given in Chapter 2. A close approximation of a simulated porpoise chirp can be defined by applying a Hanning window to a 125 kHz sine wave with 9 cycles (corresponding to a duration of 72 μs. The amplitude of the simulated porpoise chirp was chosen to be 316 Pa (170 dB re 1 μPa @ 1m) which corresponds to the average sound pressure level of echolocation chirps emitted by finless porpoises measured in a closed river channel [26]. Figure 3.16 shows a comparison of the waveform and spectrum between a real and simulated porpoise chirp.

From Figure 3.16, it can be seen that the Hanning window sine wave approximation of a simulated porpoise chirp fits the signal characteristics of a real porpoise chirp signal. The noticeable difference between the real and simulated chirp is the small highlight at the tail of the real porpoise waveform which is caused by internal reverberation in the head. These small highlights have relatively low amplitude compared to the peak amplitude of the main pulse and therefore it would not have a significant effect on bubble backscatter.

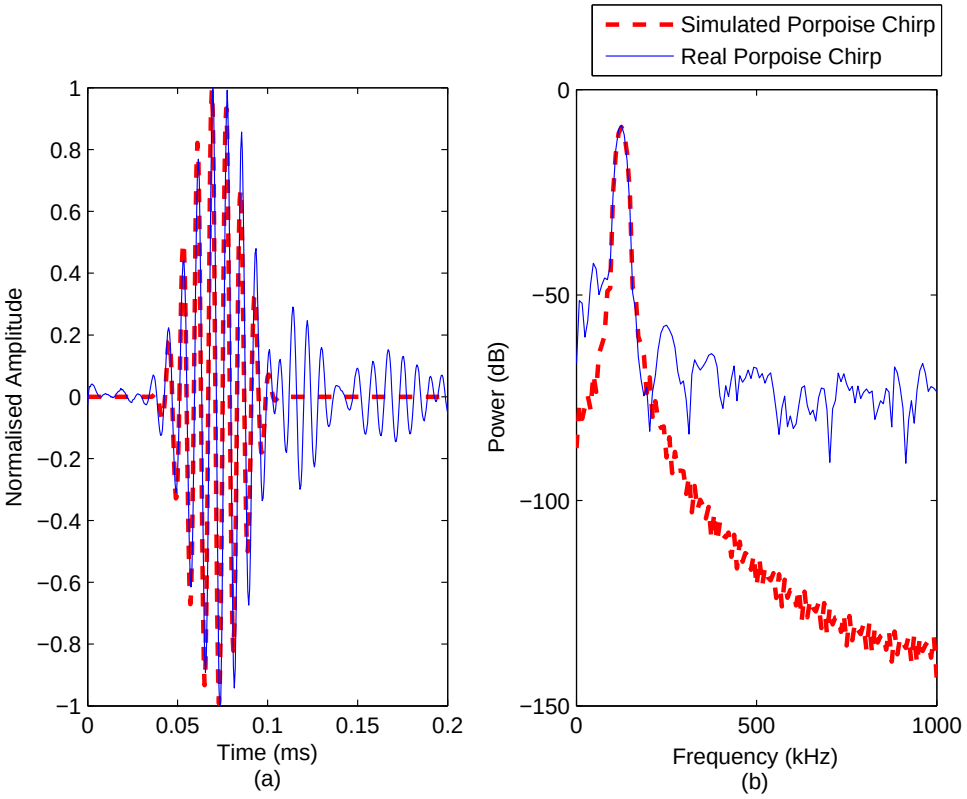

FIGURE 3.16: Comparison between the (a) waveform; (b) spectrum of a real and simulated porpoise chirp. *(Waveform of real porpoise chirp provided by Dr Tomonari Akamatsu, National Research Institute of Fisheries Engineering, Fisheries Research Agency, Japan).*

It was discussed earlier that the bubble distribution population used by Leighton *et al.* could have been misrepresented. The bubble population distribution used previously for the 6 kHz driving pulse example consists of 5 logarithmically spaced size bins with centre radii 10, 50, 100, 500, 1000 and 5000 μm. A rough estimate of the resonance frequency for each of these bubble sizes is 300, 60, 30, 6, 3 and 0.6 kHz, respectively. Since the resonance bubble size for a 125 kHz driving pulse is approximately 24 μm, the radius bins in bubble population distribution used previously will not give a good measure of nonlinear scattering in the bubble cloud here. It is believed that the authors could have scaled down the bubble population size to keep the void fraction low, so as to simplify the problem of bubble coupling.

In addition, they could have chosen the bubble size bins such that one or more of these bins correspond to the driving frequency they used in their simulation. Their objective was probably to generate as much nonlinearities as possible using the described bubble distribution in an attempt to illustrate the underlying principle behind TWIPS, which heavily relies on using nonlinearities in bubble scatters.

Other than Eq. 3.1 described by Meers *et al.*, other suitable models describing bubble size distribution were unavailable for this research despite a comprehensive literature search. Most of the bubble size distributions described in existing literatures were experimental data presented in the form of plots which were difficult to extract numerical information from. As such, Table 3.1 was used, with the 50 μm bin replaced by a 25 μm bin. This arrangement would allow few modifications to the population distribution while maintaining the same reasonably low void fraction.

Considering the low sound pressure levels in porpoise chirps, it was not practical to perform the simulation with the sound source at 10 m from the bubble cloud since the signal would have been severely attenuated due to spreading loss by the time it reached the target in the cloud. In fact, it will be shown later that the sound source amplitude at much closer distances (in the range of 1 - 2 m) will still be insufficient to generate highly nonlinear responses. Nevertheless, in this simulation performed, the sound source (simulated porpoise chirp) was chosen to be at 2 m from the centre of the bubble cloud, which was the closest reasonable distance to use.

3.5.1 Single bubble response

The backscatter response for bubbles with radii 10, 25, 100, 500, 1000 and 5000 μm is given in Figure 3.18. The amplitude of the porpoise chirp is much too low to excite significant nonlinearities in the bubble responses. As such, one expects the backscatter from all bubble sizes to be mostly linear and bigger bubbles will scatter more energy. The frequency responses from the different bubble sizes appear relatively similar in spectral composition and do not show any significant harmonic peaks. The effects of pulse inversion is straightforward in this case because of the lack of harmonic peaks. The signal has twice its original amplitude when the responses from inverted pulses are subtracted from one another. On the other hand, the amplitude of the signal is greatly reduced when summing the response from inverted pulses.

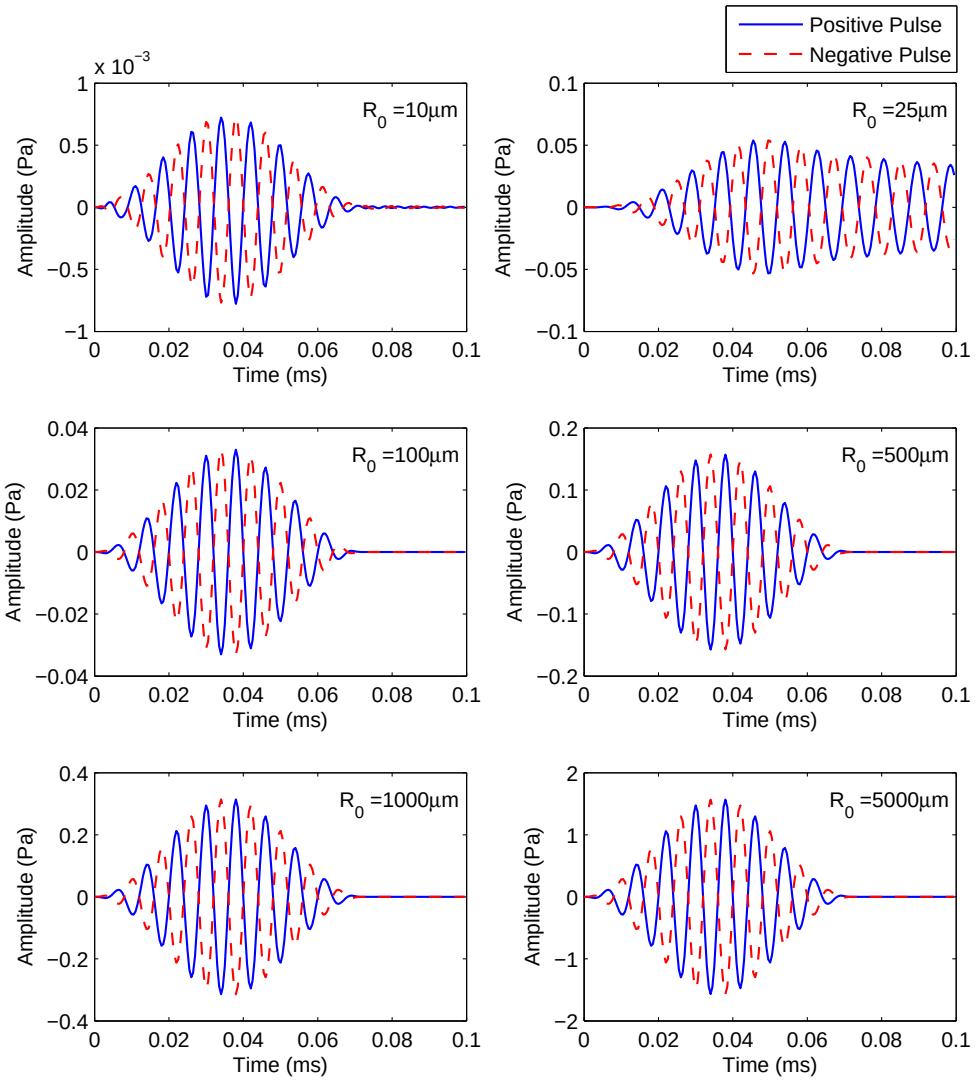

FIGURE 3.17: Waveforms illustrating the backscatter from bubbles with radii 10, 50, 100, 500, 1000 and 5000 μm, when driven by a positive and negative simulated porpoise chirp at 316 Pa.

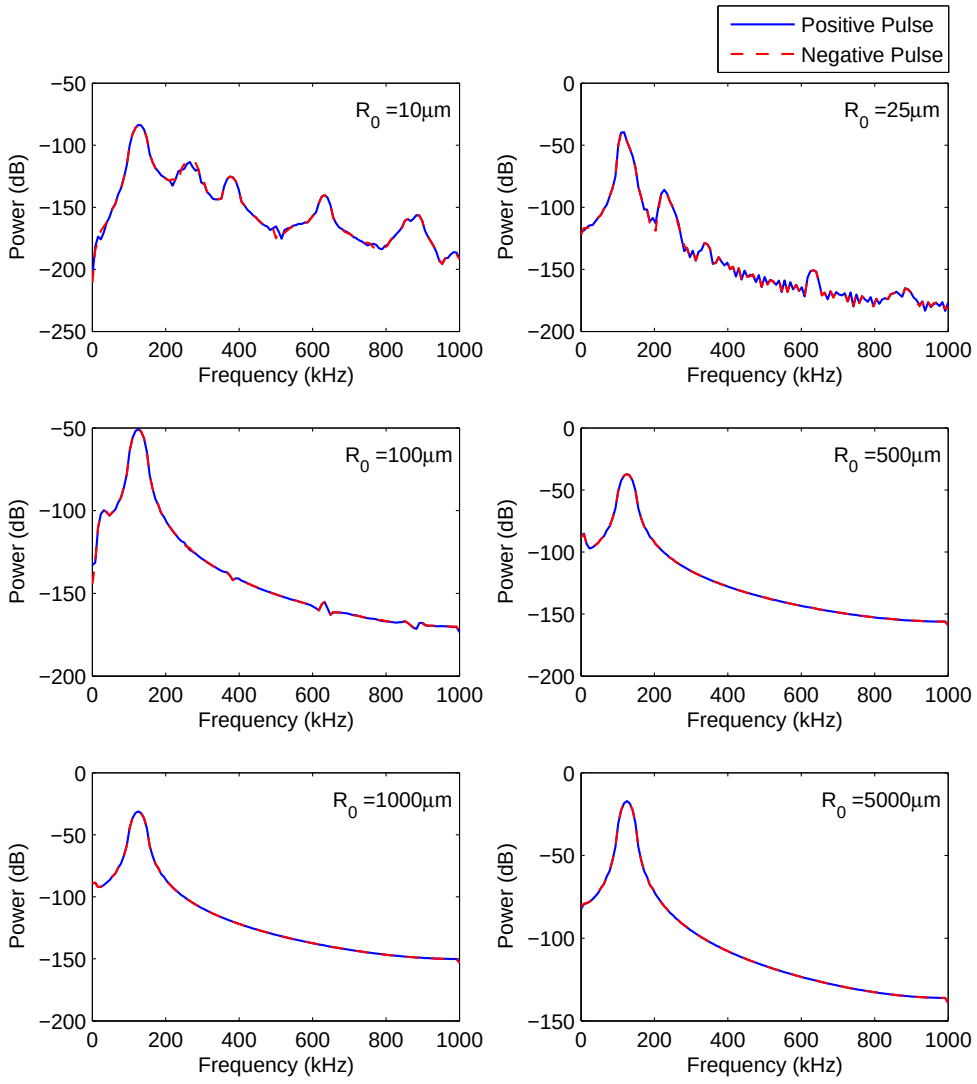

FIGURE 3.18: Frequency response plots illustrating the backscatter from bubbles with radii 10, 50, 100, 500, 1000 and 5000 μm, when driven by a positive and negative simulated porpoise chirp at 316 Pa.

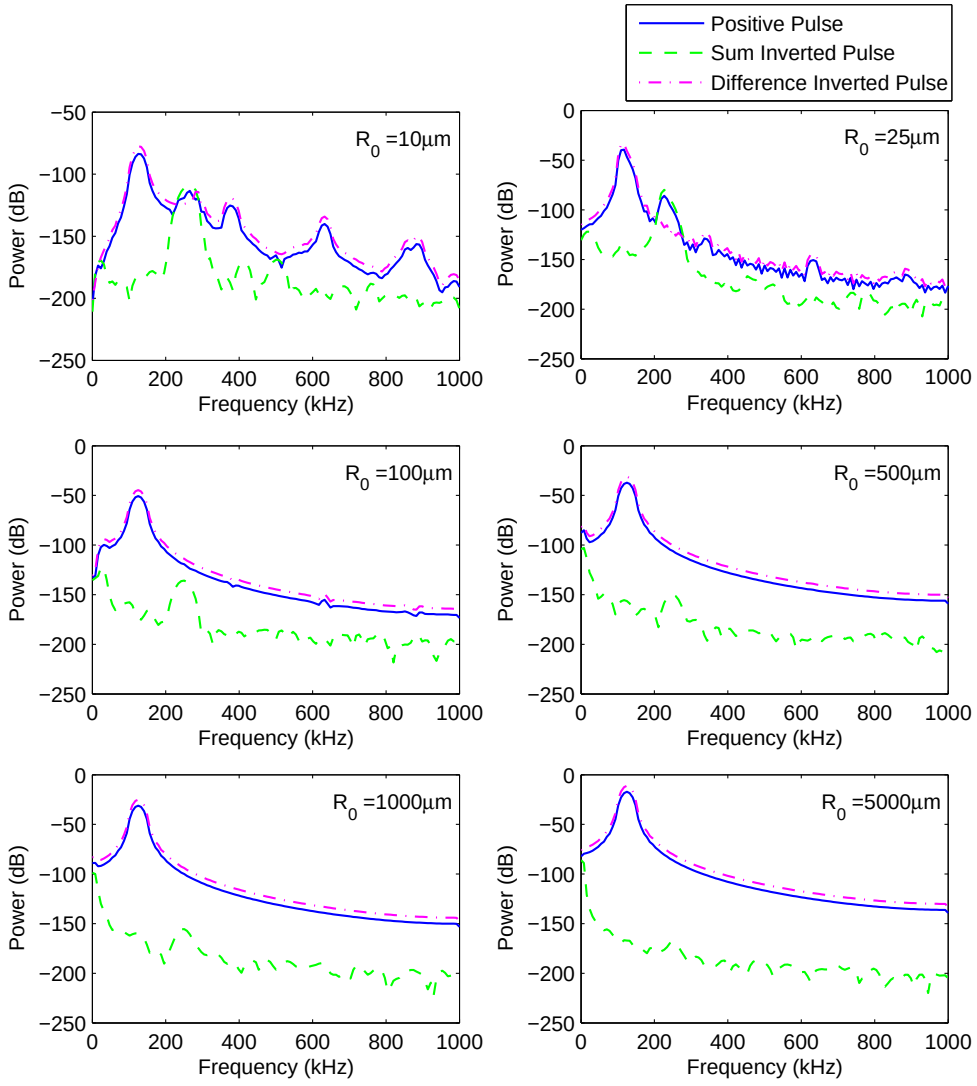

FIGURE 3.19: Frequency response plots illustrating the summation/subtraction of backscatter from bubbles with radii 10, 50, 100, 500, 1000 and 5000 μm, when driven by a positive and negative simulated porpoise chirp at 316 Pa.

It was mentioned earlier that finless porpoises produce peak to peak source levels estimated with range of 163 to 186 dB re 1 μPa @ 1 m. However, in a more recent study of wild harbour porpoises (*Phocoena phocoena*) by Villadsgaard *et al.* (2007)[42], it was suggested that the back-calculated source level measured from this species ranged from 178 to 205 dB re 1 μPa @ 1 m with a mean source level of 191 dB re 1 μPa @ 1 m. This measurement was 30 dB more than that measured from animals in captivity. The spectral and temporal properties were comparable. Studies have shown that bottlenose dolphins (*Tursiops truncatus*) alter their sound output levels according to their environments, thus this observation in wild harbour porpoises is not surprising. However, these high source levels might have only been produced by larger porpoises as studies have also shown that echolocation source level is attributed to the physical size of the animals.

To illustrate the effects of pulse amplitude on bubble oscillations, the bubble responses are calculated again with the same set of parameters used for the simulated finless porpoise chirp except that the signal amplitude has been increased to 10 kPa (200 dB re 1 μPa @ 1 m). It is important to note that there have not been any recent records of finless porpoises producing these source levels.

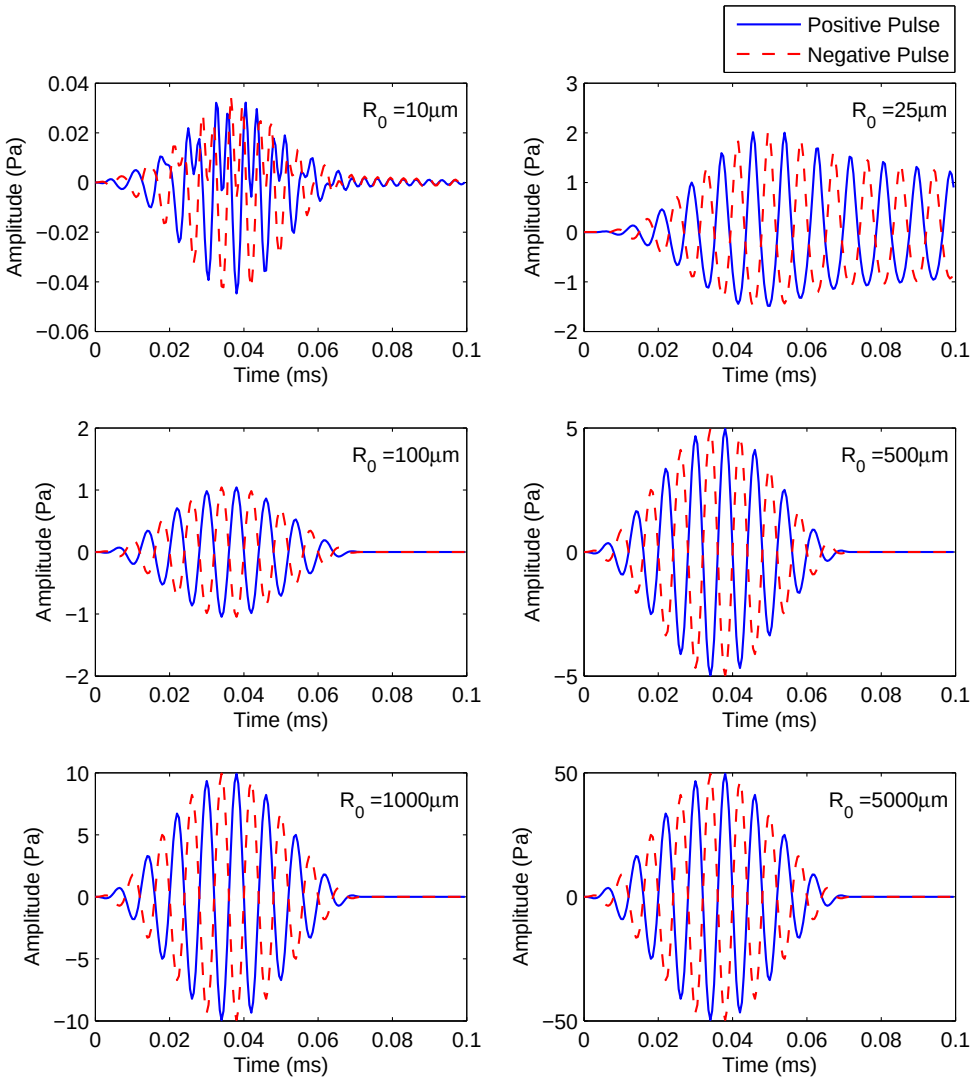

FIGURE 3.20: Waveforms illustrating the backscatter from bubbles with radii 10, 50, 100, 500, 1000 and 5000 μm, when driven by a positive and negative simulated porpoise chirp at 10 kPa.

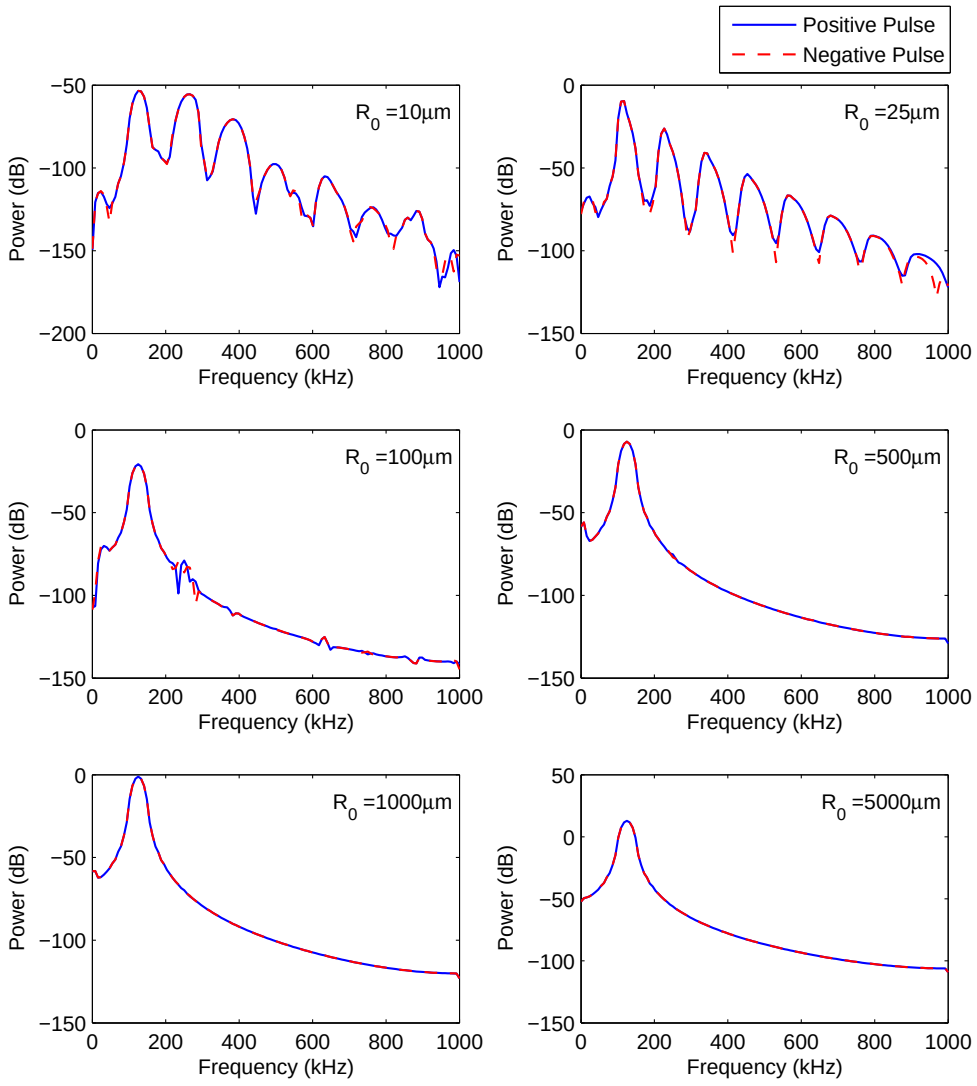

FIGURE 3.21: Frequency response plots illustrating the backscatter from bubbles with radii 10, 50, 100, 500, 1000 and 5000 μm, when driven by a positive and negative simulated porpoise chirp at 10 kPa.

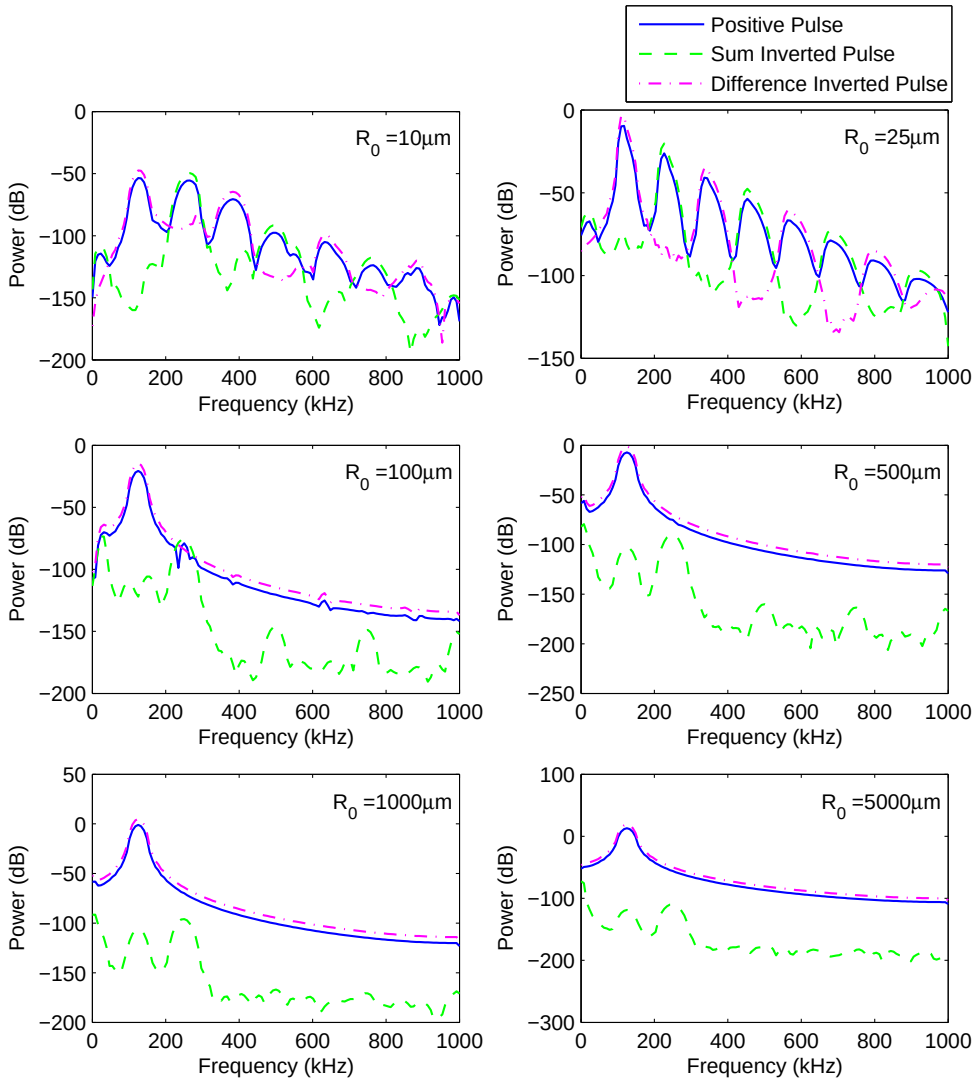

FIGURE 3.22: Frequency response plots illustrating the summation/subtraction of backscatter from bubbles with radii 10, 50, 100, 500, 1000 and 5000 μm, when driven by a positive and negative simulated porpoise chirp at 10 kPa.

The waveform plot in Figure 3.20 shows some evidence of nonlinear scattering in bubbles with radii 10 and 25 μm. This result is expected because the bubble resonance size is approximately 24 μm. The other larger bubbles all appear to scatter linearly. The frequency response plot in Figure 3.21 shows harmonic dispersion in bubbles with radii 10 and 25 μm but the frequency responses are almost similar for both the inverted and non-inverted driving pulse unlike the highly nonlinear

response observed previously in Figure 3.3. The results from pulse inversion do show the enhancement and suppression of harmonics. However, how significant this weak nonlinear response may help in contrast enhancement needs to be further assessed. This will be discussed in the next subsection on the response from the entire bubble cloud.

3.5.2 Cloud response

The methodology for calculating the bubble cloud response from a simulated porpoise chirp follows the 6 kHz driving pulse example discussed previously. The main difference is the type of signal used to ensonify the cloud and the distance of ensonification. The simulated porpoise chirp has a centre frequency of 125 kHz, hence it excites a different population of resonance bubble size in the bubble cloud. In addition, the simulated porpoise chirp has a much lower source level compared to the 6 kHz driving pulse, which would therefore not generate as much nonlinearities in the bubble cloud. In this example using simulated porpoise chirps, the distance of ensonification is 2 m whereas the 6 kHz example used an ensonification distance of 10 m. The reason for this is because TWIPS requires nonlinear response from bubbles in order to operate effectively hence the low amplitude simulated porpoise chirp needs to drive the bubbles in the cloud at close ranges. In the later part of this section, the driving amplitude of the simulated porpoise chirp at measured at 1 m from the source is increase from 316 Pa to 10 kPa. This is to compare the effects of amplitude on bubble cloud backscatter response and the performance among the different signal processing methods.

The narrowband bandpass filter used in this example is a digital FIR equiripple filter. The filter has a passband gain of 1 dB from 110 to 140 kHz and a stopband gain of -80 dB at the 100 and 150 kHz cutoff frequencies. The magnitude response of the filter is shown in Figure 3.23.

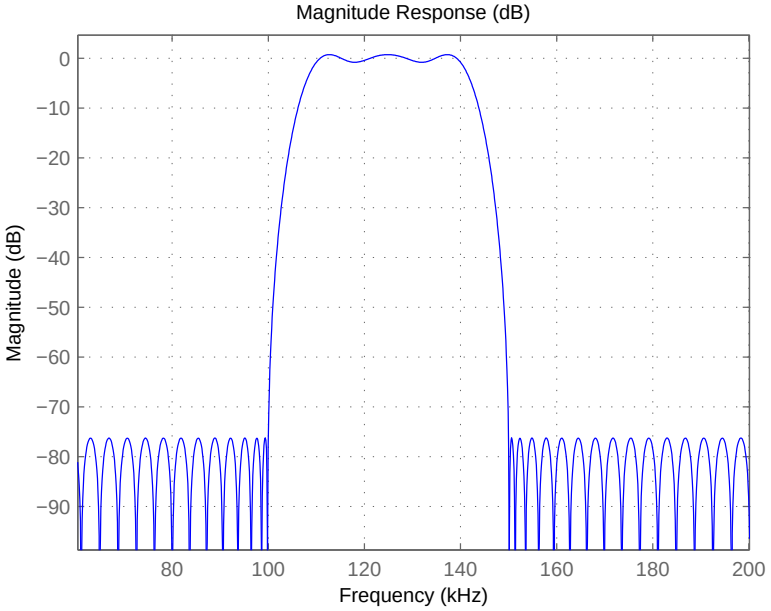

FIGURE 3.23: Magnitude response of a 125 kHz bandpass filter used in the simulations.

The waterfall plots illustrating contrast between the presence and absence of a linear scattering target (TS = -20 dB) when ensonified by a porpoise chirp (zero to peak amplitude = 316 Pa measured at 1 m from the source) transmitted 2 m from the centre of the bubble cloud is shown in Figures 3.24 to 3.29.

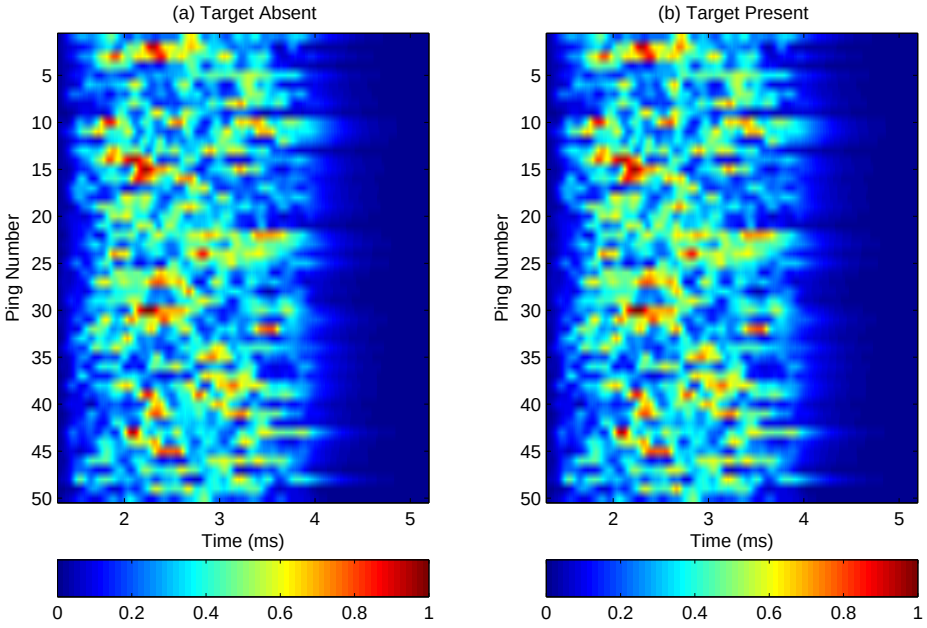

FIGURE 3.24: Waterfall plot of bubble cloud backscatter from a simulated porpoise chirp at 316 Pa using averaging and smoothing when a target is (a) absent; (b) present (TS = -20 dB).

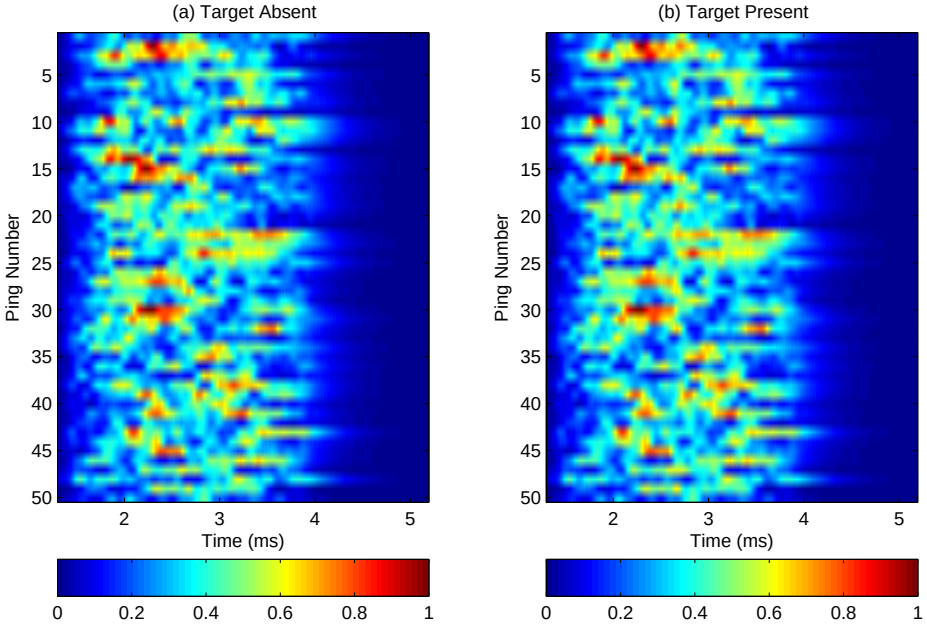

FIGURE 3.25: Waterfall plot of bubble cloud backscatter from a simulated porpoise chirp at 316 Pa using bandpass filtering when a target is (a) absent; (b) present (TS = -20 dB).

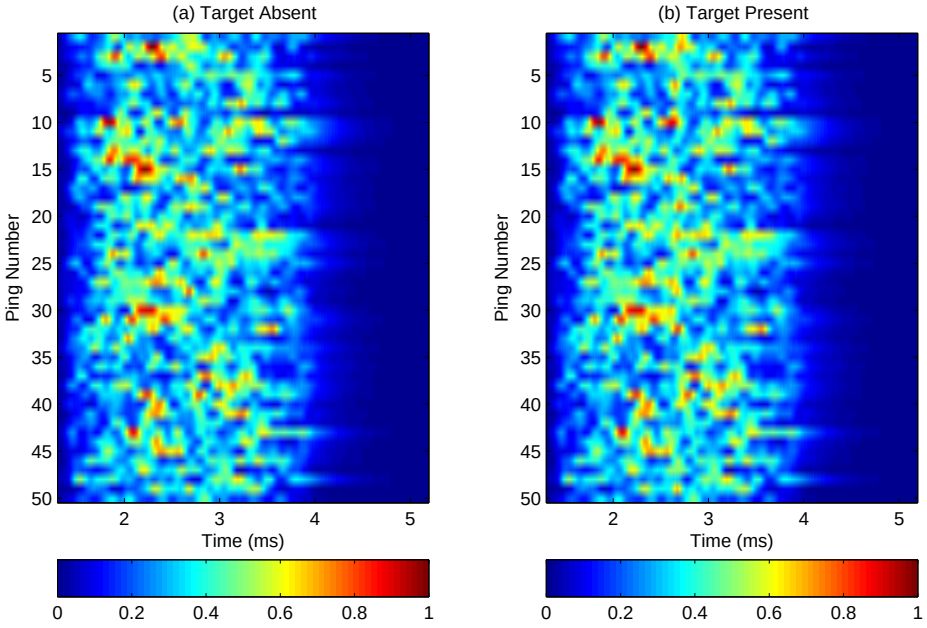

FIGURE 3.26: Waterfall plot of bubble cloud backscatter from a simulated porpoise chirp at 316 Pa using cross correlation when a target is (a) absent; (b) present (TS = -20 dB).

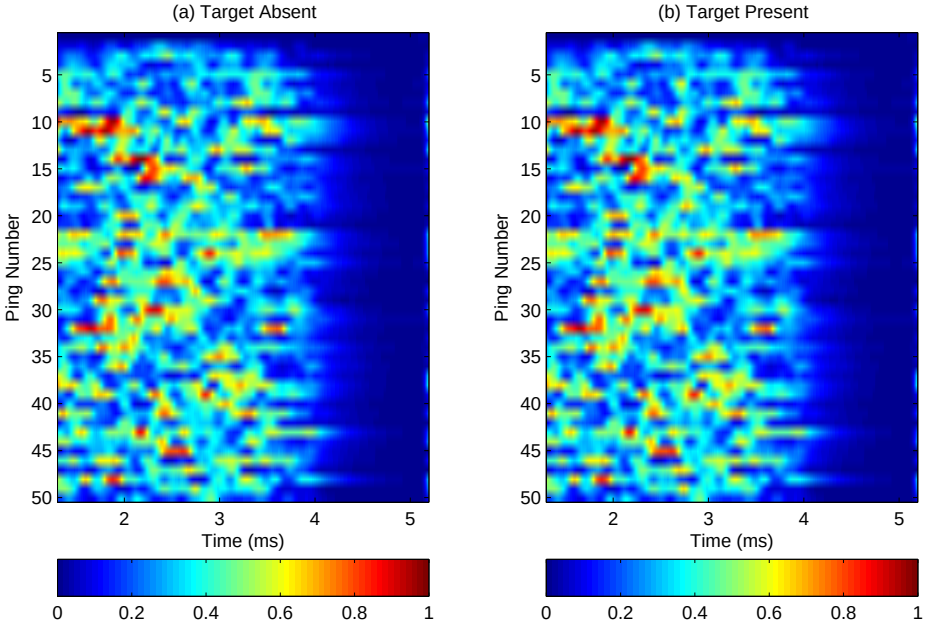

FIGURE 3.27: Waterfall plot of bubble cloud backscatter from a simulated porpoise chirp at 316 Pa using standard sonar processing when a target is (a) absent; (b) present (TS = -20 dB).

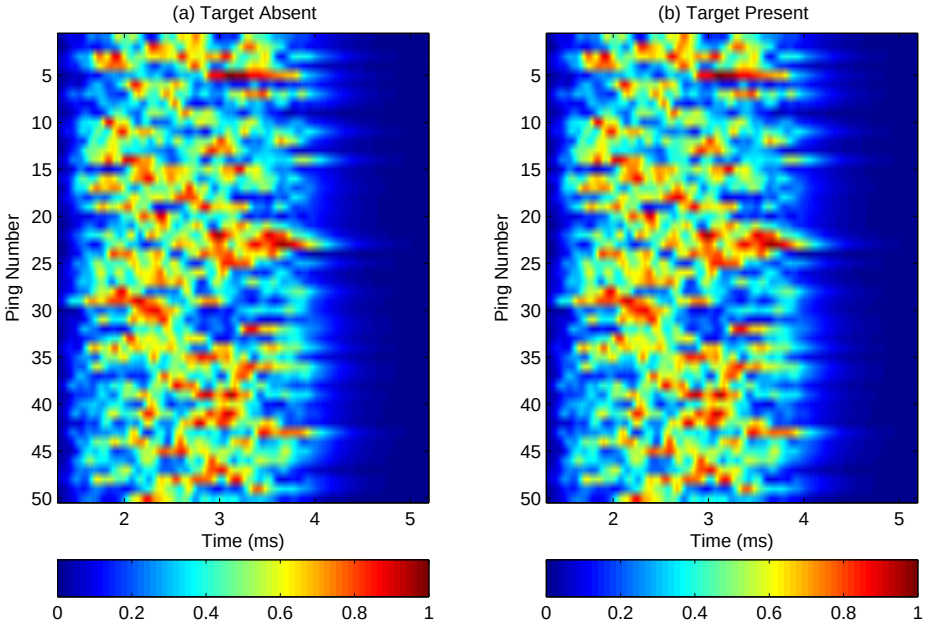

FIGURE 3.28: Waterfall plot of bubble cloud backscatter from a simulated porpoise chirp at 316 Pa using TWIPS1a when a target is (a) absent; (b) present (TS = -20 dB).

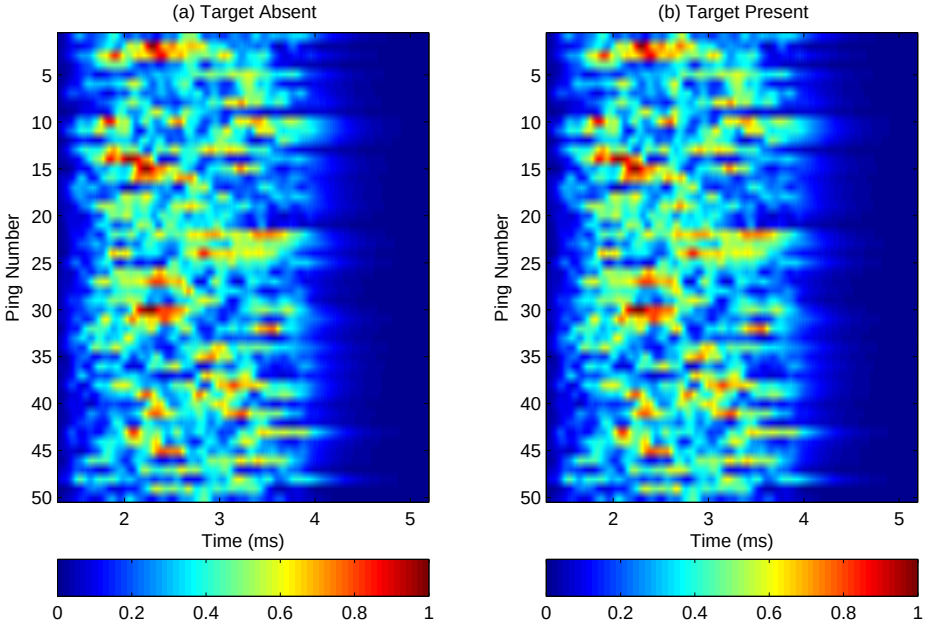

FIGURE 3.29: Waterfall plot of bubble cloud backscatter from a simulated porpoise chirp at 316 Pa using TWIPS1b when a target is (a) absent; (b) present (TS = -20 dB).

From Figures 3.24 to 3.29, it is observed that there is no distinct contrast between the target present and absent conditions for all the different signal processing methods. This could be due to the fact that the driving sound pressure level is too weak so that the amplitude of the backscatter from the target is much lower compared to the amplitude of the backscatter from the bubbles in the cloud. Clearly, this set of results is not useful for comparing the performance between the different signal processing methods. But it does show that the low sound pressure level in porpoise echolocation chirps are not useful for detection in bubble populated water.

The target strength of the linear target also plays a part in the target/bubble cloud contrast results. A higher target strength could give a better result. In order to illustrate the effects of linear scattering in bubbles and the performance among the different signal processing methods in this particular example, the target strength of the linear target is increased such that it starts to appear vaguely in the cloud. For that, a target strength of -10 dB is used.

The waterfall plots when using a target strength of -10 dB for the linear target show an improvement in the contrast between target present and absent in the bubble cloud. Based on visual observations of Figures 3.30 to 3.35, again, the cross correlation method gives the best contrast compare to the rest of the methods. This method also reduces noise in the 'target absent' condition and therefore general background noise so a low target strength return should be clearer.

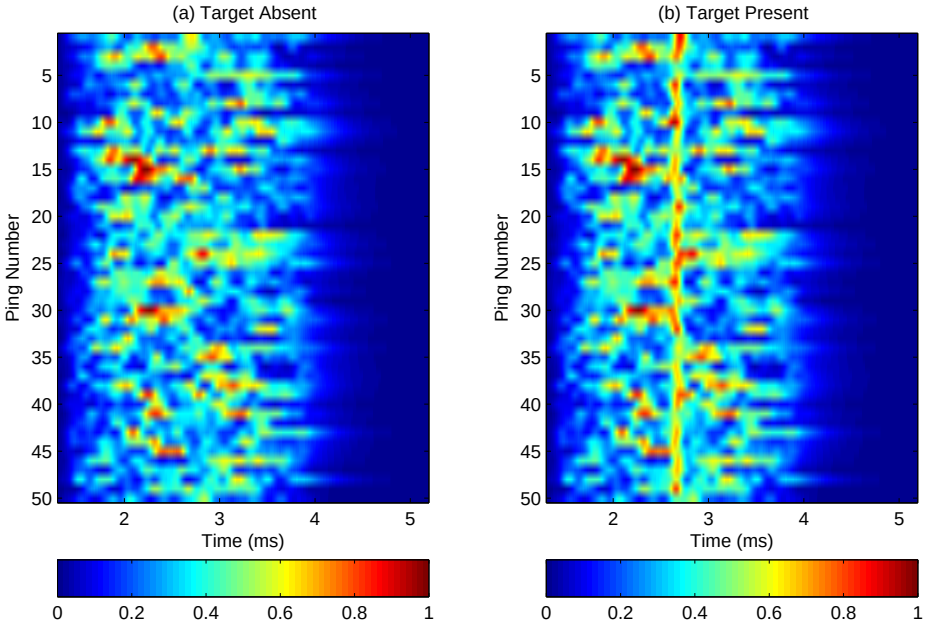

FIGURE 3.30: Waterfall plot of bubble cloud backscatter from a simulated porpoise chirp at 316 Pa using averaging and smoothing when a target is (a) absent; (b) present (TS = -10 dB).

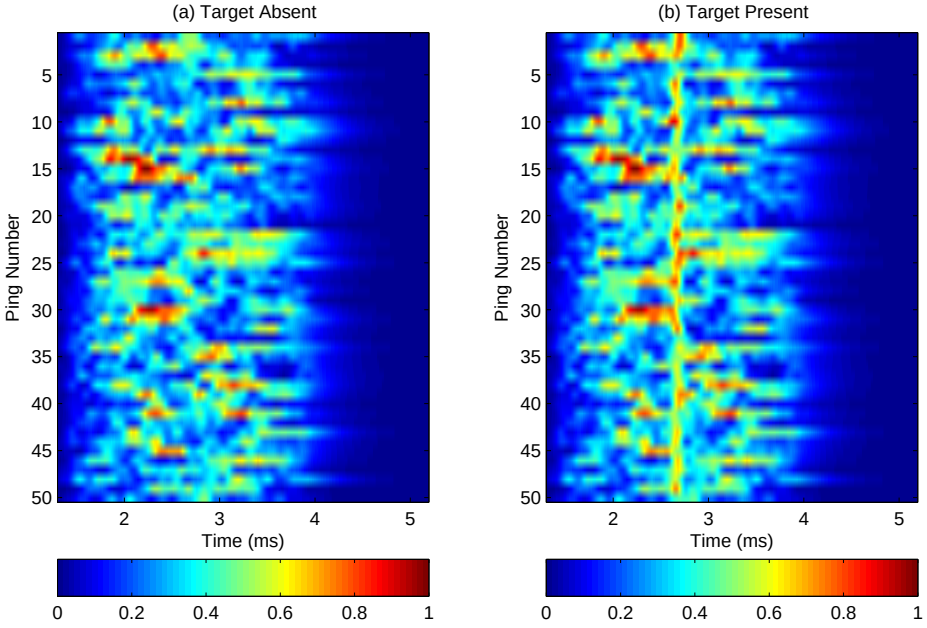

FIGURE 3.31: Waterfall plot of bubble cloud backscatter from a simulated porpoise chirp at 316 Pa using bandpass filtering when a target is (a) absent; (b) present (TS = -10 dB).

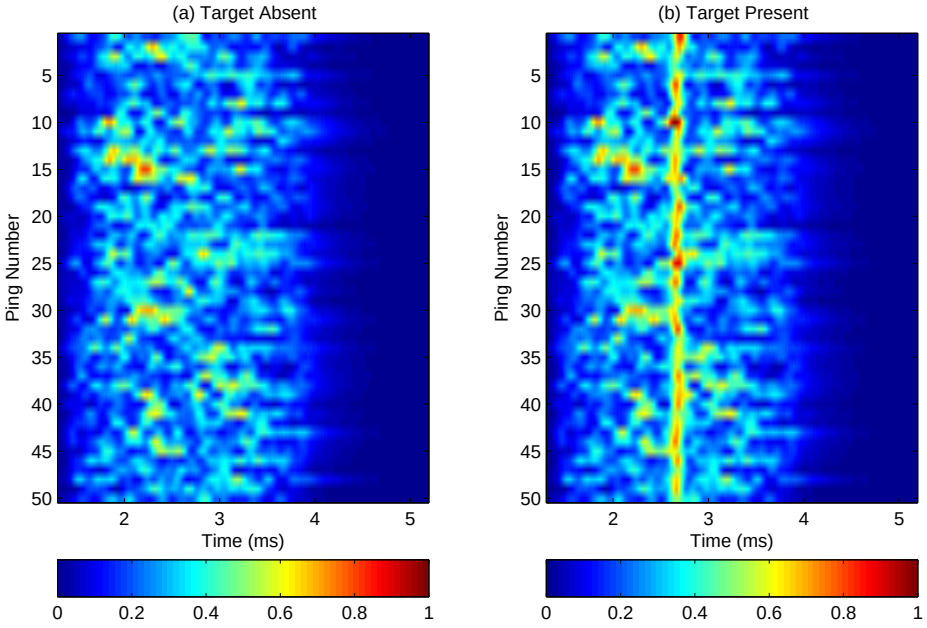

FIGURE 3.32: Waterfall plot of bubble cloud backscatter from a simulated porpoise chirp at 316 Pa using cross correlation when a target is (a) absent; (b) present (TS = -10 dB).

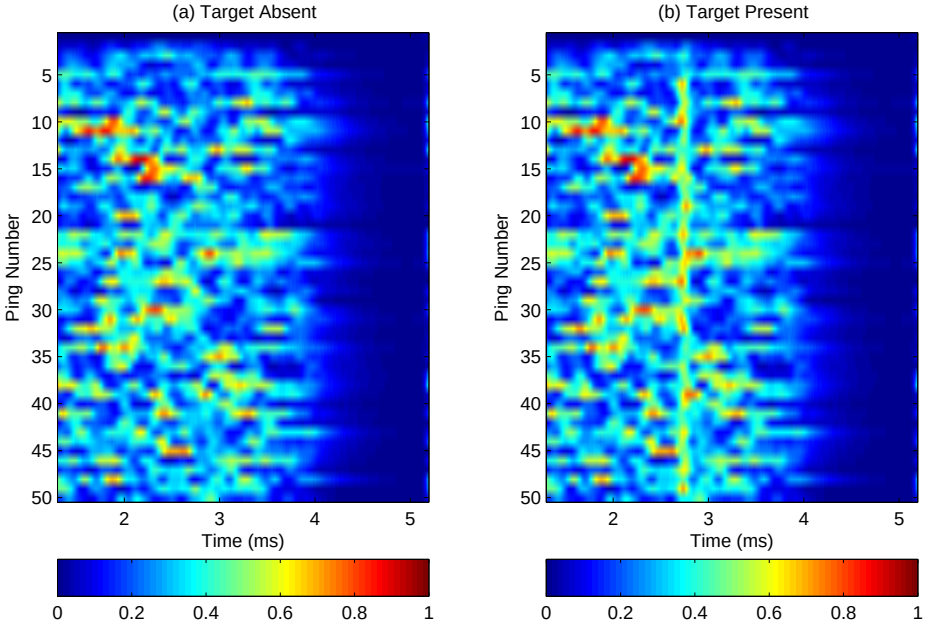

FIGURE 3.33: Waterfall plot of bubble cloud backscatter from a simulated porpoise chirp at 316 Pa using standard sonar processing when a target is (a) absent; (b) present (TS = -10 dB).

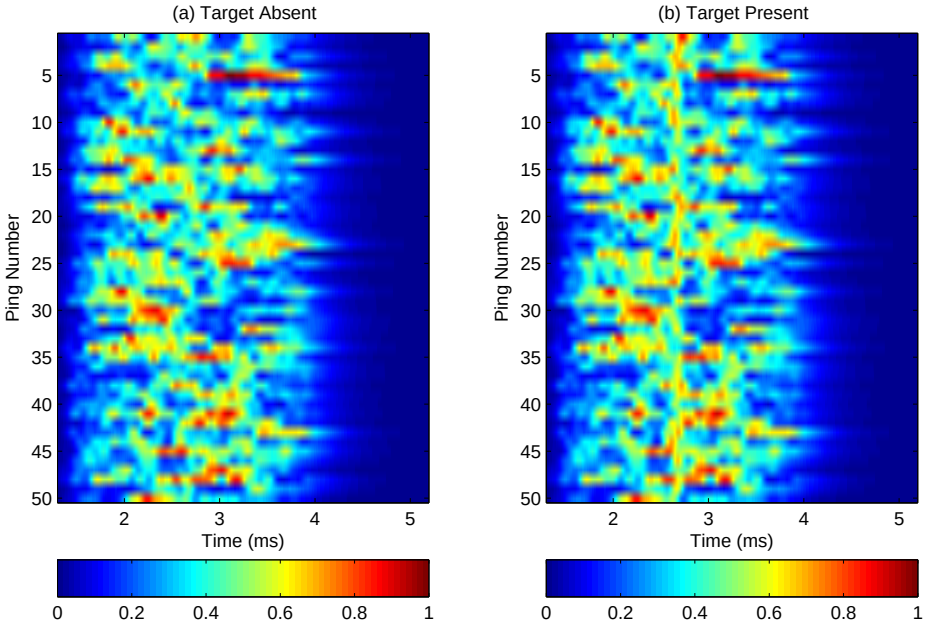

FIGURE 3.34: Waterfall plot of bubble cloud backscatter from a simulated porpoise chirp at 316 Pa using TWIPS1a when a target is (a) absent; (b) present (TS = -10 dB).

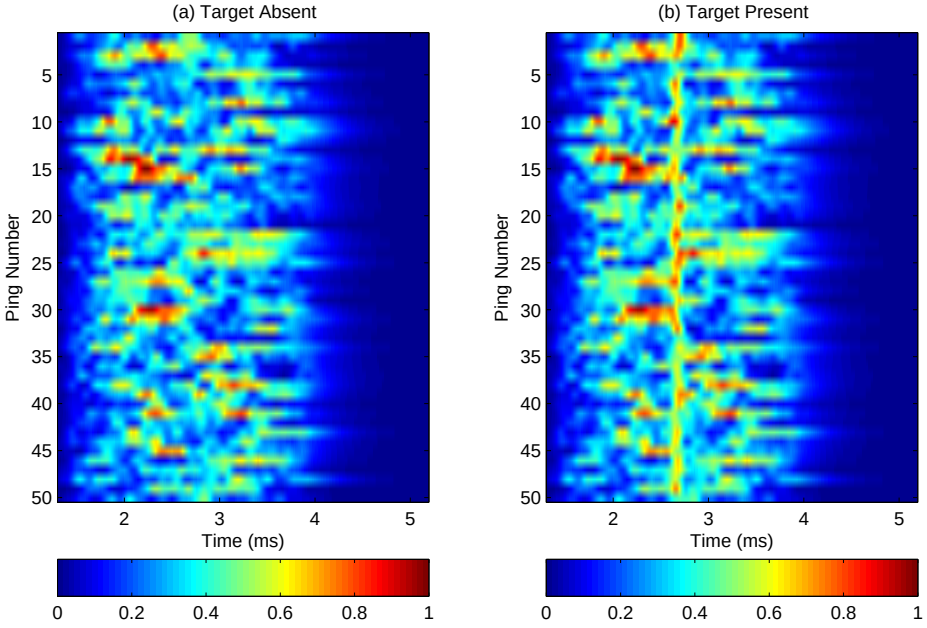

FIGURE 3.35: Waterfall plot of bubble cloud backscatter from a simulated porpoise chirp at 316 Pa using TWIPS1b when a target is (a) absent; (b) present (TS = -10 dB).

The SNR for different processing methods result is averaged over 50 pings and presented in Table 3.4.

Table 3.4: Comparison of SNR for different processing methods - simulated porpoise chirp at 316 Pa.

Signal processing	SNR
Averaging and smoothing	0.089
Bandpass filtering	0.080
Cross correlation	0.187
Standard sonar processing	0.060
TWIPS1a	0.036
TWIPS1b	0.079

From Table 3.4, the cross correlation method gives the highest SNR, followed by the basic averaging and smoothing method. Bandpass filtering and TWIPS1b have almost the same performance, both just slightly worse than basic averaging and smoothing. Standard sonar processing has the second worst SNR followed by TWIPS1a. This result is not surprising because of the linear scatters from both bubbles and target which makes discriminating between them difficult.

The ROC curve shows that the cross correlation method significantly outperforms all the other methods. On the other hand, there seems to be no improvement in using bandpass filtering or TWIPS1b compared to the basic averaging and smoothing method as they all have overlapping confidence intervals. In addition, their ROC curves lie fairly close to the diagonal of uncertainty. More interestingly, the ROC curves for TWIPS1a and standard sonar processing have a convex shape. This signifies that these methods have a higher probability of making false alarms than correct detections. From Figure 3.34, despite being able to observe a vertical indicating the scattering from the linear target, one can also notice bubble noise

of equivalent or higher amplitude in other areas not occupied by the target. This bubble noise contributed to the very high false alarm rates, thus a convex ROC curve.

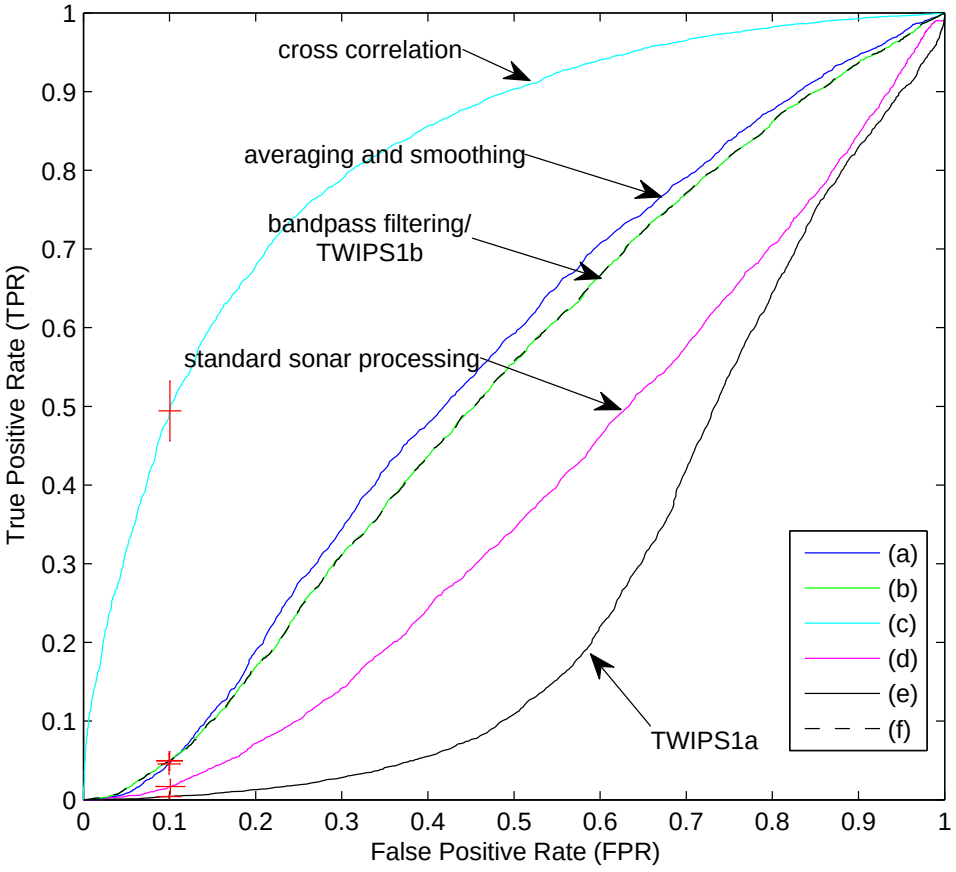

FIGURE 3.36: Simulated porpoise chirp at 316 Pa - Mean ROC curve with 95% CI (n = 50) at 0.1 FPR for (a) Averaging and smoothing; (b) Bandpass filtering; (c) Cross correlation; (d) Standard sonar processing; (e) TWIPS1a; (f) TWIPS1b.

The previous example dealt with linear scattering in the bubble cloud due to the simulated porpoise chirp having a low zero to peak amplitude of 316 Pa (measured at 1 m from the source). It was stated previously that TWIPS1 rely on nonlinearities to improve linear target contrast enhancement in nonlinear bubble

scatters. The previous example was lacking this condition hence this could have been a contributing factor the results shown.

It was also shown previously that by increasing the amplitude of the signal to 10 kPa (measured at 1 m from the source), non-linearities were observed for bubbles with radii 25μm and below. Using this amplitude for the simulated porpoise chirp would therefore generate the condition for improving TWIPS1. When the simulation was performed again using a target (TS = -20 dB), hidden in the centre of the bubble cloud at 2 m from the sound source, the same problem of very poor SNR was encountered. As such, the target strength was again increased to -10 dB where the target was just barely visible in the waterfall plot for the raw backscatter. The following figures show the simulation results using a simulated porpoise chirp with a higher zero to peak amplitude of 10 kPa (measured at 1 m from source) and a target strength of -10 dB for the linear target.

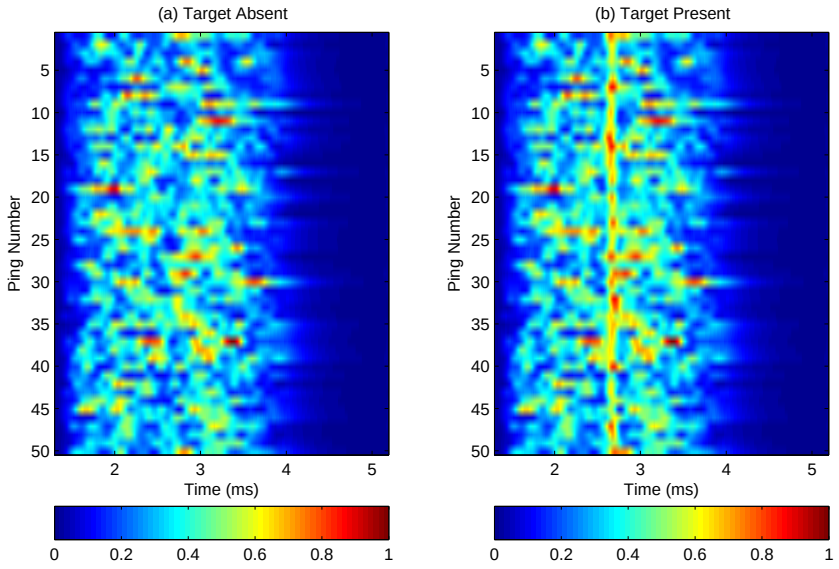

FIGURE 3.37: Waterfall plot of bubble cloud backscatter from a simulated porpoise chirp at 10 kPa using averaging and smoothing when a target is (a) absent; (b) present (TS = -10 dB).

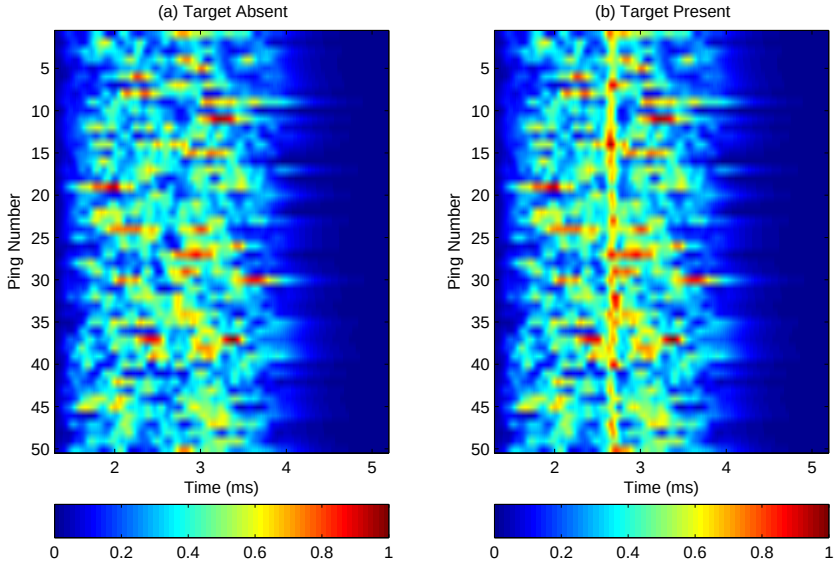

FIGURE 3.38: Waterfall plot of bubble cloud backscatter from a simulated porpoise chirp at 10 kPa using bandpass filtering when a target is (a) absent; (b) present (TS = -10 dB).

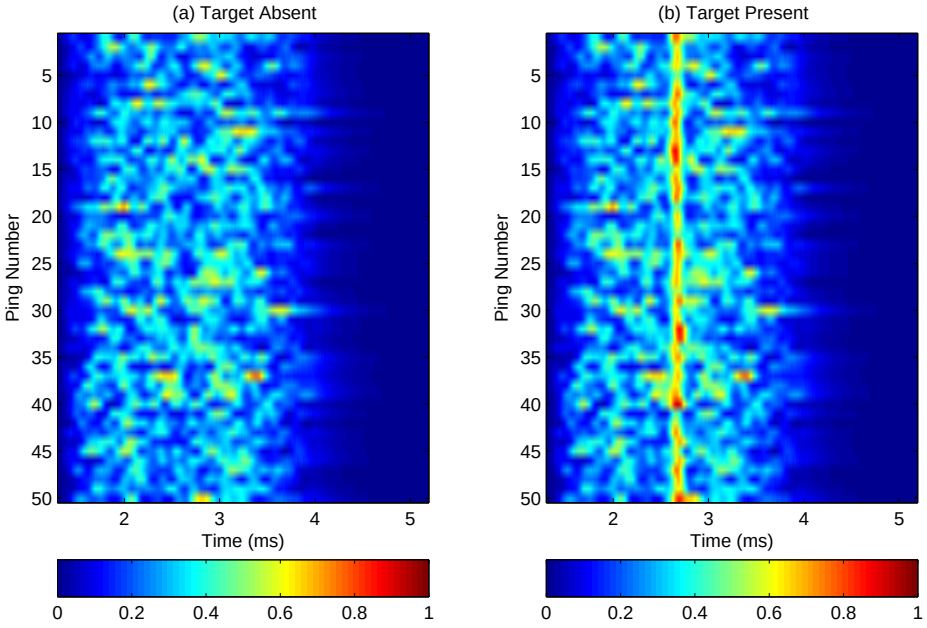

FIGURE 3.39: Waterfall plot of bubble cloud backscatter from a simulated porpoise chirp at 10 kPa using cross correlation when a target is (a) absent; (b) present (TS = -10 dB).

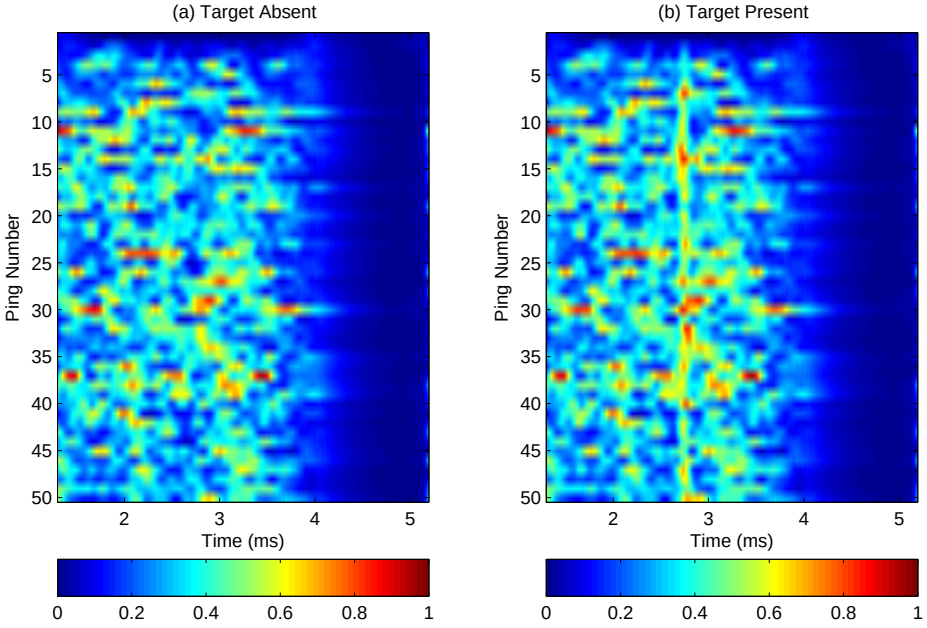

FIGURE 3.40: Waterfall plot of bubble cloud backscatter from a simulated porpoise chirp at 10 kPa using standard sonar processing when a target is (a) absent; (b) present (TS = -10 dB).

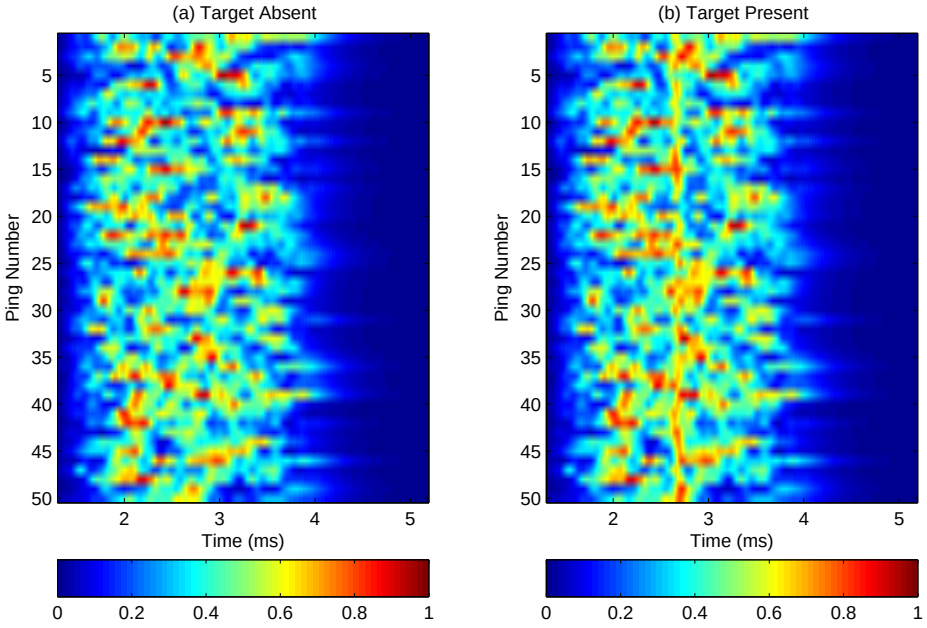

FIGURE 3.41: Waterfall plot of bubble cloud backscatter from a simulated porpoise chirp at 10 kPa using TWIPS1a when a target is (a) absent; (b) present (TS = -10 dB).

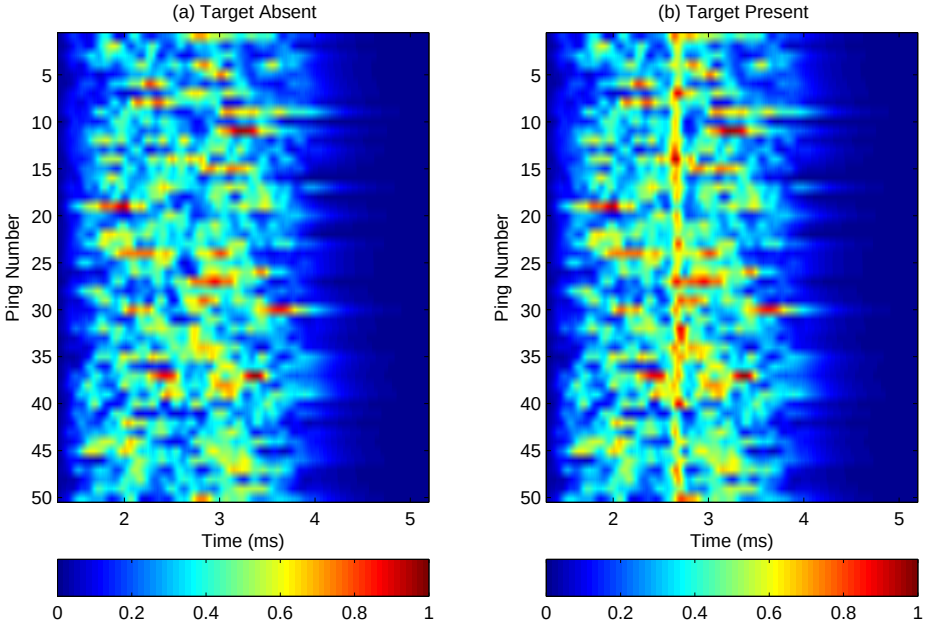

FIGURE 3.42: Waterfall plot of bubble cloud backscatter from a simulated porpoise chirp at 10 kPa using TWIPS1b when a target is (a) absent; (b) present (TS = -10 dB).

From Figures 3.37 to 3.42, it seems like the increase in driving pulse amplitude did not make significant difference in the results when compare to the previous simulation which used a much lower driving signal amplitude. Although there is a slight increase in SNR across all the different processing methods, their order of performance remains unchanged.

TABLE 3.5: Comparison of SNR for different processing methods - simulated porpoise chirp at 10 kPa.

Signal processing	SNR
Averaging and smoothing	0.093
Bandpass filtering	0.087
Cross correlation	0.199
Standard sonar processing	0.060
TWIPS1a	0.046
TWIPS1b	0.087

The ROC curve in Figure 3.43 compared to Figure 3.36 also shows no significant improvement in performance among the different processing methods.

In this section, the backscatter pressure amplitude response of a bubble cloud when ensonified by a simulated porpoise chirp is presented. It was observed that the low sound pressure levels produced by porpoises require a much shorter distance between the sound source and bubble cloud. In addition, a higher target strength (i.e -10 dB) is required in order for proper detection of a target within in the bubble cloud. Among all the different signal processing methods considered, cross correlation gives the best performance in target detection. The basic averaging and smoothing method perform equally bad with the bandpass filtering and TWIPS1b methods. These methods have a less than 10 % correct detection rate for an allowed tolerance of 10 % error. Their ROC curves lie close to the diagonal

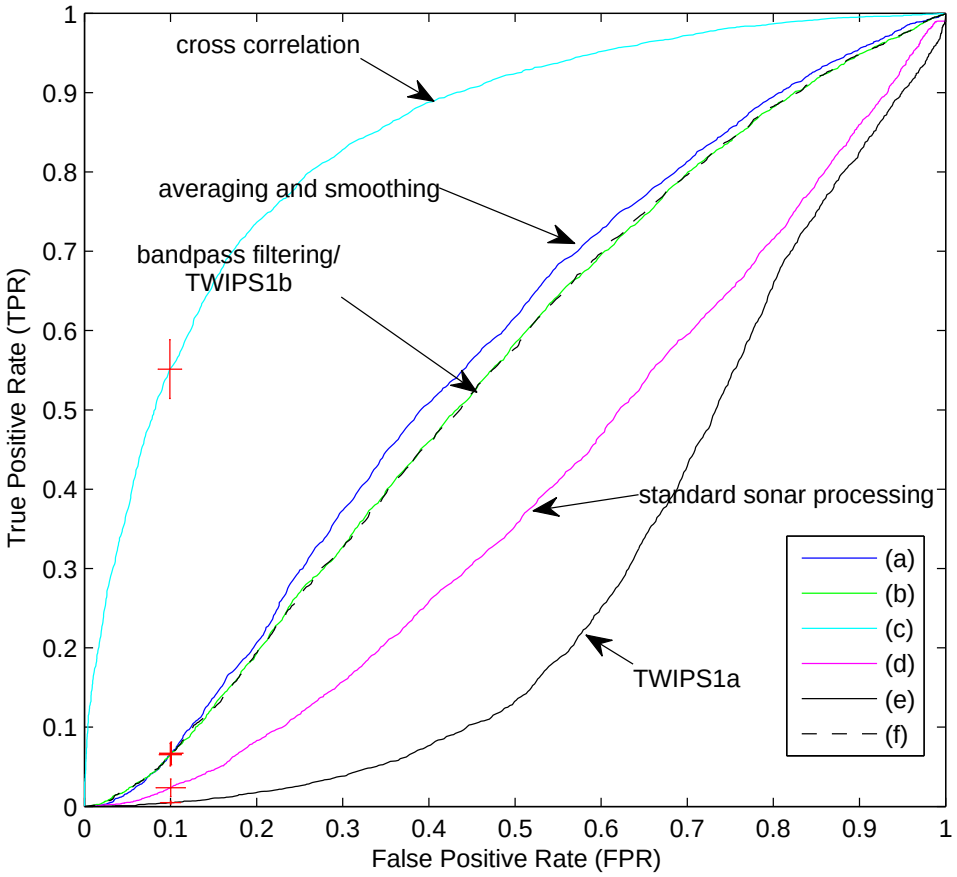

FIGURE 3.43: Simulated porpoise chirp at 10 kPa - Mean ROC curve with 95% CI (n = 50) at 0.1 FPR for (a) Averaging and smoothing; (b) Bandpass filtering; (c) Cross correlation; (d) Standard sonar processing; (e) TWIPS1a; (f) TWIPS1b.

of uncertainty indicating that the detection approximated a random guess. It is more disappointing to observe that the standard sonar processing and TWIPS1a methods have a higher probability of making mistakes than making correct detections. It doesn't make much of a difference to use a signal amplitude of 316 Pa or 10 kPa as both did not generate enough nonlinearities in the cloud for some of the proposed methods to work well.

In the next section, the backscatter response from a bubble and bubble cloud ensonified by a simulated dolphin echolocation clicks will be discussed. In general,

dolphins produce echolocation click with sound pressure levels much higher than porpoises, and thus have a better chance of generating strong nonlinearities in bubble clouds. As such, it is expected that there should be some differences in the performance of the various signal processing methods.

3.6 Response from a typical dolphin echolocation click

Bottlenose dolphin echolocation clicks are characterised by high energy, short durations and broad bandwidths. Unlike porpoise chirps, echolocation clicks produced by bottlenose dolphins have source levels of up to 220 dB re 1 μPa @ 1 m, which are sufficiently high to drive bubbles into highly nonlinear oscillations.

Au (1993) reported that a typical sonar click of an Atlantic bottlenose dolphin (*Tursiops truncatus*) resembles an exponentially damped sinusoidal wave with a duration between 40 and 70 μs and with 4 to 10 positive excursions [17]. He used a mathematical expression consisting of a Gabor function and a Gaussian curve to describe a simulated dolphin click.

$$s(t) = A\cos(2\pi f_0 t + \phi)e^{-\pi^2 \frac{(t-\tau_0)^2}{\Delta\tau^2}} \tag{3.17}$$

or

$$s(t) = A\sin(2\pi f_0 t + \phi)e^{-\pi^2 \frac{(t-\tau_0)^2}{\Delta\tau^2}} \tag{3.18}$$

where A is the relative amplitude, f_0 is the centre frequency, τ_0 is the centroid of the signal, $\Delta\tau$ is the rms duration of the signal and ϕ is the phase shift.

The waveform and spectrum of a simulated dolphin click using Equation 3.17 is shown in Figure 3.44. The simulated dolphin click has a duration of approximately 45 μs and a peak frequency of 125 kHz. This peak frequency corresponds to a resonance bubble radius of approximately 24 μm. Bubbles with radii 10, 25, 100,500, 1000 and 5000 will be driven by this simulated click with a peak source level of 100 kPa (220 dB re 1 μPa @ 1 m).

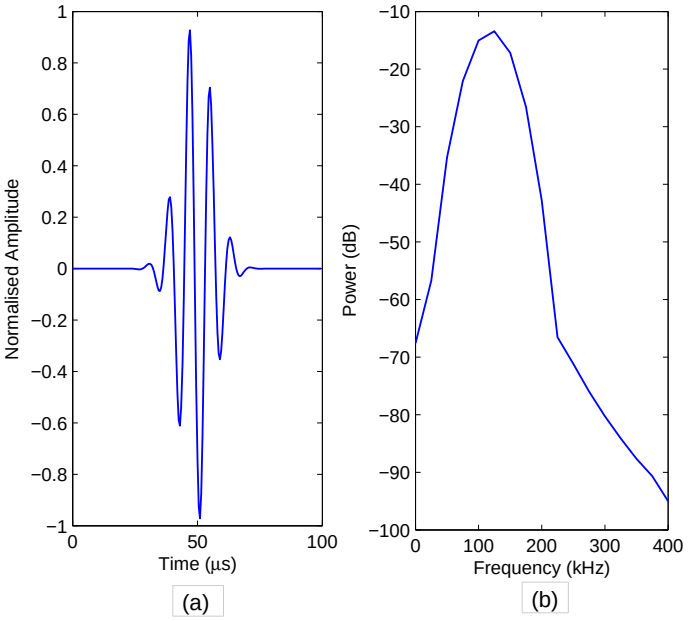

FIGURE 3.44: Simulated dolphin click (a) waveform; (b) spectrum (from Au (1993) [17]).

Although the sound pressure amplitude of the simulated dolphin click is much higher compared to the simulated porpoise chirps used earlier, the sound source was still chosen to be at 2 m from the centre of the bubble cloud. This would ensure high nonlinearities from bubble scatters.

3.6.1 Single bubble response

The backscatter pressure amplitude response from a single bubble of air in water with radius 10, 25, 100, 500, 1000 and 5000 μm driven by the simulated dolphin click given in Figure 3.44 is discussed here.

From the bubble scatter waveform shown in Figure 3.45, it can be observed that bubbles with a radius of 10 and 25 μm scatter nonlinearly. The frequency response plots shown in Figure 3.46 reveal more interesting observations with regard to nonlinear scatterers. The frequency response of bubbles with a radius of 10 μm shows that harmonic dispersion is not clearly present and inverted pulses scatter different frequencies. In addition, the backscatter from both positive and negative driving pulses has a resonance peak at 280 kHz. For bubbles with a radius of 25 μm, multiple harmonic peaks are observed in the frequency response. They however do not all occur at integer multiples of the driving frequency. This could be accounted for because of the very high source levels of the driving pulse which caused the shifting of frequency in the harmonic peaks.

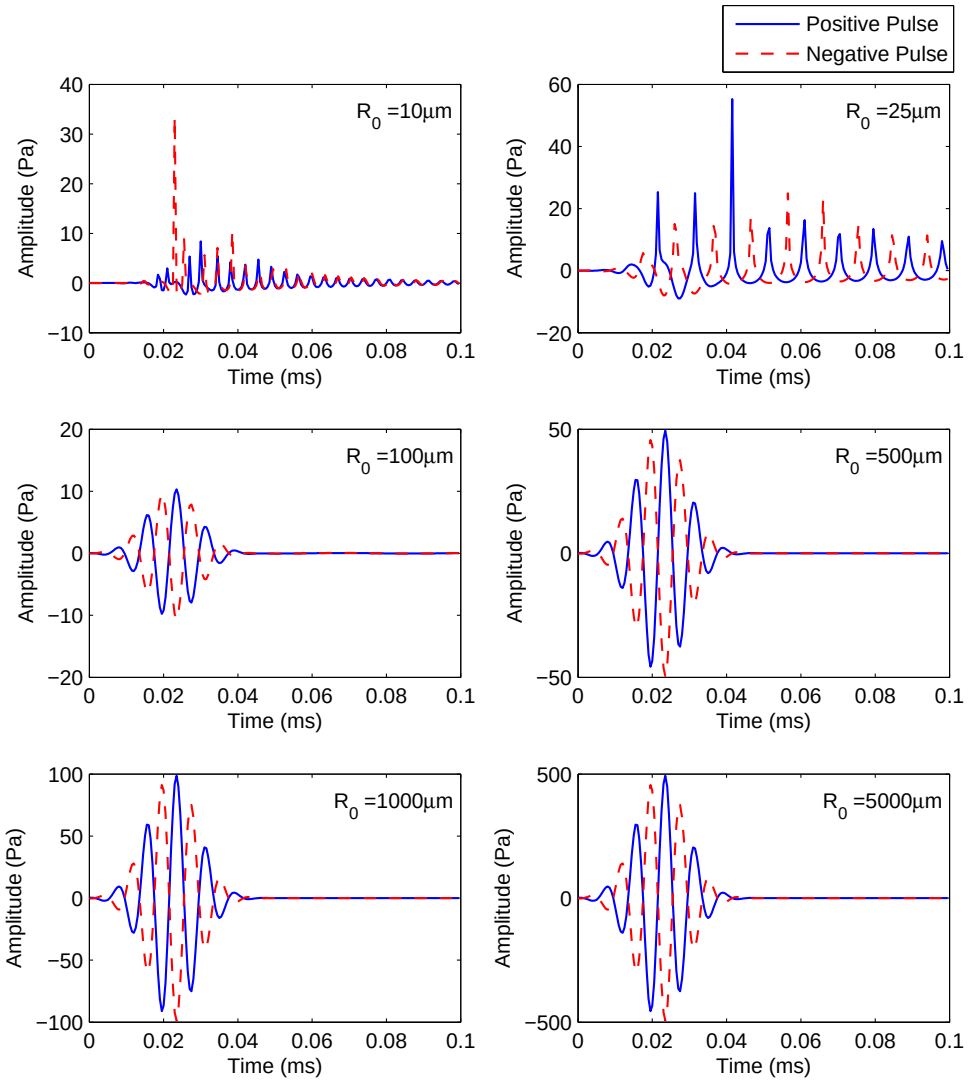

FIGURE 3.45: [Waveforms illustrating the backscatter from bubbles with radii 10, 50, 100, 500, 1000 and 5000 μm, when driven by a positive and negative simulated dolphin click at 100 kPa.

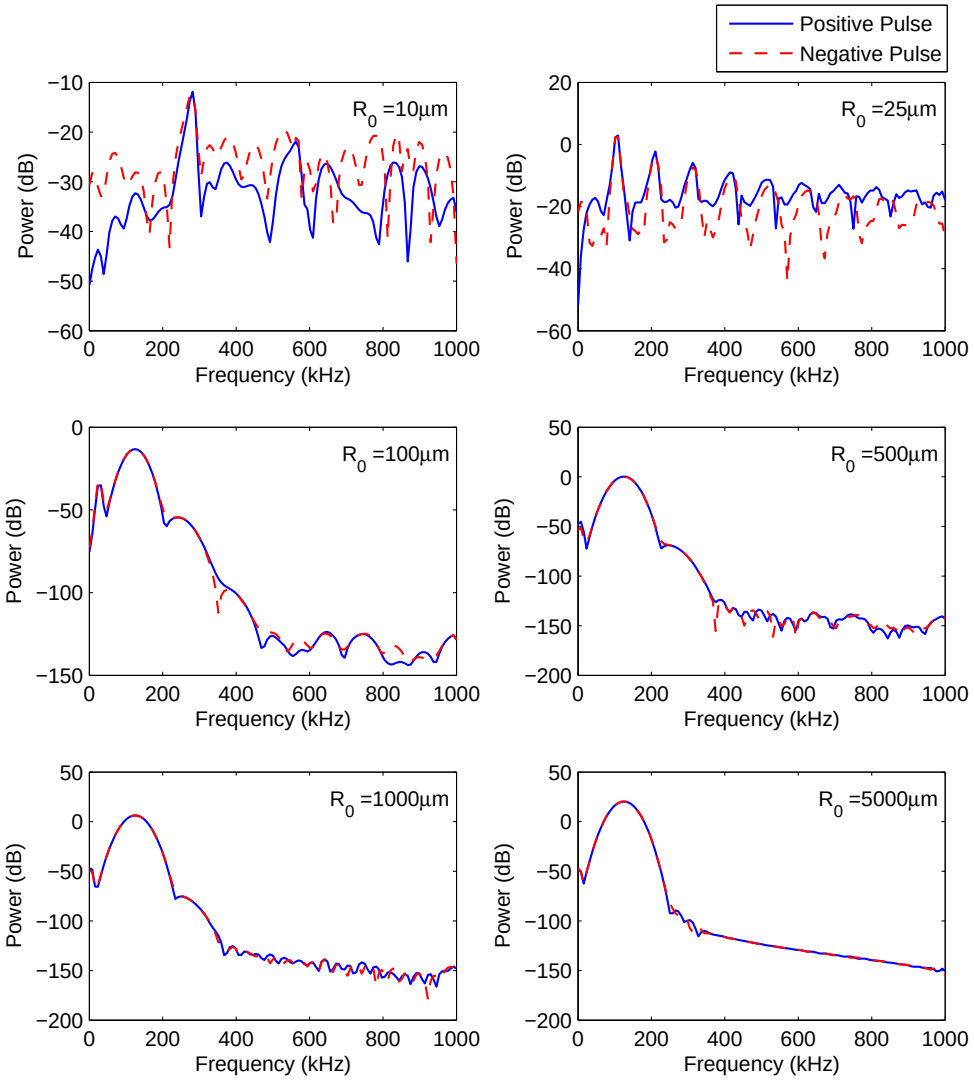

FIGURE 3.46: Frequency response plots illustrating the backscatter from bubbles with radii 10, 50, 100, 500, 1000 and 5000 μm, when driven by a positive and negative simulated dolphin click at 100 kPa.

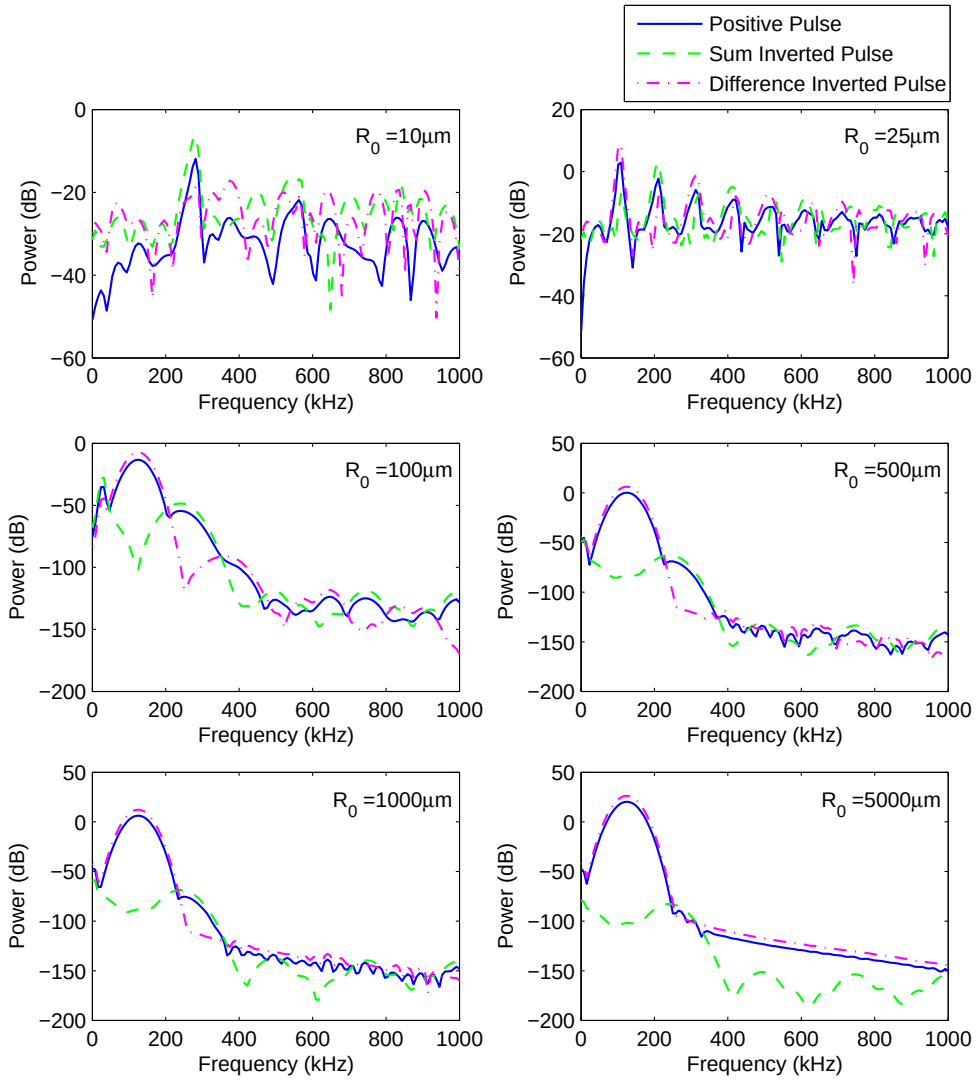

FIGURE 3.47: Frequency response plots illustrating the summation and subtraction of backscatter from bubbles with radii 10, 50, 100, 500, 1000 and 5000 μm, when driven by a positive and negative simulated dolphin click at 100 kPa.

The pulse inversion output of bubbles driven by a simulated dolphin click is given in Figure 3.47. As mentioned earlier, the frequency response from positive and negative pulses in the 10 μm bubble are different, thus the performance of harmonic suppression and enhancement is affected. Consider the result for the 10 μm bubble: it is not easy to make any useful observations due to the absence of harmonics. For the 25 μm bubble, there is some evidence of harmonic enhancement

and suppression but it becomes less obvious in the higher order harmonics. These observations might have been attributed to the short pulse length and high source levels.

The contribution of highly nonlinear responses from bubbles with radii 10 and 25 μm (which makes up a high percentage of bubbles in a real experimental measurement of bubble cloud distribution in the surf zone) sets up favourable conditions for the TWIPS approach. The response from a bubble cloud driven by a simulated dolphin click will be discussed in the next section.

3.6.2 Cloud response

The bubble cloud population distribution used for this simulation is the same as the one used in the simulation for porpoise chirps for the same reasons due to the similarity in centre frequency of the source signal. Although the driving sound pressure level involved in this simulation is much higher compare to the one used previously, the distance of the sound source is still fixed at 2 m from the centre of the bubble cloud. The target strength for the linear target is chosen to be -15 dB such that it would be just barely detectable in the cloud when observed from the waterfall plots. A target strength that is too low will just give zero detection rates for all or most of the processing methods while a target strength that is too high will give 100 % detection in all or most of the processing methods, which will not be useful either.

Figures 3.49 to 3.53 shows the waterfall plots of the various signal processing methods applied to the bubble cloud backscatter when driven by a simulated dolphin click. It can be observed that bandpass filtering gives the best contrast enhancement. This is followed by both TWIPS1a and TWIPS1b, where both seem to perform equally well. Cross correlation does not perform as well as in the previous examples and it has a problem with suppressing the scatter from bubbles when observed from its waterfall plot. The basic averaging and smoothing method and standard sonar processing totally gives no contrast in this case.

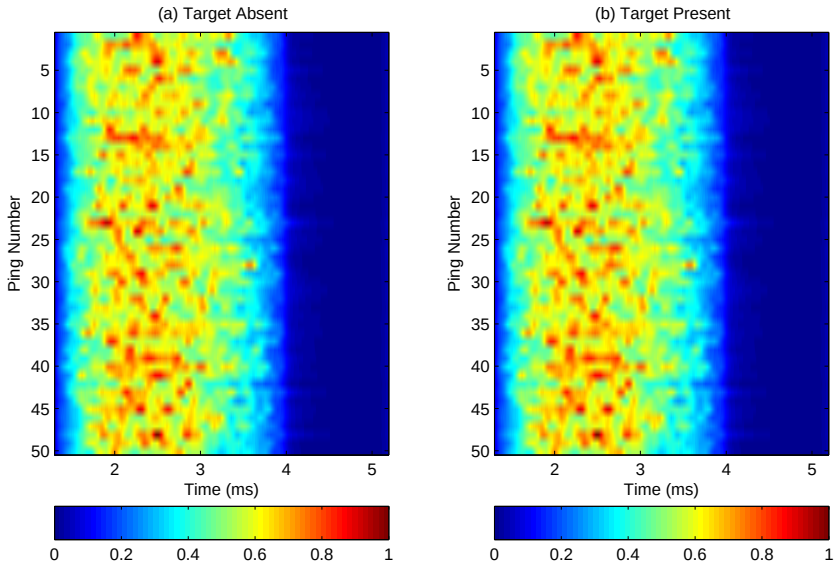

FIGURE 3.48: Waterfall plot of bubble cloud backscatter from a simulated dolphin click at 10 kPa using averaging and smoothing when a target is (a) absent; (b) present (TS = -15 dB).

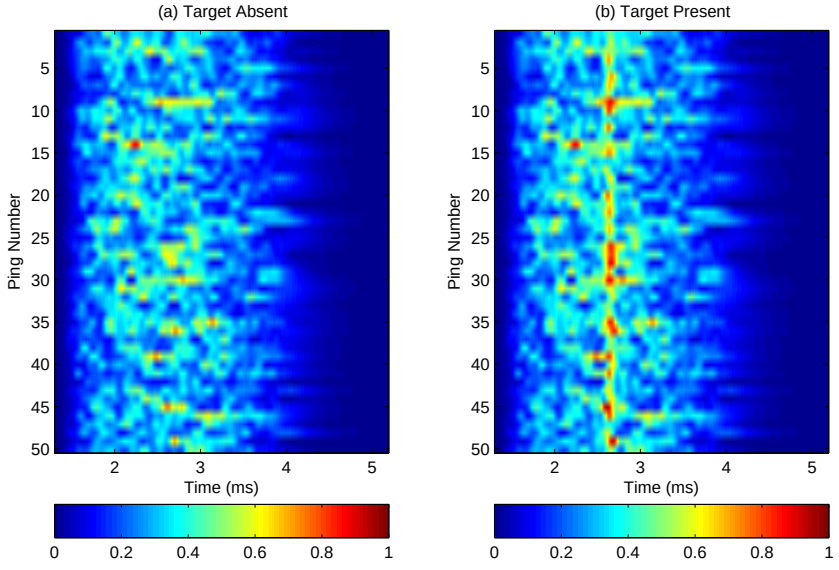

FIGURE 3.49: Waterfall plot of bubble cloud backscatter from a simulated dolphin click at 10 kPa using bandpass filtering when a target is (a) absent; (b) present (TS = -15 dB).

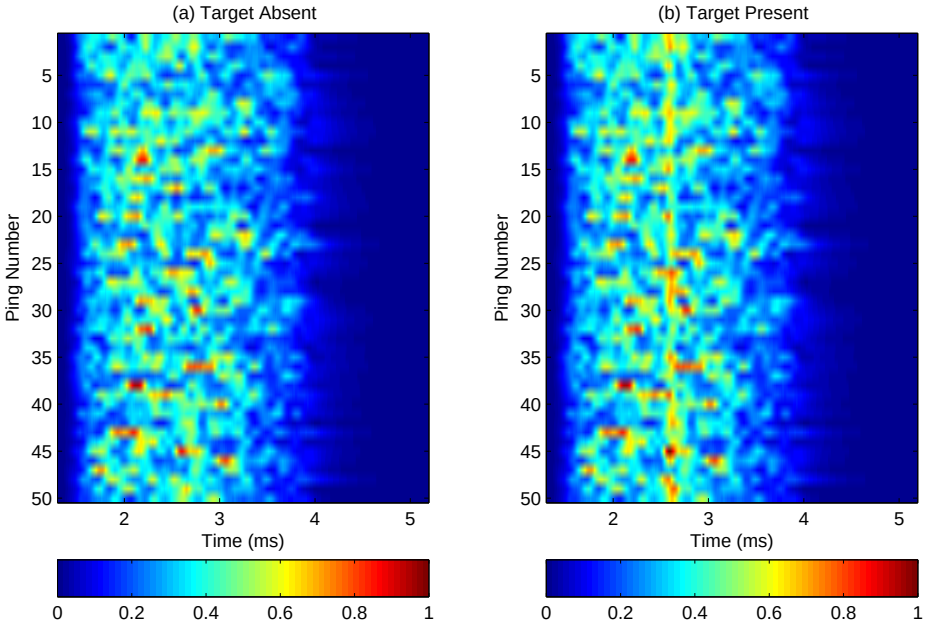

FIGURE 3.50: Waterfall plot of bubble cloud backscatter from a simulated dolphin click at 10 kPa using cross correlation when a target is (a) absent; (b) present (TS = -15 dB).

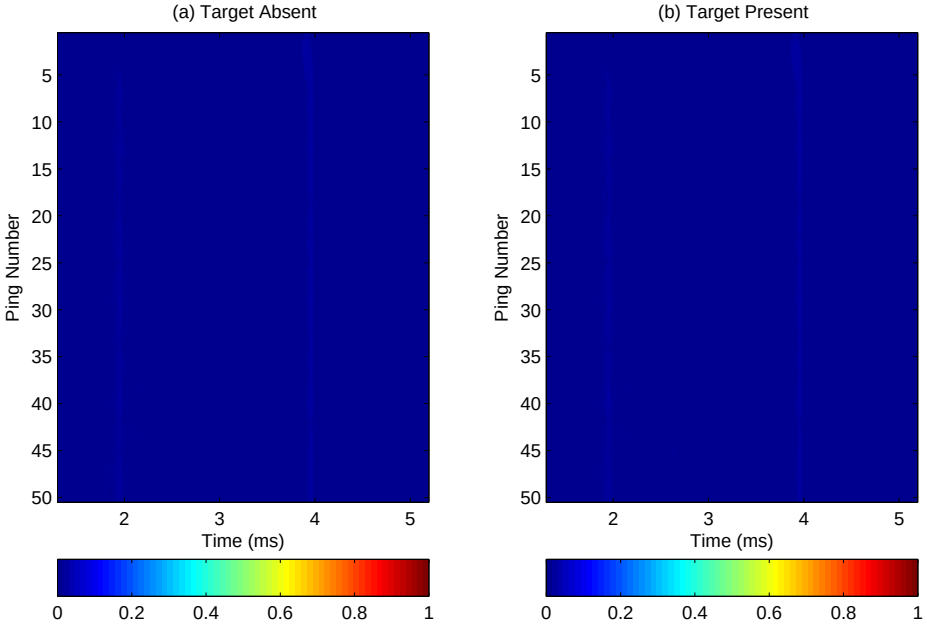

FIGURE 3.51: Waterfall plot of bubble cloud backscatter from a simulated dolphin click at 10 kPa using standard sonar processing when a target is (a) absent; (b) present (TS = -15 dB).

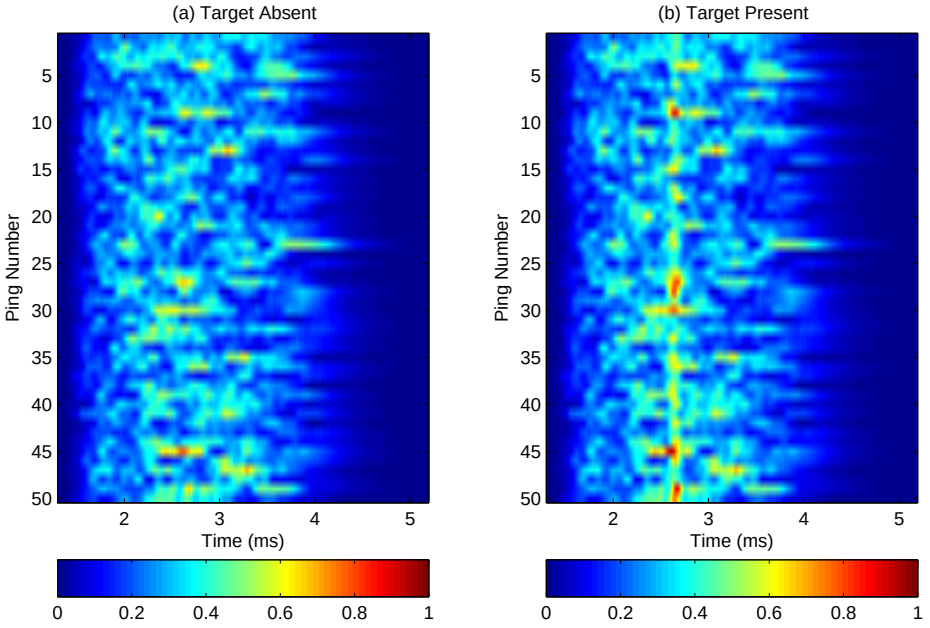

FIGURE 3.52: Waterfall plot of bubble cloud backscatter from a simulated dolphin click at 10 kPa using TWIPS1a when a target is (a) absent; (b) present (TS = -15 dB).

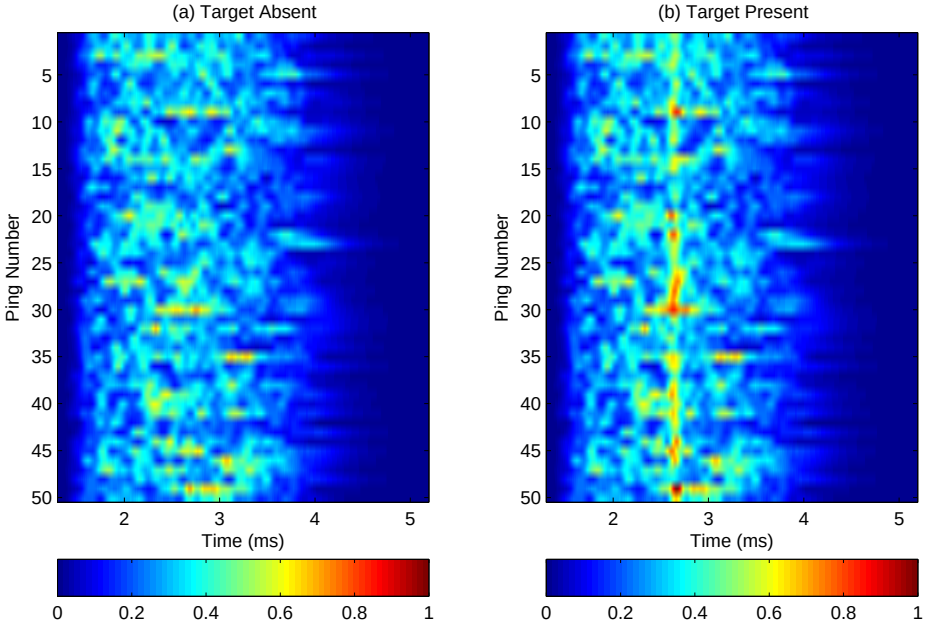

FIGURE 3.53: Waterfall plot of bubble cloud backscatter from a simulated dolphin click at 10 kPa using TWIPS1b when a target is (a) absent; (b) present (TS = -15 dB).

A comparison of SNR among these methods suggests the same results as the waterfall plots. The order of performance from best to worst based on SNR is bandpass filtering, TWIPS1b, TWIPS1a, cross correlation, standard sonar processing and averaging and smoothing.

TABLE 3.6: Comparison of SNR for different processing methods - simulated dolphin click at 100 kPa.

Signal processing	SNR
Averaging and smoothing	0.008
Bandpass filtering	0.122
Cross correlation	0.064
Standard sonar processing	0.026
TWIPS1a	0.073
TWIPS1b	0.094

The ROC plot is shown in Figure 3.54. Bandpass filtering method performs best and is significantly better than all the other methods. The waterfall plots for both TWIPS1a and TWIPS1b give few clues on whether one outperforms another and whether this is significant. However, the ROC plot provides this missing information by showing that TWIPS1b significantly outperforms TWIPS1a. The ROC curve for both cross correlation and standard sonar processing lies fairly close to the diagonal of uncertainty while the basic averaging and smoothing method gives a convex ROC curve. This indicates that their performances are unreliable.

In this section, it is shown that simulated dolphin click provides a sound pressure amplitude sufficient to drive bubbles into highly nonlinear oscillations. In addition, with the centre frequency of the click signal corresponding to a resonance bubble size that dominates in the bubble cloud population distribution, the scatter from the bubble cloud becomes highly nonlinear too. This renders some of the

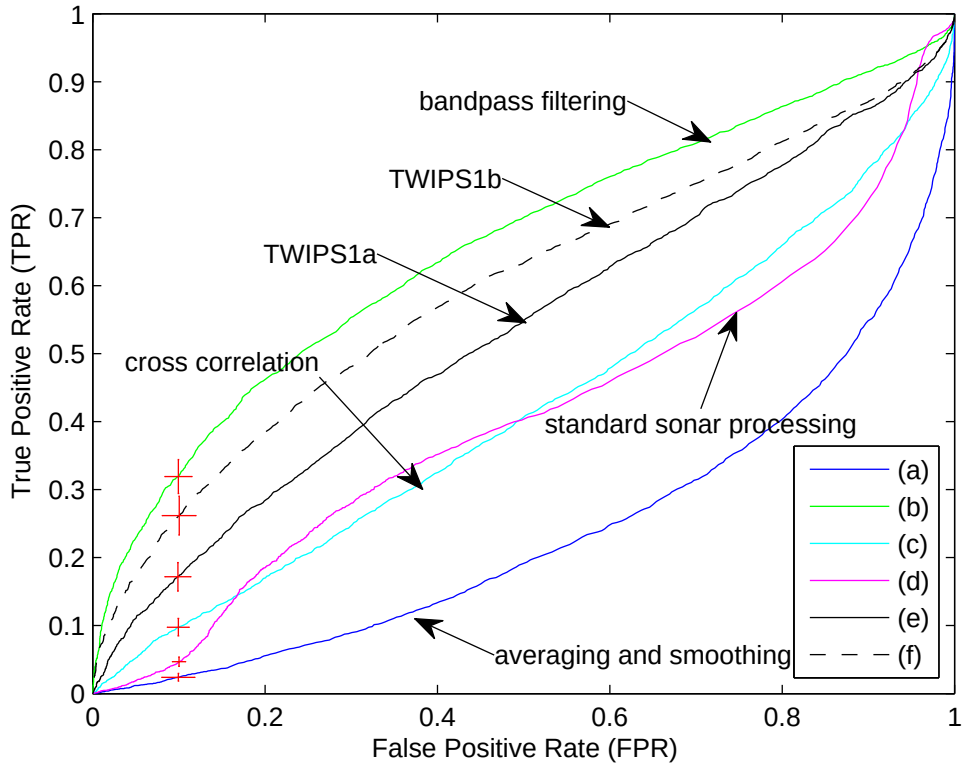

FIGURE 3.54: Simulated dolphin click at 100 kPa - Mean ROC curve with 95% CI (n = 50) at 0.1 FPR for (a) Averaging and smoothing; (b) Bandpass filtering; (c) Cross correlation; (d) Standard sonar processing; (e) TWIPS1a; (f) TWIPS1b.

methods discussed no longer as useful as they were in other examples where linear scatting dominated.

3.7 Simulation summary

So far, it seems that the original TWIPS1 method (TWIPS1a) proposed by Leighton and co-workers has never emerged as the best performing method in all the simulations discussed although it has always performed better than standard sonar processing in examples where the bubble cloud response was highly nonlinear.

From a summary of SNR comparison on the different signal processing methods using different driving pulses given in Table 3.7, it can been seen that there is a noticeable improvement in detection performance across all signal types when switching from TWIPS1a to TWIPS1b.

TABLE 3.7: Summary of SNR comparison on different processing methods using different driving pulse.

Signal processing method	6 kHz pulse (60 kPa)	Porpoise chirp (316 Pa)	Porpoise chirp (10 kPa)	Dolphin click (100 kPa)
Averaging and smoothing	0.250	0.089	0.093	0.008
Bandpass filtering	0.400	0.080	0.087	0.122
Cross correlation	0.357	0.187	0.200	0.064
Standard sonar processing	0.251	0.060	0.060	0.026
TWIPS1a	0.222	0.036	0.046	0.073
TWIPS1b	0.394	0.079	0.087	0.094

In cases with high nonlinearities generated in the bubble cloud (6 kHz pulse and simulated dolphin click), the bandpass filtering method gives the highest SNR. On the other hand, in the other examples with low amplitude driving pulse which generated linear or weakly nonlinear responses in the bubble cloud (simulated porpoise chirp), the cross correlation methods gives the highest SNR. In fact the SNR is two times more than the next best performing method in the linear case.

Comparing the performance between the 6 kHz pulse and simulated dolphin click examples based on their ROC curves, it is observed that the 6 kHz pulse gives an overall better performance across all the different signal processing methods. The detection rates for a 10 % error are much higher for the 6 kHz example despite the simulated dolphin click having a higher source level (100 kPa vs 60 kPa). This could be accounted for because of the difference in the centre frequency and pulse duration between these two signals. The 6 kHz pulse having a much lower centre

frequency, effectively drives a much larger population of bubbles nonlinearly (from 500 μm and below). On the other hand, the simulated dolphin click with a centre frequency of 125 kHz, drives a small population of bubbles in the cloud (25 μm and below) into nonlinear pulsations. With the 6 kHz pulse being able to generate nonlinearities on a larger population of bubbles in the bubble cloud, more of these non-linear components can be removed thus improving the signal to noise ratio.

Proof of concept will be discussed in the next chapter where experiments were conducted on a modified setup that is different from the simulated model.

Chapter 4

Experiment

4.1 Experimental setup

In the numerical simulations discussed in Chapter 3, the structure of the bubble cloud and its distribution were defined. In addition, the void fraction of the simulated cloud was assumed to be low. However, this is generally not the case for actual experiments conducted in a laboratory tank setting where bubble clouds do not have a definite shape. Moreover, the generation of a controlled and precise bubble size distribution with a low void fraction is difficult. It is possible to characterise the size of bubbles in a cloud and measure the void fraction experimentally, but these measurements have been excluded because of complexity in experiment design and the lack of specialized equipment for this task. Nevertheless, within the stated limits, the reliability of results obtained from the experiments was not compromised. TWIPS processing requires bubbles to be driven nonlinearly, hence prior knowledge of bubble size distribution would be helpful in determining the

most suitable excitation frequency. In the case of this experiment, it would be sufficient to show that the excitation frequency and amplitude used was able to produce nonlinearities in the backscatter which could be easily measured.

All the experiments discussed here were conducted in a rigid tank measuring 2 m long, 1 m wide and 0.8 m deep. The tank was filled with seawater with a salinity of 35 parts per thousand (ppt). An air-filled plastic bottle was used as a linear target and was placed along the centre axis of the main lobe of the acoustic driving source. The bubble generator consisted of a water pump which is modified such that air is entrained into an impeller. An inline valve restricted the water inlet to the pump. The air hose was connected via a valve to an air pump that maintained a slight positive pressure on the air supply. The generator could provide a variety of different bubble cloud populations depending on the relative settings of the air/water valves. The target when present was placed just above, and slightly behind the bubble generator such that bubbles enveloped the front surface of the target.

The driving pulse was produced by an echosounder (Odom Hydrographics Systems Inc, Model: OTSBB33) with a centre frequency of 33 kHz and 3 dB beamwidth of 23°. The return backscatter signal was received by a broadband omnidirectional hydrophone (Reson, Model: TC4013) mounted directly infront of the echosounder.

A power amplifier (Brüel & Kjær, Model: Type 2713) was used to amplify the driving pulse. The power amplifier is able to provide a maximum voltage output of 100 V peak. This together with the transducer gain provided a maximum

source level of 179 dB re 1μPa @ 1 m. A data acquisition device from National Instruments (Model: NI-USB 6251) was connected to a laptop computer (Macbook, 2.26 GHz Intel Core 2 Duo processor, 4 GB 1066 MHz DDR3 SDRAM), to generate the transmit pulse and to digitise the received signal. The received signal was sampled at 500 kHz and the acquired data was post processed on a desktop computer (Dell Optiplex 780, 3.16 GHz Intel Core 2 Duo processor, 8 GB 1066 MHz DDR3 SDRAM) running MATLAB R2009b.

Before the actual experiment tests began, several preliminary tests were carried out to determine the geometry, and most importantly the range from the transducer to bubble cloud. Clearly the shorter the range, the greater the received level at the bubble cloud, and the more likely nonlinear oscillations would result. A distance of 0.6 meters was chosen, and the bubble generator, and eventually the target were placed there. Figure 4.1 shows a block diagram of the experiment setup.

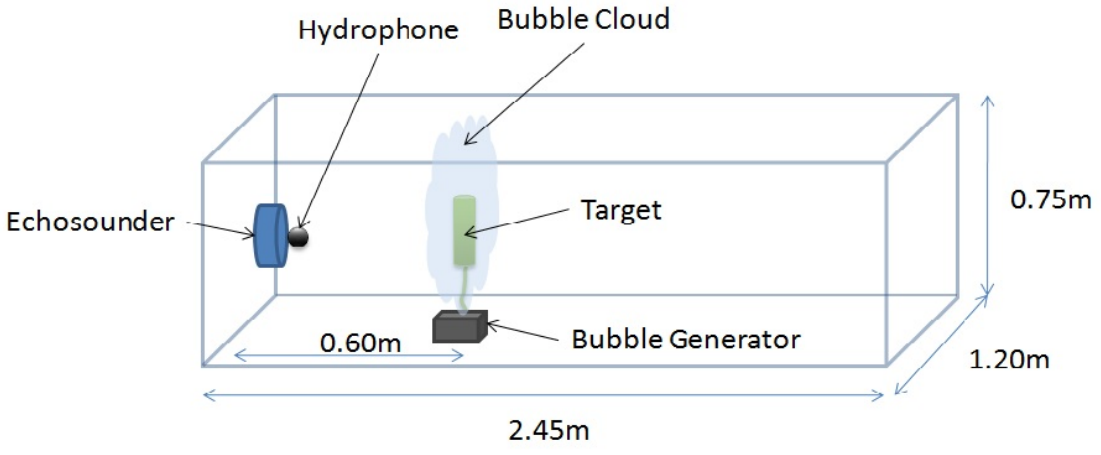

FIGURE 4.1: Block diagram showing the experiment setup.

The source level from the echosounder was measured at 0.6 m and shown in Figure 4.2. Another preliminary test was carried out to measure the target

strength, which was estimated to be -10 dB at 33 kHz.

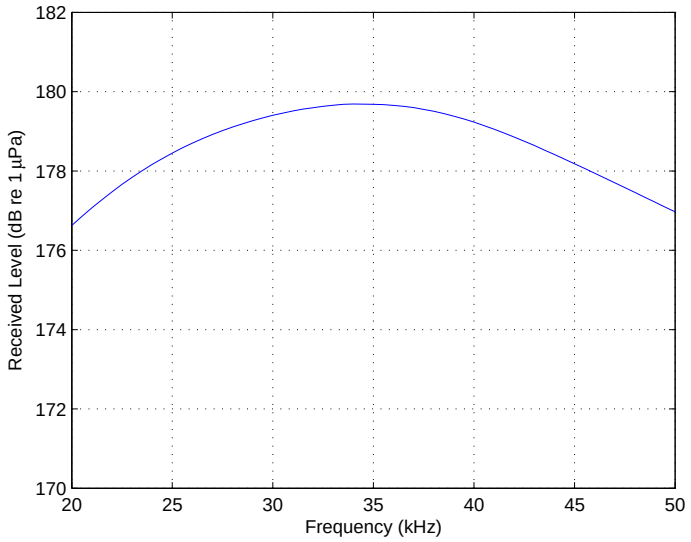

FIGURE 4.2: Source level measured at position occupied by target.

The driving pulse was created by applying a Hanning window on a 37 kHz sine waveform with a duration of 50 μs. The centre frequency of the driving signal was chosen to be 37 kHz despite the transducer having a resonance frequency of 33 kHz. This was because a centre frequency of 37 kHz gave the highest pressure amplitude when measured from the transducer. When this signal was sent to the transducer, it properties were modified due to the nature of the transducer. The waveform of the signal transmitted by the transducer is shown in Figure 4.3.

As mentioned earlier, the distribution of bubble size and void fraction in the bubble cloud could not be measured in the experiments conducted. For simplicity, it would be sufficient to show that the backscatter from the cloud exhibits a nonlinear response. This would then mean that the driving sound pressure level is sufficient and the driving frequency falls within the range of bubble resonance frequencies in the bubble cloud. The backscatter from the bubble cloud when

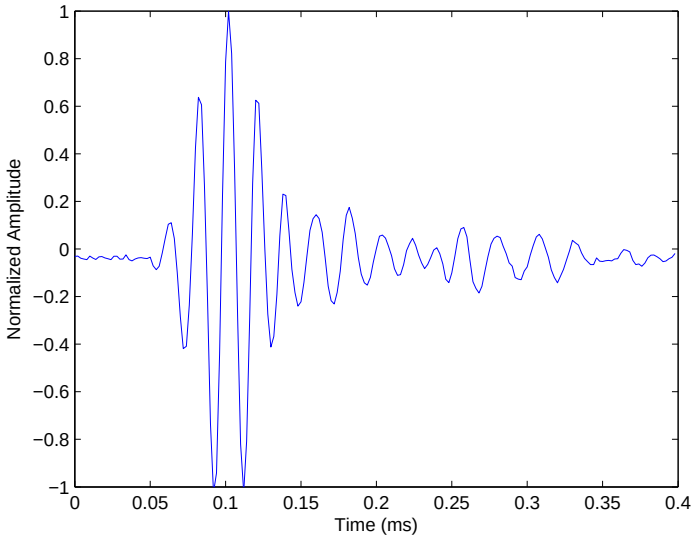

FIGURE 4.3: Waveform of the driving pulse used in the experiment.

driven by the defined pulse was measured and the air/water valves controlling the bubble cloud was adjusted until some nonlinearities were observed.

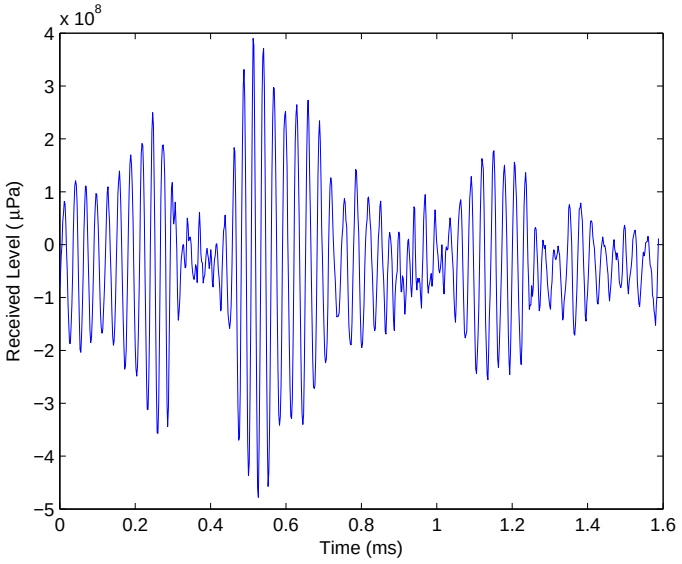

FIGURE 4.4: Waveform of the backscatter from bubble cloud used in the experiment.

Figures 4.4 and 4.5 show the waveform and frequency response of the bubble cloud driven by the 37 kHz pulse from the echosounder. It can be observed from

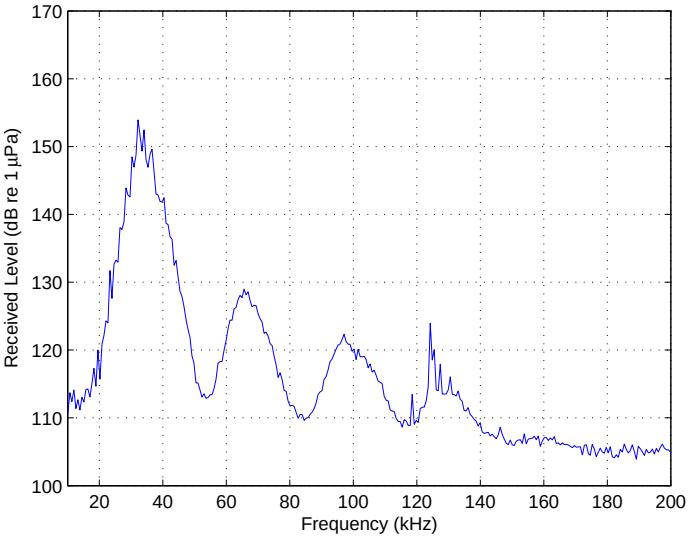

FIGURE 4.5: Frequency response of the bubble cloud used in the experiment.

the frequency response plot that weak nonlinearities were generated and this was the best that could be achieved with the available resources.

Earlier, there was a discussion on the effects of delay between the positive and negative driving pulse affecting the performance of TWIPS. To illustrate this effect, two experiments were conducted. The first experiment used a pair of inverted pulses with no time delay to ensure that bubbles have not move during this period. The second experiment introduced a 0.5 s delay between each inverted pulse during which bubbles would have moved during this period of time.

4.2 Experiment results - Bubble cloud response

Consider the description of the signal processing methods used in [14], where the backscatter from the positive and negative pulse were taken at the same time and the other processing methods uses an average of two positive pulses from different

instances in time. Two sets of data were collected in the first experiment, one with the bubble cloud alone and the other with a target in the bubble cloud. In each set, the bubble cloud (with/without target) was pinged with 100 pairs in inverted pulses. The duration between each positive and negative pulse was at a minimum which was limited by the hardware latency. The duration between each pair of inverted pulses was 0.5 s which was sufficiently long to allow bubbles to move. In the second experiment, two sets of data were again collected, one with the bubble cloud alone and the other with a target in the bubble cloud. In each set, the bubble cloud (with/without target) was pinged with 100 pairs in inverted pulses. In this experiment however, the duration between each positive and negative pulse was set to 0.5 s to provide a time delay sufficient to allow bubbles to move spatially with respect to the cloud.

The data collected from experiment 1 was post-processed to produce the waterfall plots in Figure 4.6 to 4.10, whereas the data from experiment 2 was used to produce the waterfall plot for TWIPS1b as shown in Figure 4.11.

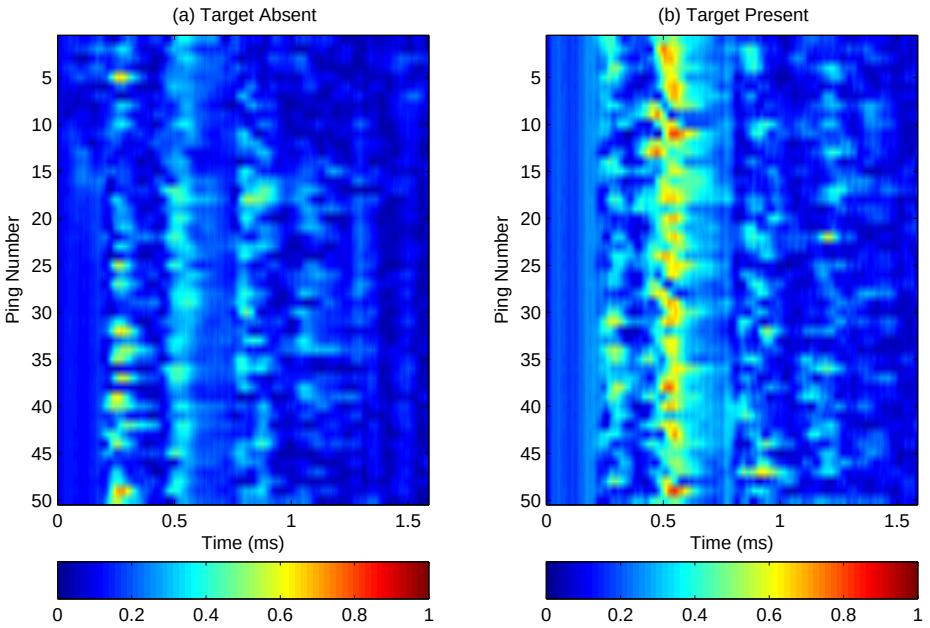

FIGURE 4.6: Waterfall plot of bubble cloud backscatter from experiment driving pulse using averaging and smoothing when a target is (a) absent; (b) present.

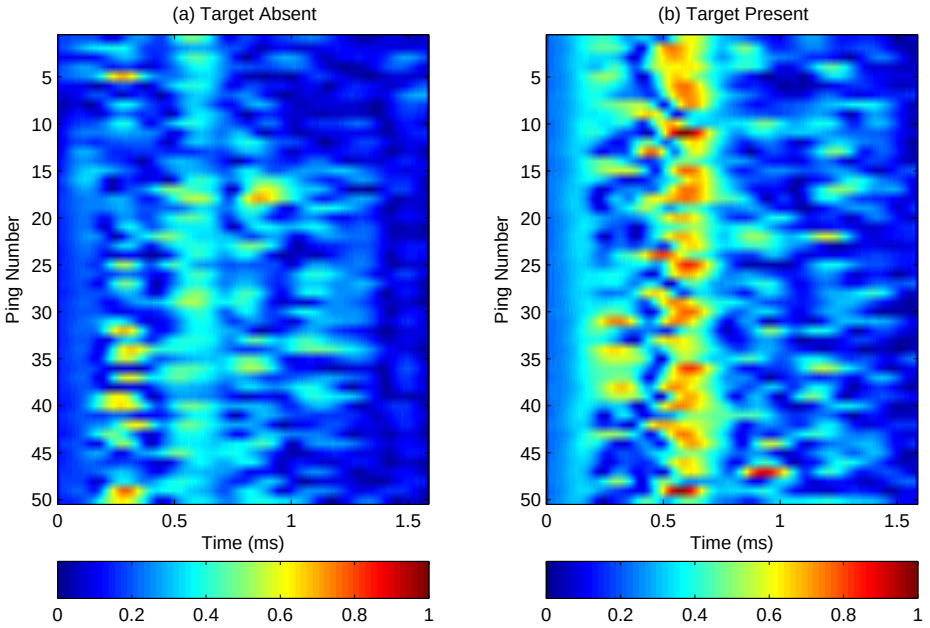

FIGURE 4.7: Waterfall plot of bubble cloud backscatter from experiment driving pulse using bandpass filtering when a target is (a) absent; (b) present.

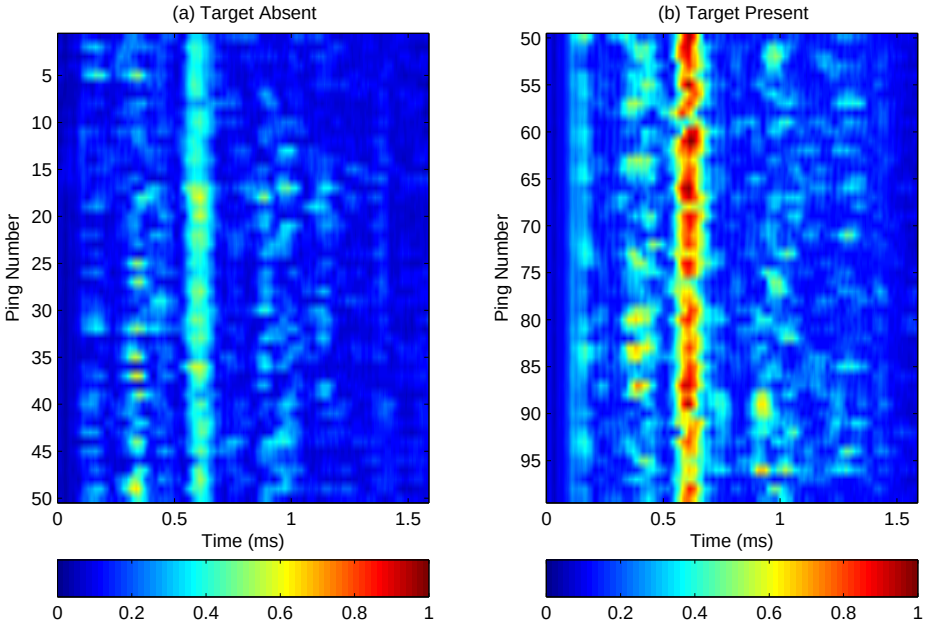

FIGURE 4.8: Waterfall plot of bubble cloud backscatter from experiment driving pulse using cross correlation when a target is (a) absent; (b) present.

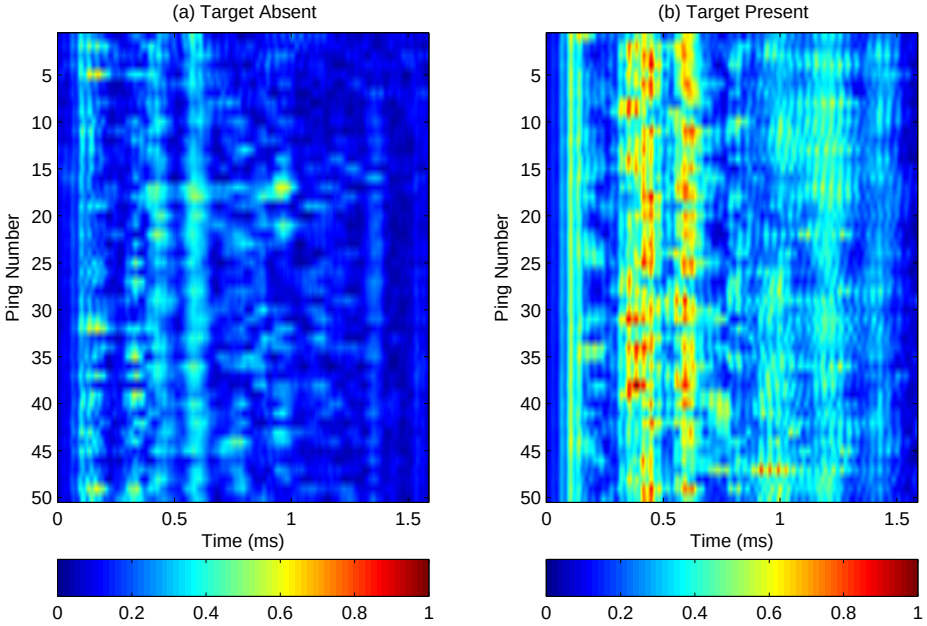

FIGURE 4.9: Waterfall plot of bubble cloud backscatter from experiment driving pulse using standard sonar processing when a target is (a) absent; (b) present.

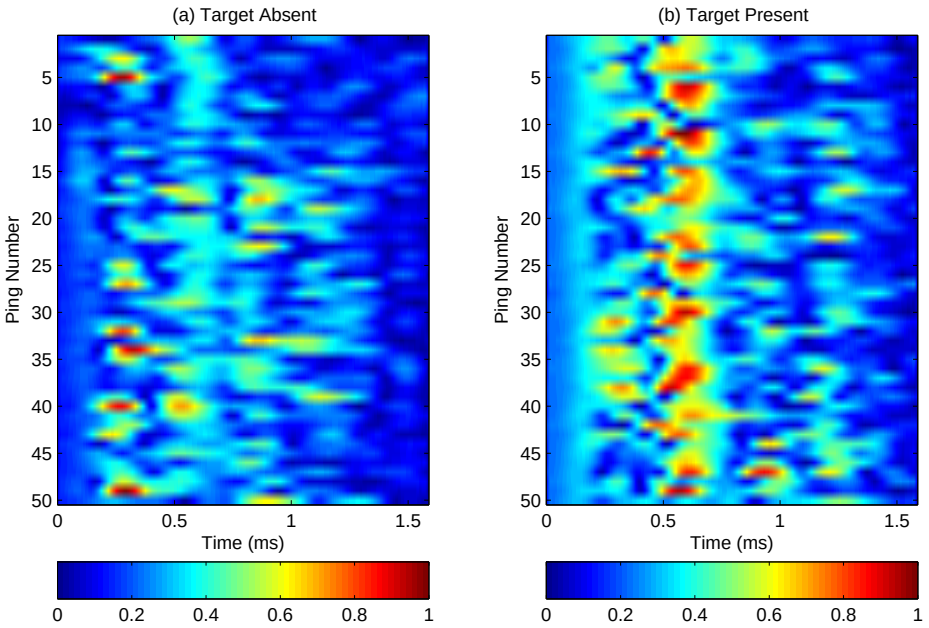

FIGURE 4.10: Waterfall plot of bubble cloud backscatter from experiment driving pulse using TWIPS1a when a target is (a) absent; (b) present.

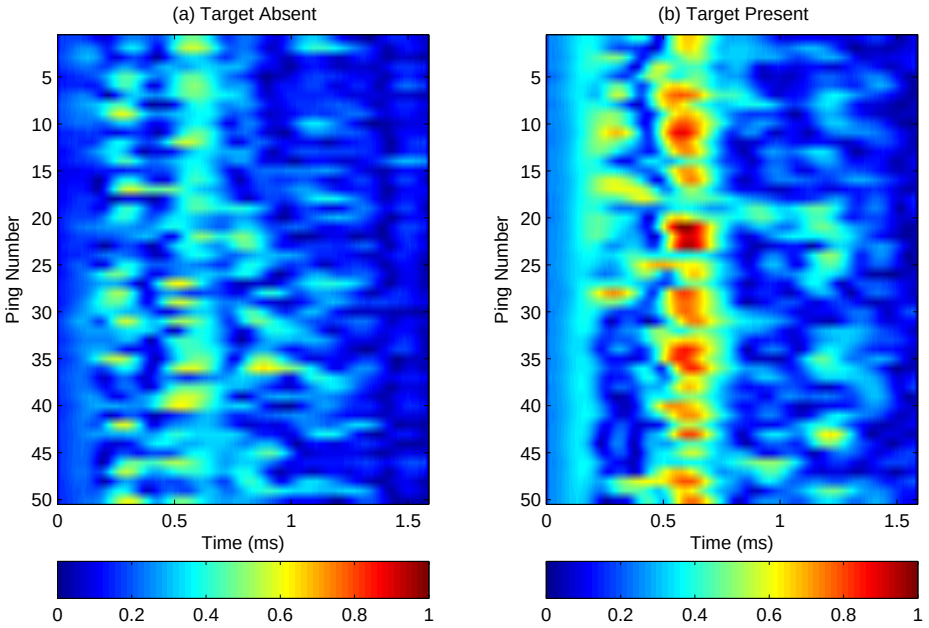

FIGURE 4.11: Waterfall plot of bubble cloud backscatter from experiment driving pulse using TWIPS1b when a target is (a) absent; (b) present.

A comparison between the waterfall plots shows that the cross correlation method gives the best target contrast. All the other methods except standard sonar processing perform relatively well from one another.

A comparison of SNR is provided in Table 4.1. It can be observed that cross correlation outperforms the other methods. Averaging and smoothing give the next best SNR followed by bandpass filtering and TWIPS1b which are almost equally good or bad. TWIPS1a has the second lowest SNR followed by standard sonar processing.

Table 4.1: Comparison of SNR for different processing methods applied on experiment data.

Signal processing	SNR
Averaging and smoothing	0.898
Bandpass filtering	0.815
Cross correlation	1.303
Standard sonar processing	0.171
TWIPS1a	0.657
TWIPS1b	0.817

The ROC curves in Figure 4.12 show that the cross correlation method significantly outperforms all the other methods. Basic averaging and smoothing, bandpass filtering and both TWIPS1a and TWIPS1b are on par with one another except that TWIPS1b performs slightly better for lower FPRs. Standard sonar processing had difficulty suppressing the scatter from the bubble cloud thus it performed very poorly as shown in the ROC plot.

Thus far, its has been observed that even with the simplest experimental setting, the experiment results do agree with the results from simulation, whereby TWIPS1 does outperform standard sonar processing but fails to perform well

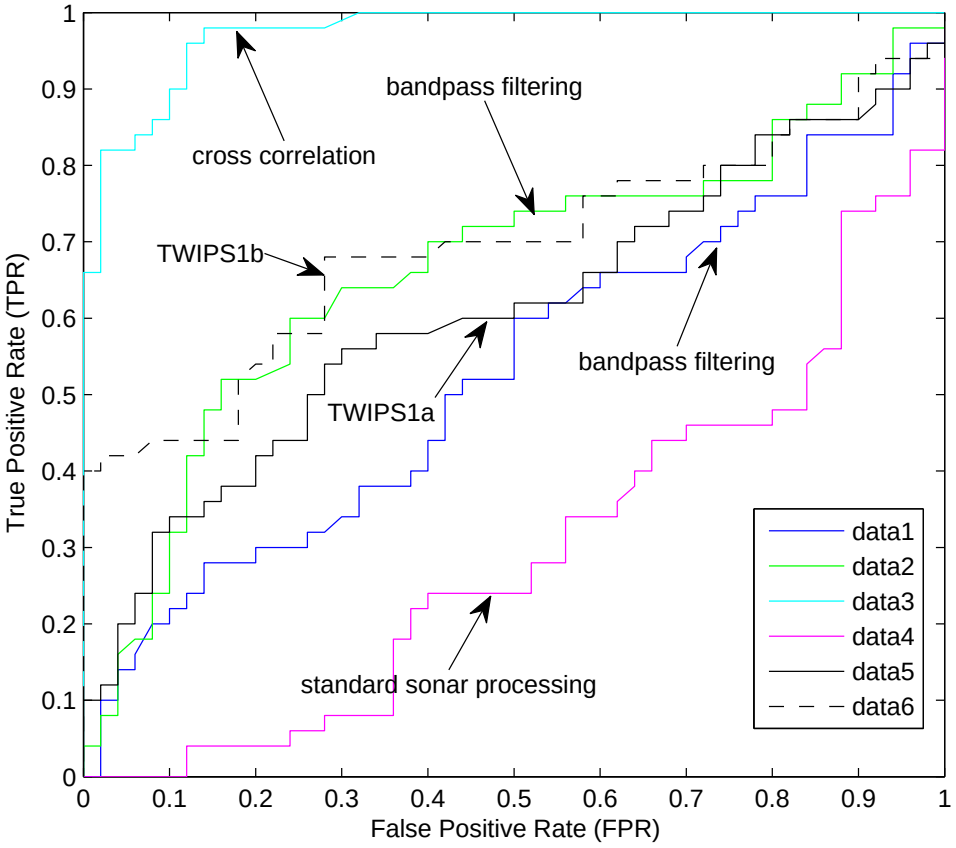

FIGURE 4.12: Experiment data - ROC curve for (a) Averaging and smoothing; (b) Bandpass filtering; (c) Cross correlation; (d) Standard sonar processing; (e) TWIPS1a; (f) TWIPS1b.

against bandpass filtering or cross correlation method. Conclusions drawn from both the simulations and experiments will be provided in the following chapter.

Chapter 5

Conclusion and Future Work

Despite much effort to reproduce the work by Leighton and co-workers, the simulation results obtained here seem somewhat disappointing. This is not because of the fact that the results were incorrect, but rather because of the much discussion on TWIPS and its benefits over their version of 'standard sonar processing' method, when it turns out that a simple bandpass filter or cross correlation method may work equally well in the simulations. Efforts were made to contact the authors for clarification in some of their implementations, where they were extremely helpful and enthusiastic initially. At one stage of the project, it was found that there could be some discrepancies in the calculation of the bubble population distribution. Through correspondence with one of the authors of the paper, it seems like it is most likely that they made a mistake in some of the statements they made. It was also observed that the authors did not include comparisons of TWIPS against other signal processing methods in any of their reports or articles. There was a

mention of on-going studies to investigate the ROC curve characteristics of TWIPS in [11], but there have not been any known reports to date.

The experiment was very challenging to conduct due to the lack of specialised equipment and a suitable experiment site. Moreover, the design of a well controlled experiment requiring the characterisation of bubble population distribution and measurements of void fraction was complicated and way beyond the scope and requirements for this course. Nevertheless, some preliminary experiments were still conducted using available resources.

The data collected from experiments produced results that somewhat agree with simulation results presented in this research, in which TWIPS1 performed better than 'standard sonar processing' but not against the standard cross correlation method. Of course it may be argued that the bubble cloud size distribution and void fraction were not properly characterised and the acoustic source levels used were insufficient to generate the high nonlinearities required. But these were limitations that could not be easily resolved with the resources available.

There is little doubt that TWIPS does work experimentally based on various reports of experimental trials on TWIPS [11, 14]. However, these trials were all made in a controlled laboratory setting. The task would probably be more representative and challenging in real sea trials.

Unfortunately this research did not have the luxury of working with real dolphin research subjects, as this would have been the best test of whether these animals do exploit nonlinearities for target detection in bubble populated water.

If a controlled bubble population distribution in the form of a bubble screen or bubble cloud could be generated, it would be interesting to see if dolphins change the centre frequency and amplitude of their echolocation pulses to match that of the resonance bubble frequency. More importantly, the backscatter from the bubble cluster could be measured to see if nonlinearities were indeed generated. The various signal processing techniques and analysis methods discussed here could then be used with this data to compare which method(s) might be most useful. There can also be another interesting outcome whereby none of the proposed signal processing methods described here work, and yet the dolphin still manages to somehow detect a target hidden in or behind a bubble cloud/screen. It might then suggest that there is a possibility of dolphins using a much superior processing method yet unknown to us which needs further investigation.

To conclude, the research here is not an attempt to disprove any of the claims by the inventors of TWIPS, but rather to close up missing links that they might have left out. It is hoped that the studies described here offer alternatives methods for processing sonar signals and provide statistical methods for the analysis of their performances. This would then help in the development of man-made sonar systems employing bio-mimetic signals that perform effectively in the littoral zone.

Appendix A

Formulating the modified Herring-Keller equation

The formulation of the Herring-Keller equation was described in detail by Hoff(2001) [43]. A summary of this derivation is given here.

In deriving the equation of motion of a bubble, the Bernoulli equation is first combined with the linear wave equation to give a set of equations for the velocity potential at the bubble surface.

Bernoulli equation:

$$\frac{\partial \Phi}{\partial t} + \frac{1}{2}\left(\frac{\partial \Phi}{\partial r}\right)^2 + h = 0; \tag{A.1}$$

Linear wave equation:

$$\frac{\partial^2 \Phi}{\partial r^2} - \frac{1}{c^2}\frac{\partial^2 \Phi}{\partial t^2} = 0 \tag{A.2}$$

Speed of sound, c:

$$\left(\frac{\partial \rho}{\partial p}\right)_S = \frac{1}{c^2} = constant \tag{A.3}$$

Enthalpy, h:

$$h = \frac{p(r) - p_\infty}{p_\infty} \tag{A.4}$$

The expression for enthalpy in Equation A.4 is correct to the first order in 1/c and boundary conditions at the bubble surface $r = a(t)$ are given as:

$$p(a,t) = p_L(t) \tag{A.5}$$
$$\frac{\partial \Phi(a,t)}{\partial r} = u(a,t) = \dot{a}(t) \tag{A.6}$$

Eq. A.1 to A.6 are combined to obtain a new set of equations for the velocity potential at the bubble surface:

$$\frac{\partial \Phi}{\partial t} + \frac{1}{2}\dot{a}^2 + h = 0 \tag{A.7}$$
$$\frac{\partial^2 \Phi}{\partial r^2} - \frac{1}{c^2}\frac{\partial^2 \Phi}{\partial t^2} = 0 \tag{A.8}$$
$$\frac{\partial \Phi}{\partial r} = \ddot{a} \tag{A.9}$$

The general solution to the wave equation is given as:

$$\Phi(r,t) = \frac{f_1(t - r/c)}{r} + \frac{f_2(t + r/c)}{r} \tag{A.10}$$

where $f_1(x)$ and $f_2(x)$ are arbitrary functions.

Taking partial derivatives with time and radius,

$$\frac{\partial \Phi}{\partial t} = \frac{f_1'}{r} + \frac{f_2'}{r} \tag{A.11}$$
$$\frac{\partial \Phi}{\partial r} = -\frac{f_1'}{rc} - \frac{f_1}{r^2} + \frac{f_2'}{rc} - \frac{f_2}{r^2} \tag{A.12}$$

The partial derivatives are inserted into the Bernoulli equation (Eq. A.1) and replacing the velocity potential (Eq. A.9) gives:

$$c(f_1 + f_2) = aa^2\left(\frac{1}{2}\dot{a}^2 - ca + h\right) + 2af_2' \tag{A.13}$$

Differentiate with respect to time,

$$c\left(1-\frac{\dot{a}}{c}\right)\left(f_1'+f_2'\right) = ca\left(-2\dot{a}^2\left(1-\frac{1}{2}\frac{\dot{a}}{c}\right)-a\ddot{a}\left(1-\frac{\dot{a}}{c}\right)+2\frac{\dot{a}}{c}h+\frac{a}{c}\dot{h}\right)+ 2a\left(1+\frac{\dot{a}}{c}\right)f_2'' \tag{A.14}$$

The time derivatives of f1 and f2 are eliminated by using the equation:

$$\frac{f_1'+f_2'}{a}+\frac{1}{2}\dot{a}^2+h=0 \tag{A.15}$$

The equation of motion for the bubble surface is finally obtained after substituting for the time derivatives of f1 and f2:

$$a\ddot{a}\left(1-\frac{\dot{a}}{c}\right)+\frac{3}{2}\dot{a}^2\left(1-\frac{1}{3}\frac{\dot{a}}{c}\right)-h\left(1+\frac{\dot{a}}{c}\right)-\frac{a}{c}\dot{h}-\frac{2}{c}\left(1+\frac{\dot{a}}{c}\right)f_2''\left(t+\frac{a}{c}\right)=0 \tag{A.16}$$

The driving acoustic field is included by the term containing $f_2''(t+a/c)$ because $f_2(t+a/c)$ represents a converging spherical wave.

The driving field which is described by a velocity potential field, can be decomposed into spherical harmonics and spherical Bessel functions. Since bubble oscillation is purely radial, the zeroth term is the only term that interacts with this radial mode. The zeroth term is given as:

$$\Phi_{i0}(r,t)=\frac{f_2(t+r/c)+f_3(t-r/c)}{r} \tag{A.17}$$

The driving field has its potential in the bubble center where $r=0$. This would imply that $f_3=-f_2$ and the driving acoustic field is given as:

$$\Phi_{i0}(r,t)=\frac{f_2(t+r/c)-f_2(t-r/c)}{r} \tag{A.18}$$

As the bubble diameter is small compared to the wavelength of the driving pressure field, only small variations are allowed in the function f_2 over a distance equal to the bubble diameter. The variation of f_2 over the bubble diameter is

approximated as:

$$\frac{f_2(t+r/c)-f_2(t-r/c)}{a} \approx \frac{2}{c} f_2'(t) \tag{A.19}$$

If the driving acoustic field is treated linearly, then the driving pressure $p_i(a,t)$ at the bubble surface can be found from the velocity potential:

$$p_i(a,t) = -\rho \frac{\partial \Phi_{i0}}{\partial t}\Big|_{r=a} = -\frac{2\rho}{c} f_2''(t) \tag{A.20}$$

The above equation is substituted into the equation of motion given in Eq. A.16. The driving acoustic field Φ_{i0} will disappear at $r=\infty$, giving $p_\infty = p_0$. The final expression for the equation of motion for the bubble is given as:

$$a\ddot{a}\left(1-\frac{\dot{a}}{c}\right)+\frac{3\dot{a}^2}{2}\left(1-\frac{\dot{a}}{3c}\right)-\left(1+\frac{\dot{a}}{c}\right)\frac{1}{\rho}\left(p_L-p_0-p_i(t+\frac{a}{c})\right)+\frac{a}{\rho c}\frac{\partial p_L(t)}{\partial t}=0 \tag{A.21}$$

The pressure at the bubble surface p_L is given as:

$$p_L = \left(p_0+\frac{2\sigma}{a}\right)\left(\frac{a}{a_e}\right)^{3\kappa} - \frac{2\sigma}{a} - \frac{4\eta_L \dot{a}}{a} \tag{A.22}$$

Assuming that the liquid medium is incompressible, the pressure at a distance r from the bubble center is given by;

$$\left(\frac{p}{p_\infty}-1\right)\frac{p_\infty}{\rho} = \frac{a}{r}\left(\ddot{a}a+2\dot{a}^2\right) - \frac{\dot{a}^2}{2}\left(\frac{a}{r}\right)^4 \tag{A.23}$$

Numerical differentiation to find the bubble wall acceleration $\ddot{a}$ can easily become inaccurate and unstable, thus it is reformulated using the equation of motion:

$$\ddot{a}a + \frac{3}{2}\dot{a}^2 + \frac{p_\infty - p_L}{\rho} = 0 \tag{A.24}$$

Expressing the equation of motion in terms of $\ddot{a}$,

$$\ddot{a} = \frac{1}{a}\left(-\frac{3}{2}\dot{a}^2 - \frac{p_\infty - p_L}{\rho}\right) \tag{A.25}$$

The pressure radiated by the bubble can then be solved by substituting for $\ddot{a}$ to obtain:

$$p_s = p - p_\infty = \frac{a}{r}\left(\frac{1}{2}\rho\dot{a}^2 + p_L - p_\infty\right) - \rho\frac{\dot{a}^2 a^4}{2\dot{r}^4} \tag{A.26}$$

Appendix B

Receiver Operating Characteristic (ROC) Curves

Receiver Operating Characteristic (ROC) curves was developed in the 1950's where it was used for signal detection in radio signals contaminated by noise. It is a technique used generally for organising classifiers and visualisation of their performance. Other applications of ROC curves include medical decision making, machine learning and data mining.

In this research project, the ROC technique is used as a 2 class classifier (target present and target absent).Given a classifier (actual class) and instance (measured data), there are 4 possible outcomes. If an instance detects a target and the target is physically present, it is considered as a *true positive*; if the target is physically absent, it is considered as a *false positive*. If an instance doesn't detect a target and the target is physically absent, it is considered a *true negative*; if the target is physically present, it is considered a *false negative*. Given the set of classifiers and instances, a two-by-two confusion matrix (contingency table) can be created.

The following information can be obtained from the confusion matrix:

True Positive (TP) - Correct detection

True Negative (TN) - Correct rejection

False Positive (FP) - False alarm

False Negative (FN) - Miss

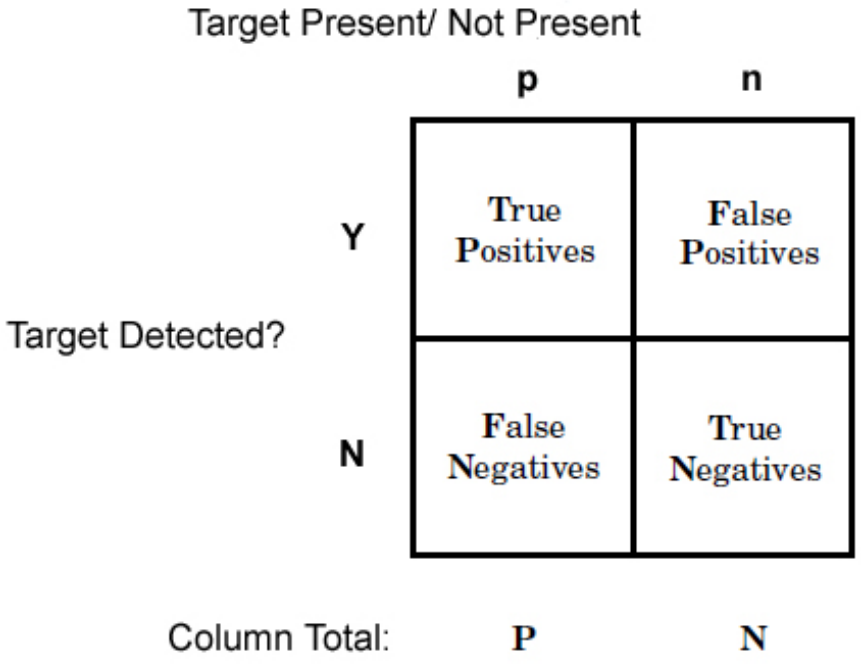

FIGURE B.1: Confusion Matrix

Sensitivity or True Positive Rate (TPR) - Correction detection rate

$$TPR = \frac{TP}{P} = \frac{TP}{TP + FN} \tag{B.1}$$

False Positive Rate (FPR) - False alarm rate

$$FPR = \frac{FP}{N} = \frac{FP}{Fp + TN} \tag{B.2}$$

Specificity or True Negative Rate (TNR)

$$Specificity = 1 - FPR \tag{B.3}$$

The ROC curve is a plot of True Positive Rate (y-axis) against False Positive Rate (x-axis) over a range of detection thresholds. In signal detection theory, an ideal receiver in the absence of interference will have a TPR of 1 and a FPR of 0 for the entire detection threshold range. However in practical situations this is not possible. A good detector aims to maximise the TPR while minimising the FPR. The diagonal line joining the points (0,0) and (1,1) is called the diagonal of uncertainty where it means that the outcome is a random guess.

To compare the performance between ROC curves, one needs to apply a measure of variance to each curve and see if they are significantly different from one another. The measure of variance can be achieved by averaging the curve over multiple data sets for each signal processing method adopted. There are many methods for averaging ROC curves. The most basic methods include vertical and threshold averaging.

In vertical averaging, vertical samples of the ROC curves are taken at fixed intervals of FPR and the corresponding TPR are averaged. However, this method gives only a one dimensional measure of variance. Moreover, the FPR is not an independent variable that is under direct control of the experiment controller. A preferred method is to average ROC points with independent variables whose values can be controlled directly. The threshold method overcomes this limitation.

The Area Under Curve (AUC) method is sometimes used to compare classifier performance. This method reduces the two dimensional ROC space into a single scalar value giving a measure of expected performance. The AUC, as its name depicts, is found by calculating the area under the ROC curve. The AUC is used when one wishes to evaluate performance over the entire range of detection probability, and this is useful since two ROC curves may have different curvatures but yet have the same AUC. In this research project however, the interest is in the detection performance at specific FPR rather than overall performance. Hence, the threshold averaging method is more suitable.

For each simulation in this research, 50 sets of 100 bubble cloud backscatter responses were generated to obtain 50 waterfall plots and 50 ROC curves for each of the processing method discussed. Each point on the ROC curve is plotted by varying the detection threshold and finding the percentage of correct detections and false alarms. Correct detection (TP) is measured from the waterfall plot (target present) by finding the number of pings in the time samples occupied by the target that have an amplitude higher than the specified detection threshold. A false alarm (FP) is measured from the waterfall plot (target absent) by finding the number of pings in the entire time duration that have an amplitude higher than the detection threshold. The FPR and TPR is then calculated using Eq. B.2 and B.1 respectively.

Each of the ROC curves presented in this research thesis was found by averaging over 50 ROC curves. The 95 % confidence interval for a FPR of 0.1 and

its corresponding 95 % confidence interval for TPR were plotted. Any overlap in the confidence interval of the ROC curve for the different signal processing techniques would indicate that one technique is not significantly better than any of the others.

Bibliography

[1] T. G. Leighton, "From sea to surgeries, from babbling brooks to baby scans: The acoustics of gas bubbles in liquids," *Invited Review Article for International Journal of Modern Physics B*, vol. 18, no. 25, pp. 3267–3314, 2004.

[2] T. G. Leighton, S. D. Richards, and P. R. White, "Marine mammal signals in bubble water," in *Proceedings of the Institute of Acoustics Symposium on Bio-sonar*, 2004.

[3] T. G. Leighton, P. R. White, and D. C. Finfer, "Bubble acoustics in shallow water: Possible applications in nature," in *International Conference on Boundary Influences in High Frequency, Shallow Water Acoustics*, 2005, pp. 433–440.

[4] T. G. Leighton, D. C. Finfer, and P. R. White, "Bubble acoustics: What can we learn from cetaceans about contrast enhancement?" in *Proceedings of the IEEE International Ultrasonics Symposium*, 2005, pp. 964–973.

[5] T. G. Leighton, P. R. White, D. C. Finfer, and S. D. Richards, "Possible applications of bubble acoustics in nature (opening invited paper)," in *Proceedings of the 28th Scandinavian Symposium on Physical Acoustics*, 2005.

[6] T.G.Leighton, P.R.White, D.C.Finfer, and S.D.Richards, "Cetacean acoustics in bubbly water (invited paper)," in *Proceedings of the International Conference on Underwater Acoustic Measurements, Technologies and Results*, 2005, pp. 891–898.

[7] D. C. Finfer, T. G. Leighton, and P. R. White, "Marine mammals, noise, and sonar in shallow costal bubbly waters," in *Proceedings of the Institute of Acoustics*, 2006, pp. 69–74.

[8] T. G. Leighton, D. C. Finfer, and P. R. White, "Sonar which penetrates bubble clouds (invited paper)," in *Proceedings of the Second International*

Conference on Underwater Acoustic Measurements, Technologies and Results, 2007, pp. 555–562.

[9] T.G.Leighton, D.C.Finfer, and P.R.White, "Cavitation and cetacean," in *Proceedings of the 19th International Congress on Acoustics*, 2007, pp. 1–31.

[10] T. G. Leighton, P. R. White, and D. C. Finfer, "Hypotheses regarding exploitation of bubble acoustics by cetaceans," in *Proceedings of the 9th European Conference on Underwater Acoustics, (EUCA2008)*, 2008, pp. 77–82.

[11] T. G. Leighton, D. C. Finfer, and P. R. White, "Experimental evidance for enhanced target detection by sonar in bubbly water," *Hydroacoustics*, vol. 11, pp. 181–202, 2008.

[12] T.G.Leighton, D.C.Finfer, and P.R.White, "Two hypotheses about cetacean acoustics in bubbly water," in *Proceedings of the 5th IOA International Conference on Bio-Acoustics*, 2009, pp. 119–122.

[13] T. G. Leighton, P. R. White, and D. C. Finfer, "Hypotheses on the acoustics of whales, dolphins and porpoise in bubbly water (opening plenary address)," in *Proceedings of the Third International Conference on Underwater Acoustic Measurements, Technologies and Results*, 2009, pp. 3–14.

[14] T.G.Leighton, P.R.White, and D.C.Finfer, "Contrast enhancement between linear and nonlinear scatterers," Patent International patent application number PCT/GB2006/002 335, May, 2006.

[15] E. C. Monahan, *Natural Physical Sources of Underwater Sound*. Boston, MA: Kluwer, 1993, p. 503.

[16] J. Roberts, *A Sense of the World: How a Blind Man Became History's Greatest Traveler*. New York, NY: HarperCollins Publishing, 2006.

[17] W. W. Au, *The Sonar of Dolpins*. Springer-Verlag New York, Inc, 1993.

[18] C. Kamminga and H. Wiersma, "Investigations on cetacean sonar ii. acoustical similarities and differences in odontocete sonar signal," *Aquatic Mammals*, vol. 8, pp. 41–62, 1981.

[19] S. M. Dawson and C. W. Thorpe, "A quantitative analysis of the sounds of hector's dolphin," *Ethology*, vol. 86, pp. 131–145, 1990.

[20] W. W. Au, A. N. Popper, and R. R. Fay, *Hearing by Whales and Dolphins*. Springer, 2000.

[21] L. M. Herman and W. N. Tavolga, *Cetacean Behavior: Mechanisms and Function*. Wiley, 1980, ch. The communication systems of cetaceans, pp. 149–209.

[22] H. Shirihai and B. Jarrett, *Whales, Dolphins and Other Marine Mammals of the World*. Princeton, Princeton University Press, 2006.

[23] W. W. Au, R. W. Floyd, R. H. Penner, and A. E. Murchison, "Measurement of echolocation signals of the atlantic bottlenose dolphin *Tursiop truncatus* montagu, in open waters," *J Acoust Soc Am*, vol. 56, pp. 280–290, 1974.

[24] W. W. Au, *Animal Sonar Systems*. Plenum Press, 1980, ch. Echolocation signals of the Atlantic bottlenose dolphin (*Tursiops truncatus*), in Open Waters, pp. 251–282.

[25] S. Li, K. Wang, D. Wang, and T. Akamatsu, "Echolocation signals of the free-ranging yangtze finless porpoise (*Neophocaena phocaenoides asiaeorientialis*)," *J Acoust Soc Am*, vol. 117, pp. 3288–3296, 2005a.

[26] S. Li, K. W. D. Wang, and T. Akamatsu, "Sonar gain control in echolocating finless porpoises (*Neophocaena phocaenoides*) in an open water," *J Acoust Soc Am*, vol. 120, no. 4, pp. 1803–1806, 2006.

[27] M. Minnaert, "On musical air bubbles and the sound of running water," *Phil Mag*, vol. 16, pp. 235–248, 1993.

[28] A. D. Phelps and T. G. Leighton, "Oceanic bubble population measurements using a buoy-deployed combination frequency technique," *IEEE J. Oceanic Eng*, vol. 23, pp. 400–410, 1998.

[29] D. M. Farmer and S. Vagle, "Waveguide propagation of ambient sound in the ocean-surface bubble layer," *J Acoust Soc Am*, vol. 86, pp. 1897–1908, 1989.

[30] T. G. Leighton, A. D. Phelps, and D. G. Ramble, "Acoustic bubble sizing: from laboratory to the surf zone trials," *Acoustic Bulletin*, vol. 21, pp. 5–12, 1996.

[31] A. D. Phelps, D. G. Ramble, and T. G. Leighton, "The use of a combination frequency technique to measure the surf zone bubble population," *J Acoust Soc Am*, vol. 101, pp. 1981–1989, 1997.

[32] S. D. Meers, T. G. Leighton, J. W. L. Clarke, G. J. Heald, H. A. Dumbrell, and P. R. White, "The importance of bubble ring-up and pulse length in estimating the bubble distribution from acoustic propagation measurements," in *Proceedings of the Institute of Acoustics: Acoustical Oceanography*, T. G. Leighton, H. D. Griffiths, and G. Griffiths, Eds., vol. 23, no. 2, 2001, pp. 235–241.

[33] M. S. Plesset and A. Prosperetti, "Bubble dynamics and cavitation," *Ann. Rev. Fluid. Mech.*, vol. 9, pp. 145–185, 1977.

[34] L. Rayleigh, "On the pressure developed in a liquid during the collapse of a spherical cavity," *Phil Mag*, vol. 34, pp. 94–98, 1917.

[35] M. S. Plesset, "The dynamics of cavitation bubbles," *J Appl Mech*, vol. 16, pp. 277–282, 1949.

[36] H. Poritsky, "Cavitation produced by ultrasonics," in *Proceedings of the first U.S. National Congress on Applied Mechanics*, E. Sternberg, Ed., 1952, pp. 813–821.

[37] F. R. Gilmore, "The growth or collapse of a spherical bubble in a viscous compressible liquid," California Institute of Technology, Pasadena, California, USA, Tech. Rep. 26-4, 1952.

[38] J. B. Keller and M. Miksis, "Bubble oscillations of large amplitude," *J Acoust Soc Am*, vol. 68, p. 628, 1980.

[39] A. Prosperetti, "Bubble phenomena in sound fields: Part one," *Ultrasonics*, vol. 22, pp. 69–77, 1984.

[40] C. Herring, "Theory of the pulsations of the gas bubble produced by an underwater explosion," OSRD, Tech. Rep. 236, 1941.

[41] J. C. Novarini, R. S. Keiffer, and G. V. Norton, "A model for variations in the range and depth dependence of the sound speed and attenuation induced by bubble clouds under wind-driven sea surfaces," *IEEE J. Oceanic Eng*, vol. 23, no. 4, pp. 423–438, 1998.

[42] A. Villadsgaard, M. Wahlberg, and J. Tougaard, "Echolocation signals of wild harbour porpoises, *Phocoena phocoena*," *The Journal of Experimental Biology*, vol. 210, pp. 56–64, 2007.

[43] L. Hoff, *Acoustic Characterization of Contrast Agents for Medical Ultrasound Imaging*. Kluwer Academic Publishers, 2001.